ISOTHERMAL HYDROGENATION KINETICS OF MAGNESIUM BASED HYDRIDE

by

Jingzhu Li

A thesis submitted to the faculty of
The University of Utah
in partial fulfillment of the requirements for the degree of

Master of Science

Department of Metallurgical Engineering

The University of Utah

December 2014

The University of Utah Graduate School

STATEMENT OF THESIS APPROVAL

The thesis of **Jingzhu Li**

has been approved by the following supervisory committee members:

Zhigang Zak Fang	, Chair	**6/11/2014** Date Approved
Peng Fan	, Member	**6/11/2014** Date Approved
Kent S Udell	, Member	**6/11/2014** Date Approved
Robert C Bowman	, Member	**6/22/2014** Date Approved

and by **Manoranjan Misra** , Chair/Dean of

the Department/College/School of **Metallurgical Engineering**

and by David B. Kieda, Dean of The Graduate School.

ABSTRACT

Magnesium hydride was proposed to be used for on-board heating and cooling systems due to its high energy density. Low-temperature hydrogenation has been achieved via ball milling and adding appropriate additives. However, further details regarding the mechanism for hydrogenation of magnesium hydride is not available yet.

This work first developed a methodically designed technique to test hydrogenation kinetics under isothermal condition across a wide temperature range, from room temperature to 200 ºC using a Sieverts type apparatus, in order to minimize the thermal gradient effect, which is often neglected in the literature. The tested material was ball-milled magnesium mixed with titanium hydride, a combination that had been demonstrated to have excellent hydrogenation and dehydrogenation kinetics in recent studies, and is considered to be a promising material for hydrogen storage and thermal energy storage applications. It was found that the hydrogenation kinetics under isothermal conditions were significantly different from those under nonisothermal conditions. Additionally, it was determined that the hydrogenation kinetics under isothermal conditions were numerically best fit by the Johnson-Mehl-Arrami (JMA) model.

The second part of this work further investigated the possible effect of various processing variables, including milling parameters, catalyst, as well as the effect of hydrogenation conditions, such as temperature and pressure, on the hydrogenation kinetics of magnesium hydrides. Moreover, the effect of different processing variables on grain size

and specific surface area was investigated as well. Various kinetic models have been employed to examine the hydrogenation kinetics of samples prepared by different parameters and tested under different conditions. The JMA model was found again to be the best numerical model to describe the hydrogenation behavior of the ball-milled magnesium hydride prepared in this work. In addition, the JMD (Jander Diffusion Model) model has high consistency with low-temperature hydrogenation of pure magnesium hydrides. It was found that longer milling time and smaller milling load will lead to smaller grain size of the as-milled powder, thus better hydrogenation rate and smaller activation energy. Adding catalyst could not only assist in reducing grain size of the as-milled MgH_2 powder, but also facilitate the hydrogen diffusion in Mg/MgH_2, thus reducing the activation energy of hydrogenation in both ways.

TABLE OF CONTENTS

LIST OF FIGURES

LIST OF TABLES

ACKNOWLEDGMENTS

I would like to express my profound gratitude to my advisor, Professor Zhigang Zak Fang, whose professionalism, critical thoughts, work ethic, and positive life attitude had inspired me over the graduate years and will continue to guide me in my future career. I am also genuinely grateful to his patience, encouragement, and understanding, which will be remembered and will continuously remind me to be a good person.

I would also like to thank my associate advisor, Professor Peng Fan, for the meticulous scholarship he showcased during his continuous guidance in my research work. Without him, I could have never been able to finish this thesis. Genuine gratitude is dedicated to my committee member, Dr. Robert Bowman, for his insightful suggestions, comments, and reviewing during this thesis work. Special gratitude is extended to my committee member, Professor Kent Udell, for the time and effort he spent in reviewing my work.

I would also like to express my sincere thanks to John Vajo for his valuable advice during this work. Special acknowledgement is extended to Dr. Mark Koopman for proofreading the manuscript and constructive suggestions.

A great deal of thanks is due to Chengshang Zhou and Chai Ren for their generous instructions and help in lab work, as well as valuable discussion during my research work. Special thanks are extended to Xiangyi Luo and Jun Lu for their support in X-ray characterization. I would also like to thank other group members for their generous help during my graduate years: Pei Sun, Jun Guo, Xu Wang, Quan Shi, Lu Yang, Lin Gu, Kyu

Sup Hwang, James Paramore, Benjamin Thompson, Hyrum Lefler, and Matthew Dunstan.

I would also like to acknowledge the financial support from the National Science Foundation (Grant No. 0933778) and the U.S. Department of Energy (DOE) under contract number DE-AR0000173.

I can never express enough heartfelt thanks to my parents, Jianhua Li and Ling Li. I am the luckiest child to have such great parents like them, who never stop caring, always show understanding and respect, try to teach with fun, and only become Tiger Mom & Dad when they have to.

Finally, to my beloved boyfriend, Zhixue Yuan: my deepest gratitude for the never-failing love, care, and faith he gave. It was nice to meet you, in the planet among the vastness of space, for a while in the immensity of time.

CHAPTER 1

INTRODUCTION

1.1 Electrical Vehicles

As the automotive manufacturing industry continues growing, worldwide concerns arise due to energy and environment issues. As a result, electrical vehicles (EVs) gathered considerable renewed attention after their first appearance in the mid-19th century [1], as one promising solution for fuel depletion and greenhouse gas (GHG) emission [2].

Compared to the conventional Internal Combustion Engine (ICE), there are mainly 3 types of EV, which are Battery Electrical Vehicle (BEV), Hybrid Electrical Vehicle (HEV), and Fuel Cell Electrical Vehicle (FCEV) [3]. Despite the advantages of EVs mentioned above, most of the now existing EVs suffer from problems such as low battery capacity, short driving range, and high cost. Detailed comparisons between traditional ICE vehicles, BEV, HEV, and FCEV are listed in Table 1.

1.2 Solutions to Improve EV's Performance

Besides working in the direction of increasing the energy capacity of EVs, using other energy sources to replace electricity for certain automobile components could possibly create a longer driving range as well. For example, the on-board air conditioning system accounts for a considerable amount of the available energy [4]. According to Lambert, the

Table 1. Characteristics of BEVs, HEVs, FCEVs [8, 9]

Characteristic	Energy storage	Advantages	Drawbacks	Important issues
ICE vehicles	• Fuel tank	• Matured technology • Fully commercialized • Better performance • Simple operation • Reliable • Durable	• Less efficient • Poor fuel economy • Harmful emission • Comparatively bulky	• Fuel economy • Harmful emission • Highly dependency on petroleum products
EVs	• Battery • Ultra capacitor • Flywheel	• Energy efficient • Zero emission • Independency from petroleum products • Quite • Smooth operation • Commercialized	• Limited driving range • Higher recharging time • Poor dynamic response	• Size and weight of battery pack • Vehicle performance • Infrastructure for charging stations

Table 1. Continued.

Characteristic	Energy storage	Advantages	Drawbacks	Important issues
Hybrid EVs	• Fuel tank • Battery • Ultracapacitor • Flywheel	• Higher fuel economy • Very low emission • Long electric driving range • Reliable • Commercialized • Durability	• Costly • Bulky • Complex system • Complexity in control algorithm • Increased component count	• Power management of multi-input source • Size and weight of battery pack and ICE • Integration of components
Plug in HEVs	• Fuel tank • Battery • Ultracapacitor • Flywheel	• Lower emission • Higher fuel efficient • Extended electric driving range • V2G or G2V capability • Partially commercialized • Quiet and smooth operation	• Higher complexity • Impact on grid • Higher initial cost • Sophisticated electronic circuitry • Battery technology	• Size and weight of battery pack and ICE • Charging infrastructure • Power flow control and management • Impact on grid

Table 1. Continued.

Characteristic	Energy storage	Advantages	Drawbacks	Important issues
FCEVs	• Fuel cell stack • Battery • Ultra capacitor	• Ultra low emission • Highly efficient • Independent from petroleum products • Competent driving range • Reliable • Durable • Under development	• High cost • Slow transient response • Not commercialize yet • Sophisticated electronic controllers	• Cost of fuel cell • Cycle life and liability • Infrastructure for hydrogen conditioning, storage, and refilling system

energy consumed by the mechanical compressor of a subcompact to mid-size car contributes 12-17 % of all on-board energy [5]. Otherwise, exhaust waste heat has been reported as a possible power source for on-board air conditioning systems [5, 6]. However, an air conditioning system that uses waste heat as the exclusive power source is subject to scenarios when waste heat is not sufficient, such as start-up or idling; otherwise, extra components such as a small pump or refrigerant reservoir need to be added, which will definitely impair the energy density of the overall air conditioning system.

1.3 Metal Hydride-Based Thermal Battery for On-board Air Conditioning

Recently, a high energy density thermal battery based on metal hydride has been proposed by Fang et al. at the University of Utah for the use of heating, ventilation, and air conditioning (HVAC) of an electric vehicle [7], which is self-contained and does not rely on the electricity provided from battery. The principle of this thermal battery is schematically illustrated in Figure 1.

This proposed thermal battery uses a pair of metal hydrides, one as the low temperature (LT) hydride with a higher equilibrium pressure, the other as the high temperature (HT) hydride with a lower equilibrium pressure, and can dehydrogenate at a moderate higher temperature. The two beds are connected as a closed system with controlling valves. Hydrogen will flow in between to realize charging and discharging.

This proposed thermal battery can provide both heating and cooling during charging. Before charging, the LT hydride is in hydride form and the HT hydride is in metal form. Once the valve is open, hydrogen will be released from the LT bed due to a higher

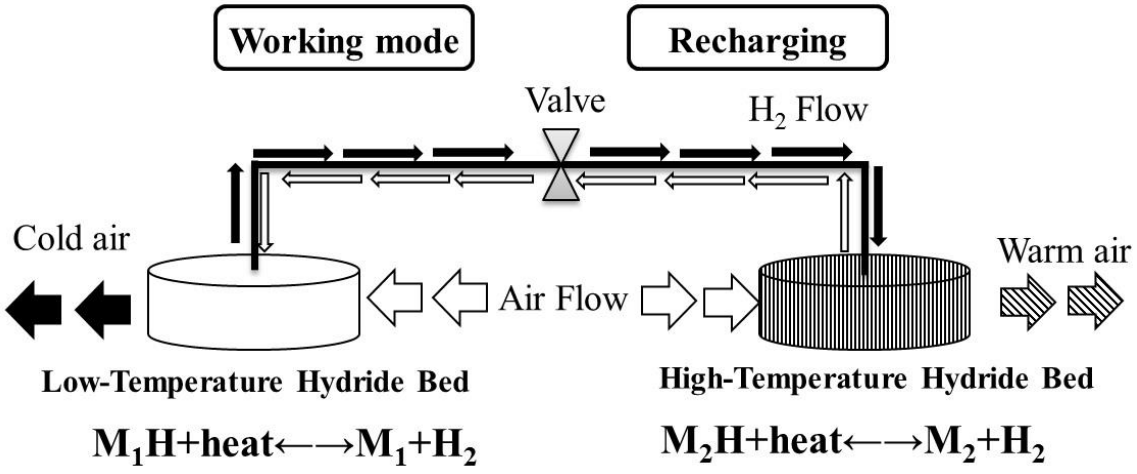

Figure 1. Principle of the high energy density metal hydride thermal battery.

equilibrium pressure. As the dehydrogenation continues, the LT bed will be cooled due to the endothermic reaction. On the other side, hydrogen will be absorbed by the HT hydride, the equilibrium pressure of which is lower than that of LT hydride. As a result, the HT bed will be heated up by the released heat. Therefore, the cabin can be either heated or cooled by blowing ambient air through the HT bed or LT bed, respectively.

After a charging process, a recharging process is necessary for subsequent time use. This is done by heating up the HT hydride to a certain temperature to allow HT hydride to dehydrogenate, while the LT bed will stay at room temperature and absorb the hydrogen released from the HT bed.

1.4 Metal Hydride

Metal hydrides are defined as concentrated single-phase compounds involving the host metal and hydrogen [10, 11]. According to the crystal structure, metal hydrides can be classified into five categories; see Table 2 [12-14]. Most metal hydrides have high energy density compared to other thermal storage materials [11]. The energy density of two paired metal hydrides proposed for the thermal battery application mentioned in section 0 is shown in Figure 2, along with the energy density of single metal hydrides and other heat storage materials. See Appendix A for more calculation details of the energy density listed in Figure 2.

Metal hydrides have been proposed for thermal application [12, 15-17], hydrogen storage [11, 12, 17-20], batteries [18, 21-23], and other applications such as getters, separation, purification, compressor, sensor, and detector optical switch [12, 18, 20, 24].

Table 2. Metal hydrides categories and representative metal hydrides.

Alloy type	Crystal structure	Examples	Maximum H Capacity (wt.%)	Enthalpy (kJ/mol H_2)	P_{eq} at 298 k (bar)
A	A3 (hP_2)	MgH_2	7.66	74.5	$\sim10^{-6}$
	A2 (CI_2)	VH_2	3.81	40.1	2.1
A_2B	Ca (hP_{18})	Mg_2NiH_4	3.59	64.5	$\sim10^{-5}$
AB	B2 (cP_2)	$TiFeH_2$	1.89	28.1	4.1
	Bf (oC_8)	$ZrNiH_3$	1.96	68.6	$\sim5x10^{-6}$
AB_2	C14 (hP_{12})	$TiMn_{1.4}V_{0.62}H_{3.4}$	2.15	28.6	3.6
	C14 (hp_{12})	$ZrMn_2H_{3.6}$	1.77	53.2	0.001
AB_5	D2d (hP_6)	$LaNi_5H_{6.5}$	1.49	30.8	1.8
	D2d (hP_6)	$LaNi_{4.8}Sn_{0.2}H_{6.0}$	1.40	32.8	0.5

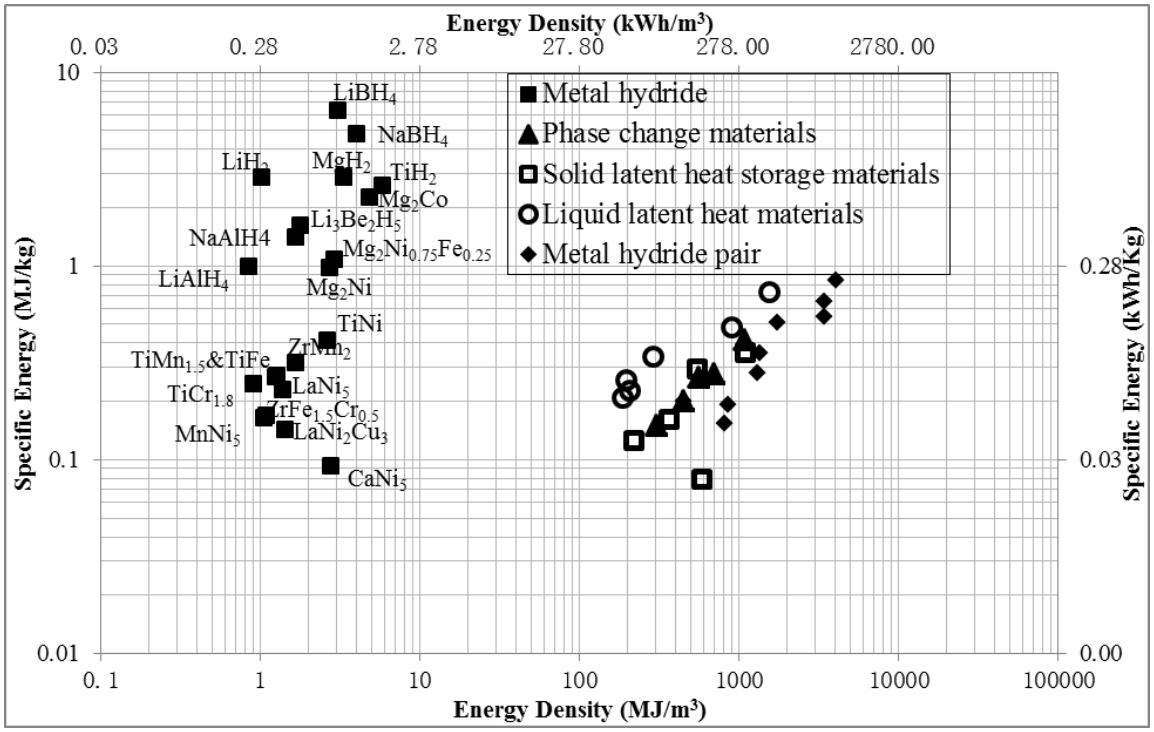

Figure 2. Energy density of various thermal storage materials.

1.5 Magnesium Hydride

In order to be used for on-board air conditioning, metal hydride must meet several criteria: 1) fast kinetics near ambient temperature; 2) good cycle ability; 3) high energy density; 4) low cost; and 5) environmental friendly [3]. Among various metal hydrides, magnesium hydride is considered as a promising candidate of HT hydride for the proposed thermal battery application, due to its high theoretical capacity (7.6 wt.%), high formation enthalpy (74.5 kJ/mol H_2), and thus relative high energy density [15]. Other merits of magnesium hydride such as practically reversible and abundant resources also add to its potential of practical application. In the past, the sluggish kinetics of magnesium hydride, especially the hydrogenation kinetics at low temperature, was a major obstacle impeding further application of magnesium hydrides. However in recent studies, the fast kinetics, even at room temperature, has been made available now by ball milling and adding proper additives [25-27].

1.6 Research Scope

As kinetics is such an essential issue for on-board air conditioning, detailed studies regarding hydrogenation and dehydrogenation of metal hydride is necessary for the development of the proposed thermal battery. However, even though there were large quantities of literature reporting the kinetics studies of metal hydride or metal hydride with different catalysts, the hydrogenation kinetics is not yet fully understood and little agreement has been achieved. In the meantime, there are issues still left unsolved: 1) significant thermal effect for hydrogenation due to the exothermic reaction [28]; 2) most of the hydrogenation kinetics studies focus on the high-temperature hydrogenation, while

low-temperature hydrogenation is more of a importance in practice but is less studied.

Current work mainly focuses on the kinetics study of magnesium hydride used on the air conditioning system of next generation electrical vehicles. The major objectives are: 1) find an appropriate methodology to minimize thermal effect; 2) investigate the effect of multiple processing variables, such as milling load, milling time, and catalyst, as well as the effect of hydrogenation condition, such as temperature and pressure; 3) learn more about the hydrogenation mechanism of magnesium hydride.

CHAPTER 2

LITERATURE REVIEW

2.1 Magnesium and Magnesium Hydrides

2.1.1 Material Characteristics

Magnesium is an abundant element on earth, accounting for 2.7 wt.% of the earth's crust [29]. The only stable hydride phase existing in equilibrium with Mg at moderate hydrogen pressures is magnesium dihydride, MgH_2, which is usually referred to as "magnesium hydride" [14]. As H is initially introduced into the hexagonally close-packed (HCP) Mg metal lattice, the H atoms will first occupy tetrahedral interstitial sites, forming a solid solution of H in magnesium alloy, α MgH_2. As H concentration accumulates, the most stable MgH_2 phase, β MgH_2, will form, where Mg atoms are octahedrally coordinated to six H atoms and each H atom is coordinated to three Mg atoms in a planar coordination, as shown in Figure 3. According to Bastide et al. [30], when subjected to up to 80 kbar hydrogenation pressure, β MgH_2 phase will partially transform into another metastable polymorphic phase, γ MgH_2, which decomposes above 300 °C [14]. The packing and coordination of Mg and H are maintained during the phase transformation from β MgH_2 to γ MgH_2. However, the octahedral chains are deformed into a zigzag form [29]. See Table 3 for the crystallographic parameters of the phases in Mg-H system. The bonding of hydrogen in MgH_2 was a combination of ionic and covalent bonding, which is weak but

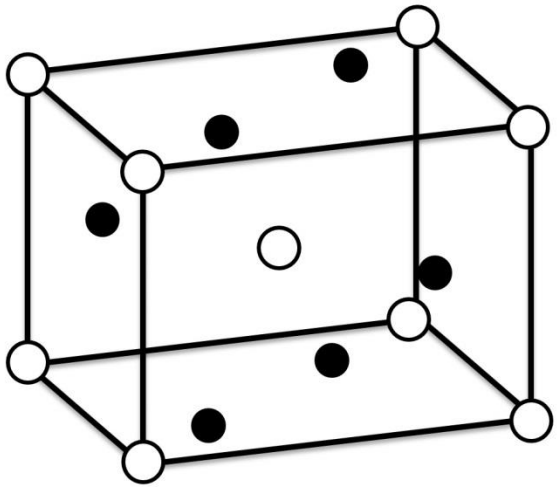

Figure 3. Crystal structure of β MgH_2 (Mg atom: open ball, H atom: solid ball).

Table 3. Crystallographic parameters of the phases in Mg-H system [29].

Form	Structure	Space group	a (nm) *	b (nm)	c (nm)	Density (g/cm^{-3})
Mg	hexagonal	P_{63}/mmc	0.321	0.321	0.521	1.74
α MgH_2	Solid solution (Tetrahedral interstitial site)	P	0.540	0.540	1.099	1.79
β MgH_2	Body centered tetragonal	P_{42}/mnm	0.452	0.452	0.302	1.42
γ MgH_2	Orthorhombic	Pbcn	0.453	0.544	0.493	-

* Temperature is 293 K

significant between Mg and H as well as H and H [14, 31, 32].

2.1.2 Thermodynamics

The enthalpy and entropy of magnesium hydride formation were determined experimentally since the 1960s, which were ΔH= 74.5 kJ/mol H_2 and ΔS = -135 J/K.mol H_2, respectively [33]. The most common approach to calculate enthalpy and entropy value of magnesium hydride formation is to obtain equilibrium pressure at different temperatures via experimental equilibrium isotherms. At least three sets of equilibrium pressure at different temperature are necessary to generate a linear plot, $ln(P_{eq})$ against $1/T$, then ΔH and ΔS can be calculated via the slope and intercept, according to Van's Hoff equation, Eq. 1, where P_{eq} is the equilibrium pressure, R is gas constant, and T is reaction temperature. The values of ΔH and ΔS obtained by this experimental method are reported as 68~75.2 J/K.mol H_2 and -135.1~-126 J/K.mol H_2, respectively [25, 34-37].

$$ln\, P_{eq} = -\frac{\Delta H}{RT} + \frac{\Delta S}{R} \qquad \text{Eq. 1}$$

The desired enthalpy value of magnesium hydride is between 10 and 60 kJ/mol H_2 because physisorption is too weak below 10 kJ/mol H_2 while chemisorption is too high above 60 kJ/mol H_2 [14]. With a formation enthalpy approximate 75 kJ/mol H_2, the operating temperature for pure magnesium hydride application is relatively high as a result, creating a drawback to magnesium hydride application. Over these years, in order to reduce the thermal stability of magnesium hydride, various metals has been alloyed with magnesium, including rare earth (e.g., Ce, La), non-transition (e.g., Al, Li, In), and transition metals (e.g., Ni, Co, Fe, Cu, Ag, Sc, Y) [38-44]. Zhou et al. reported that magnesium hydride doped with indium has a 70 % lower equilibrium pressure, with an

experimental tested enthalpy of 70.9 kJ/mol H_2 compared to 76.6 kJ/mol H_2 of pure magnesium hydride [40].

2.1.3 Hydrogenation and Dehydrogenation

Another major problem impeding the practical application of magnesium hydride is the sluggish kinetics of both hydrogenation and dehydrogenation [29, 38, 45]. Hydrogenation of magnesium is exothermic while dehydrogenation is endothermic, as shown in Eq. 2, where the rightward is hydrogenation and the leftward is dehydrogenation.

$$Mg+H_2 \longleftrightarrow MgH_2 \quad \Delta H = 74.5 \text{ kJ/mol } H_2 \qquad \text{Eq. 2}$$

As mentioned in section 2.1.2, the enthalpy of formation for magnesium hydride is 74.5 kJ/mol H_2, implying a relatively high operation temperature is necessary for both hydrogenation and dehydrogenation. During recent decades, there has been a large quantity of studies focusing on improving the hydrogenation/dehydrogenation kinetics of magnesium hydrides. Two major ways are: 1) reducing particle size and 2) using additives.

Typically, the most common way to reduce particle size of magnesium hydride is ball milling [46-48]; other methods such as chemical/physical vapor deposition [49-52], rolling [53, 54], and combustion [55, 56] have also been employed to prepare magnesium-based hydrides. The experimental onset temperature of dehydrogenation for as-received magnesium hydride tested by Differential Scanning Calorimetry (DSC) is 420-450 ºC [46-48]. Polanski et al. showed that ball-milled magnesium hydride could dehydrogenate at 325 ºC under a 1 bar back pressure, while as-received magnesium hydride cannot [48]. Also, ball-milled magnesium hydride could uptake approximately 3 wt.% more hydrogen at 300 ºC under 10 bar pressure [48].

Another way to improve hydrogenation and dehydrogenation kinetics of magnesium hydride is using additives. The most widely studied additives are: 1) transition metals and transition metal compounds; b) intermetallic compounds and alloys, and 3) carbon and composites [46, 57-59]. See Table 4 for more details of the catalysts. With appropriate additives, the dehydrogenation temperature of magnesium hydride could be as low as ca. 200 ºC [25]. It should be pointed out that the decrease of dehydrogenation temperature to such a level (~200 ºC) is merely kinetics improvement, and there is no alteration in formation enthalpy of magnesium hydride. Further reduction in dehydrogenation temperature of magnesium hydride requires thermodynamic modification [40]. A big breakthrough, room temperature hydrogenation of magnesium hydride, was also available with the participation of appropriate additives, such as Nb [27], Nb-V [60], V-Cr [61, 62], and Ti-based binary and ternary intermetallic compounds [25].

2.2 Hydrogenation Kinetics Study of Magnesium Hydride

In order to be practically used on automobiles, one of the preconditions is the fast kinetics at low temperature range, even as low as room temperature. Take the proposed thermal battery as an example; less, if not no, extra energy is required to start working mode. In other words, the metal hydrides do not need to be heated up, or only need a moderate temperature, to hydrogenate and dehydrogenate. Further understanding in the hydrogenation kinetics of magnesium hydride and related mechanisms helps to improve the hydrogenation properties more specifically. Even though the hydrogenation kinetics has been improved considerably by adding additives and ball milling, an agreement in the mechanism of magnesium hydrogenation has not yet been established.

Table 4. Catalysts used for magnesium hydrides.

Category	Examples		References
Transition metals and Transition metal compounds	Ti-based	Ti, TiH_2, TiO_2, $TiCl_3$, TiC, TiF, and TiB_2	[34, 63-65]
	V-based	V, V_2O_5	[66, 67]
	Nb-based	Nb-based, Nb, Nb_2O_5, NbF_5, and NbH	[27, 68-70]
	Others	Ni-, Fe-, Co-, Pd-, Zr-, Mn-, and Cr-based	[47, 54, 71-75]
Intermetallic compounds	$TiMn_2$, TiFe, Mg_2Ni, Nb-V alloy, V-Ti-Cr alloy, and misch metals		[25, 61, 72, 76-78]
Other additives	Carbon nanotubes		[79, 80]
	$NaAlH_4$, LiH, and $LiAlH_4$		[81-83]

2.2.1 Kinetics Studies

Chemical kinetics focuses on the quantitative study of the rates of chemical reactions and of the factors upon which they depend [84]. Conventionally, the reaction progress is defined as the fraction of the transformation, ξ ($0 \leq \xi \leq 1$), which is a function of reaction time, t, and rate constant, k, as shown in Eq. 3:

$$\xi = f(k,t) \qquad \text{Eq. 3}$$

The rate constant k is also known as specific rate and the rate coefficient is numerically equal to the reaction rate when the reactants are present at unit concentrations [84]. Rate constant k is a function of temperature [85]. The relationship between rate constant k and temperature T was first found empirically by Hood that the rate constant k of a reaction varies with the absolute temperature T according to a law of the following form [86, 87], Eq. 4.

$$\log k = B - \frac{A'}{T} \qquad \text{Eq. 4}$$

where A' and B are constants. Later in 1884, Van't Hoff argued on the basis of the effect of temperature on equilibrium constants [88]. This idea was extended by Arrhenius [89] who suggested in the late 1800s that the rate constant k of most reactions varies with temperature T following a rule as shown in Eq. 5.

$$\mathrm{k} = A\exp(-\frac{E_a}{RT}) \qquad \text{Eq. 5}$$

where k is the rate constant, A is the frequency factor or pre-exponential factor, and T is the absolute temperature. If we take the natural logarithm of both sides of Eq. 5, the Arrhenius equation becomes Eq. 6.

$$\ln k = -\frac{E_a}{RT} + \ln A \qquad \text{Eq. 6}$$

Even though the Arrhenius law is empirical, it was found to be highly accurate for almost all the types of chemical reactions [84]. Arrhenius first mentioned the concept of activation energy, E_a, as the minimum energy that must be input to a chemical system, containing potential reactants, in order for a chemical reaction to occur. Activation energy could be calculated by the slope of the Arrhenius plot, which is *ln(k)* against the reciprocal of the absolute temperature *1/T* [84].

2.2.2 Methods of Kinetics Studies for Gas-solid Reactions

There are diverse methods to study chemical kinetics such as calculating rate constants, half-life method, differential method, isolation method, etc. [84, 85]. As hydrogenation of magnesium hydride is a gas solid reaction, the reaction rate in terms of concentration cannot be easily obtained. Instead, the fraction of transformation ξ is frequently chosen as the index to evaluate hydrogenation kinetics [85]. Usually, the fraction of transformation ξ is not measured directly but converted based on reaction variables such as mass, volume, pressure, etc.

Theoretically, during the kinetics measurement, sample temperature should be kept as a constant, i.e., kinetics measurement should be performed under isothermal condition. Approximately 20 rate laws have been found applicable to describe the kinetics of solid state processes [85]. Table 5 listed the most commonly used rate laws applied in the hydrogenation kinetics studies [85].

As experimental technologies develops during recent decades, the detection of subtle changes under temperature variation became available, which allows for nonisothermal

Table 5. Classification of most commonly used rate laws for gas-solid reactions.

Rate laws	Numerical equation	Mechanism	Curve shape
P1 power	$\xi^{1/n}=kt$	--	Concave
E1 exponential	$ln(\xi)=kt$		
Johnson-Mehl-Avrami (JMA)	$ln(-ln(1-\xi))=ln(k)+nln(t)$	Nucleation and Growth mechanisms	Sigmodial
B1 Prout-Tompkins	$ln(\xi/(1-\xi))=kt$		
Jander diffusion model (JMD)	$(1-(1-\xi)^{1/3})^2=kt$		
1-D diffusion	$\xi^2=kt$	Diffusion controlled mechanisms	
2-D diffusion (Bidmensional particle shape)	$(1-\xi)ln(1-\xi)+\xi=kt$		
3-D diffusion (Ginsling-Braunshteinn model)	$(1-2\xi/3)-(1-\xi)^{2/3}=kt$		Convex
2-D contracting area	$1-(1-\xi)^{1/2}=kt$	Based on geometrical models	
3-D contracting volume	$1-(1-\xi)^{1/3}=kt$		
F1 first order	$-ln(1-\xi)=kt$	Based on reaction order	
F2 second order	$1/((1-\xi)=kt$		
F3 third order	$(1/(1-\xi))^2=kt$		

kinetic studies. The only restriction is that heating rate must be constant [74, 85, 90]. One of the major methods is to measure the weight change via TGA or DSC based on the Kissinger theory, Eq. 7. Kissinger [90] successfully evaluated kinetics behavior of gas-solid reactions under a constant heating rate via differential thermal analysis patterns.

$$\ln(\frac{\beta}{T_{max}^2}) = -\frac{E_a}{R}(\frac{1}{T_{max}}) + F_{KAS}(\xi) \qquad \text{Eq. 7}$$

where T_{max} is the temperature when reaction rate reaches the maximum, β is the heating rate, E_a is the activation energy, R is the gas constant, ξ is the fraction of transformation, and $FKAS(\xi)$ is the function of fraction of transformation ξ. In such a nonisothermal analysis, activation energy can be calculated via the slope of the Kissinger plot, which is $\ln(\frac{\beta}{T_{max}^2})$ against $\frac{1}{T_{max}}$. Other methods such as the Reich and Stivala Method reveal more kinetics details, which were explained in other earlier works [85] and will not be covered in this work.

2.2.3 Hydrogenation Kinetics Studies

The hydrogenation for metal hydrides consists of the following five steps [91, 92]:

1) Physisorption of hydrogen molecules;

2) Dissociation of hydrogen molecules and chemisorption;

3) Surface penetration of hydrogen atoms;

4) Diffusion of hydrogen atoms through the hydride layer, either by an interstitial or a vacancy mechanism;

5) Hydride formation at the metal/hydride interface.

A commonly accepted assumption is that among the five steps, there could be one

or several steps that are much slower than the others, which is usually defined as the rate-limiting step, i.e., the rate of the entire hydrogenation process depends on this step [91, 93].

For the hydrogenation kinetics study, one requirement that must be met is that driving force of the hydrogenation should be constant [94-96]. The constant driving force does not mean a constant pressure, but rather a constant value of the pressure dependence factor *F(P)*, which has various forms used by earlier investigators; see Table 6. Rudman [94] derived a driving force factor, $T(1-(P_{eq}/P)^{1/2})$ for hydrogenation and $T(1-(P/P_{eq})^{1/2})$ for dehydrogenation, which combined the effect of both pressure and temperature based on the Johnson-Mehl-Avrami (JMA) equation, with the assumption that the rate-limiting step for hydrogenation/dehydrogenation was diffusion. Later in 1999, Ron [96] put forward a normalized pressure dependence method (NPDM). The NPDM suggested to use the pressure dependence factor $F(P)=|P_{eq}-P|/P$, and insert the pressure dependence factor in the rate equations, $f(\xi)=ktF(P)$, to offset the effect of pressure variation.

In addition, if using isothermal methods to evaluate the kinetics, sample temperature must be kept constant, or at least varied in a small temperature range only. Unfortunately, an isothermal condition is usually difficult to maintain during hydrogenation of magnesium hydrides due to the thermal gradient effect or self-heating phenomenon [28, 97]. The thermal gradient effect or self-heating phenomenon refers to the rise of temperature during the initial stage of hydrogenation [28, 97], and is primarily an effect of the large exothermic hydrogenation reaction heat and the poor heat conductivity of the hydrogen storage materials. Due to insufficient heat dissipation from the hydrogen storage material, a large amount of heat released during hydrogenation will accumulate and raise the temperature

Table 6. Pressure dependence factors *F(P)* used by previous investigators [96].

F(P)	*F(P)*	*F(P)*
$\lvert P_{eq}-P\rvert/P_0$ (P_0=1 atm)	$\lvert P^{1/2}-P_{eq}^{1/2}\rvert$	$[(P-P_{eq})/P_0]^n$
$\lvert ln(P_{eq}/P)\rvert$	$\lvert P-P_{eq}\rvert$	$F(P/P_{eq})^n$
$\lvert P-P_{eq}\rvert/P_{eq}$	$P^{1/2}$	$F(P_{eq}/P)^n$

of the material. This propels a faster reaction, resulting in even more heat releasing, leading to considerable temperature rise. This significant self-heating phenomenon has been observed during hydrogenation as a temperature spike during the initial stage of the process. Moretto et al. reported that during hydrogenation of Mg-based materials, the sample temperature could rise by as much as 80 ºC in the initial hydrogenation period [28].

The effects of self-heating on the kinetics of hydrogenation have also been reported for studies of Mg_2Ni and $LaNi_5$ alloys [98-100]. Three methods have been primarily used to minimize the self-heating effect: using a smaller mass of sample [28], changing reaction vessel design, and/or adding thermal ballast [98]. Thermal ballast serves as a heat buffer, which not only accelerates the heat conduction but also absorbs the heat itself, thus minimizing the temperature fluctuation. Thermal ballast materials should have high thermal conductivity and high heat capacity, and should be inert to H_2 as well as the reaction materials.

2.2.4 Case Studies of Hydrogenation Kinetics of Magnesium Hydrides

The earliest study of hydrogenation of magnesium hydride dated back to 1955, when Ellinger et al. [101] concluded the hydrogenation of pure magnesium obeys the second order rule. Later Kennelley et al. [37] claimed that the hydrogenation of pure magnesium is a first order reaction. In 1976, Stander [102] reported a more detailed investigation regarding the hydrogenation kinetics of pure magnesium. As Stander claimed, initially the hydrogenation process is a rapid surface reaction, governed by the relation $1-(1-\xi)^{1/2}=kt$; while after the metal surface has been covered by the formed hydride, hydrogenation becomes a diffusion controlled procedure, and governed by $(1-2\xi/3)-(1-\xi)^{2/3}=kt$. These

early works were done to study hydrogenation of pure magnesium hydrides. Huot et al. contended that diffusion was the controlling step for hydrogenation of magnesium hydrides because diffusion rate in β phase is much smaller than that in α phase, while no further evidence was provided [48].

Since ball milling techniques and additives were introduced to prepare magnesium hydride, the hydrogenation properties have been improved considerably. Both the change in particle size/grain size and the composition of materials could lead to the change in hydrogenation mechanism. Moreover, the improvement in hydrogenation kinetics of magnesium hydrides allows such material to uptake hydrogen at a much lower temperature, which must be treated differently from hydrogenation at high temperature.

Lu et al. [26] studied the hydrogenation kinetics of ball-milled magnesium hydride with the presence of TiH_2. Such material has superior kinetics and can even uptake hydrogen at room temperature. Lu found the first order rate law can best describe the hydrogenation kinetics of ball-milled magnesium with TiH_2, and the calculated activation energy was 16.4 kJ/mol H_2. He further concluded that the rate-limiting step was the hydrogen dissociation based on the fact that adding TiH_2 made a drastic improvement to the hydrogenation kinetics.

Zhou et al. [25] compared the effect of Ti-base intermetallic compounds on the hydrogenation kinetics of ball-milled magnesium hydrides. With most of the reported Ti-based intermetallic compounds, the ball-milled magnesium hydrides could absorb hydrogen at room temperature. The Johnson-Mehl-Avrami (JMA) rate law was applied to characterize the hydrogenation behavior of the ball-milled magnesium hydride with various Ti-based intermetallic compounds, such as $TiMn_2$, TiAl, TiNb, TiFe, TiVMn, etc.,

with an activation energy varied from 20.6-25.5 kJ/mol H_2.

Tan et al. [60] examined the hydrogenation kinetics of thin film magnesium hydride using Nb-V alloys as catalyst. Throughout the kinetics analysis, a driving force factor $T(1-(P_{eq}/P)^{1/2})$ was kept constant, as Rudman suggested. The authors found that the entire hydrogenation kinetics behavior could be interpreted by the Johnson-Mehl-Avrami (JMA) rate law as a two-stage procedure. During the first stage, hydrogenation rate was much faster than that during the second stage. They also combined cryo-stage TEM results of partially absorbed material and concluded that the two-stage hydrogenation behavior was due to the distribution and stability of the surface catalyst, which in turn determined the cycle ability of such material.

Barkhordarian et al. [103] studied both the hydrogenation and dehydrogenation kinetics of magnesium hydrides with a different amount of Nb_2O_5 as catalyst. They fit the experimental data with different kinetics models such as the JMA model, contracting volume, etc. Then the authors concluded that the hydrogenation of such material was controlled by diffusion, while dehydrogenation mechanism varied with different Nb_2O_5 content and different milling time.

In addition to experimental characterization, there was also theoretical calculation focusing on the hydrogenation kinetics of magnesium hydrides. Yao et al. [104] calculated the diffusion coefficient as a function of temperature and verified with experimental results of Mg-FeTi-CNT system. As to the theoretical model, assumptions are: 1) diffusion is the control step of magnesium hydrogenation; 2) particles are spherical; 3) hydrogen diffusion is much faster along grain boundaries than that through grains; 4) hydrogen concentration around each grain is the same and is pressure dependent, and 5) the diffusion rate in

magnesium is much larger than that in magnesium hydride. The authors also discussed the effect of grain size on the hydrogenation kinetics and suggested that reducing grain size leads to faster kinetics.

A comparison and summary of previous studies of hydrogenation kinetics of magnesium hydrides is listed in Table 7. There were lots of kinetics studies regarding hydrogenation of metal hydrides other than magnesium hydrides, among which $LaNi_5$-based material is one of the most thoroughly studied metal hydrides. However, no agreement has been reached so far regarding to the rate-controlling step, or kinetics mechanism for hydrogenation of $LaNi_5$-based materials.

Pan et al. [105] analyzed the hydrogenation kinetics of Mg-$LaNi_5$ composites with Chou's model, a new model developed by Chou and Xu with more explicit analytic explanation [93]. They found the controlling step in hydrogenation of the Mg-$LaNi_5$ composites was hydrogen diffusion if sample was prepared by microwave sintering (MS) and combustion synthesis (CS); however, if sample was prepared by mechanical milling (MM), the rate-controlling step became surface penetration. This change in hydrogenation mechanism implies that different sample preparation methods could lead to discrepancy in kinetic behavior.

Muthukumar et al. [92] compared the hydrogenation kinetics of $LaNi_5$ with $LaNi_{4.7}Al_{0.3}$ and $LaNi_{4.9}Sn_{0.1}$. It turned out that the Jander Diffusion Model (JMD) could successfully describe the hydrogenation behavior of all three metal hydrides, which meant diffusion was the most possible mechanism for hydrogenation of these $LaNi_5$-based materials. However, the hydrogenation of a similar metal hydride, $LaAl_{0.25}Ni_{4.75}$, appeared to be controlled by interface phase transition, according to Haberman et al. [106]. Later Oh

Table 7. Summary of previous studies on hydrogenation kinetics of magnesium hydride.

Catalyst	Rate law or mechanism	Activation energy (kJ/mol H_2)	Driving force	Ref.
None	Second order	-	-	[101]
None	First order	111.3*	-	[37]
None	First surface control, then diffusion control	95.5	$P>>P_{eq}$	[102]
10% TiH_2	First order, H_2 dissociation	16.4	$P>>P_{eq}$	[26]
Nb-V	JMA	14.6	Rudman	[60]
Ti-based intermetallic compound	JMA	20.6-25.5	Constant pressure	[25]
None	Studied hydrogenation kinetics using modeling, effect of grain size was also examined			[104]

* Not listed in article, calculated based on the given data

et al. [107] found the hydrogenation of $LaNi_{4.5}Al_{0.5}$ is controlled by the dissociative chemisorption of hydrogen molecules.

To conclude, the general approach of kinetics characterization is to fit experimental data with different models. Various factors could influence the hydrogenation kinetics of metal hydrides, for example, adding additives or not, how sample was prepared, what sample processing parameters were used such as milling time, as well as the test condition such as temperature and pressure.

CHAPTER 3

RESEARCH OBJECTIVES

As discussed before, there have been only a few studies focusing on the hydrogenation of magnesium hydride-based materials. Moreover, discrepancies regarding the rate-controlling step for hydrogenation of magnesium hydrides have not been resolved so far.

Firstly, the thermal effect during hydrogenation of magnesium hydrides was often neglected in the kinetics studies. The reported three ways to eliminate thermal effect, use a small amount, change reaction vessel design, and add ballast, have their own drawbacks when dealing with magnesium hydride. Due to the relatively large formation enthalpy and poor thermal conductivity of magnesium hydride, the thermal effect of magnesium hydride is more serious than many other metal hydrides such as $LaNi_5$ and Mg_2Ni; thus, merely reducing the amount of magnesium might be insufficient for maintaining the isothermal condition. Changing reaction vessel design could be a possible but not universal resolution due to the variety of the test methods and equipment. The proven successful thermal ballasts reported for $LaNi_5$ and Mg_2Ni, such as copper and nickel, will alloy with magnesium, especially during dehydrogenation at high temperature.

Secondly, the hydrogenation temperature in previous kinetics studies of magnesium hydrides was relatively high considering the kinetics improvement these recent years. Room temperature hydrogenation is now available with ball milling techniques and proper

additives. Moreover, low-temperature hydrogenation is of more importance in practical application because there is no need to heat up the materials in order to start hydrogenation. However, the existing kinetics studies mainly focus on a temperature range higher or much higher than 200 ºC.

Thirdly, the mechanism of magnesium hydrogenation could possibly be altered when processed with different variables. As we discussed in section 2.2.4, the change in milling method and milling parameters could possibly alter the rate-limiting step of magnesium hydrogenation. More details regarding the effects of processing and testing parameters on the hydrogenation kinetics are necessary to further understand and improve the properties of magnesium hydride.

Therefore, the research objectives in this work are:

1) Find a suitable method to minimize the thermal effect;

2) Investigate the effect of milling parameters and catalyst;

3) Investigate the effect of temperature and pressure on hydrogenation of magnesium hydride-based materials;

4) Try to understand the kinetics mechanism of hydrogenation for magnesium hydrides.

CHAPTER 4

EXPERIMENTAL WORK

4.1 Materials Preparation and Handling

The starting material, MgH_2 and TiH_2, were used as received. $TiMn_2$ and 75V-5Ti-20Cr needed to be pulverized through an activation process, during which sample would undergo a cycle of pressurizing (~150 bar) and evacuations 3-4 times under room temperature. Before usage, graphite will be degassed under vacuum for 4 h at 400 ºC, in order to eliminate the possible residual water and gas. The detailed information of materials used in this work is listed in Table 8. All the material handling included in the present study was carried out in a glovebox and sample will be sealed before being taken out. The glovebox is filled with purified argon (99.999%), which contained less than 1 ppm water vapor and 1 ppm oxygen, in order to minimize contamination.

Samples were milled using 1/4 inch stainless steel balls (ca. 330 g) via a custom-made ultrahigh-energy-high-pressure (UHEHP) planetary milling machine. Before ball milling, a sample was sealed inside the glovebox in a 160 ml nonstirred vessel from Parr Instrument, and pressurized to ~150 bar. After ball milling, sample was first depressurized and then handled inside the glovebox.

Table 8. Raw materials used in this work.

Material	Purity (%)	Company	Handling	Handling
MgH_2	98	Sigma-Aldrich	As received	Glovebox
TiH_2	99	Alfa-Aesar		
$TiMn_2$*	-	Sigma-Aldrich	Used after	Activation,
75V-5Ti-20Cr	-	Custom made**	activation	Glovebox
Graphite	99.9999	Alfa-Aesar	Used after degassing	Degas, Glovebox

* The composition for $TiMn_2$ is $Ti_{0.98}Zr_{0.02}V_{0.43}Fe_{0.09}Cr_{0.05}Mn_{1.5}$

** The 75V-5Ti-20Cr was made in HRL Laboratories

4.2 Sample Characterization

4.2.1 Kinetics Test

Hydrogenation kinetics measurements were performed using a commercial Sieverts type apparatus (PCTPro-2000), and a detailed sample cell configuration is shown in Figure 4. To obtain more accurate temperature reading, a K-type thermocouple was inserted in a stainless steel thermocouple well that was in direct contact with the sample powder. Hydrogen pressure was measured using a Teledyne Taber model 206 piezoelectric transducer, 0-200 bar, with a resolution of 10^{-3} bar. The amount of hydrogen desorbed and absorbed was calculated by the pressure change in the calibrated volume. Each time, approximately 0.5 g of the powder mixture was loosely packed in a stainless steel sample holder, which was then sealed in the PCT autoclave in the glovebox. Before being used in hydrogenation kinetics tests, each fresh sample would undergo 3 cycles of hydrogenation and dehydrogenation at 300 °C to eliminate the residual stress produced during mechanical milling, using a pressure of 10 bar for hydrogenation and 0.01 bar for dehydrogenation.

4.2.2 X-ray Diffraction (XRD)

High energy X-ray diffraction (XRD) was used for phase identification and grain size estimation. The experiments were operated at the Sector 11 of the Advanced Photon Source (APS), Argonne National Laboratory. The samples were sealed up in a Kapton tape in the glovebox. The 2-D diffraction patterns were collected in the transmission mode using either a Piratus 2M or a Perkin–Elmer large-area detector, and transformed to 1-D patterns (intensity vs. 2θ) for final data analysis by integration with the FIT2D software, after which data processing and analysis was performed using MDI Jade 5.0. Grain size (D) and strain

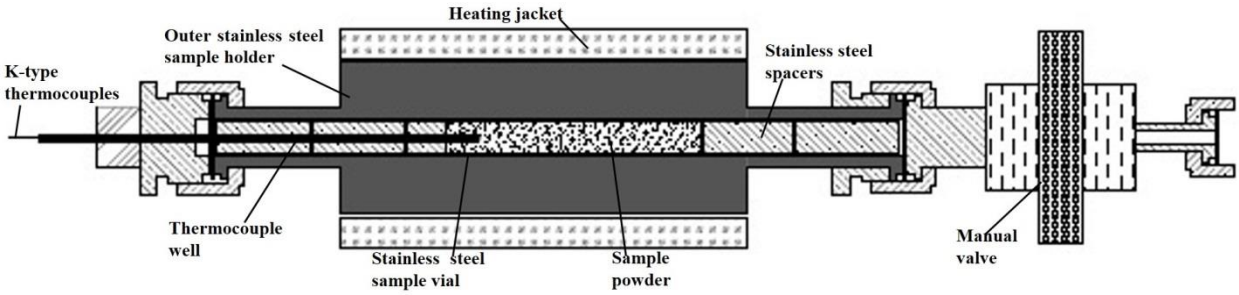

Figure 4. Schematic diagram of the cross section of the sample cell configuration.

analysis were performed by using the well-known Williamson-Hall equation, Eq. 8, which is a simplified breadth method where both size-induced and strain-induced broadening are deconvoluted by considering the peak width as a function of 2θ [108].

$$FW(\theta)\times\cos(\theta) = 4\times strain\times\sin(\theta) + \frac{K\lambda}{D} \qquad \text{Eq. 8}$$

where K stands for shape factor, which is a constant and taken as 0.9 here, λ is the X-ray wave-length, $FW(\theta)$ is the full width half maximum of the peak (FWHM) in radians with the instrumental broadening effect corrected, and θ is the position of the peak maximum. When plotting $FW(\theta)*Cos(\theta)$ against $Sin(\theta)$, the grain size and strain could be calculated via the intercept and slope of the plot.

4.2.3 Specific Surface Area

The specific surface area was measured using a TriStar 3020 surface area analyzer with a resolution of 0.01 m^2/g. During the measurement, helium was used as calibration gas and nitrogen as testing gas, and sample was immersed in liquid nitrogen to ensure low-temperature isothermal condition for the test. Brunauer Emmett Teller (BET) theory was applied for analyzing the surface area. Generalized from the Langmuir single layer absorption theory, BET theory incorporated the concept of multimolecular layer adsorption, with a fundamental assumption that the forces active in the condensation of gases are also responsible for the binding energy in multimolecular layer adsorption [109]. Sample was sealed before the measurement to minimize the possible influence of contamination on specific surface area.

4.2.4 Transmission Electron Microscopy (TEM)

Transmission Electron Microscopy imaging and selected area electron diffraction (SAED) analysis was performed on a JEOL 2010 LaB6 (CTEM only) transmission electron microscope operated at 200 kV, using a Gatan HHST4004 heating environmental vacuum cell transfer stage. For each specimen, a portion of powder was dry-transferred to a holey carbon coated 400 mesh Cu TEM grid, which was then loaded into the vacuum transfer stage. To avoid any exposure, the sample was retracted into the vacuum cell, which was then sealed off and pumped down to a roughing vacuum before transfer to the microscope.

4.2.5 Inductively Coupled Plasma Mass Spectrometry (ICP)

The Fe content was detected using an Agilent 7500ce Inductively Coupled Plasma quadrupole mass-spectrometer with a double-pass spray chamber, sapphire torch injector, platinum cones, and octopole reaction system. Helium gas with a flow rate of 4 mL/min in the collision cell was used to decrease the interference of ArO.

About 90 mg of sample were transferred into a preweighted acid-leached PTFE vial and digested with 10 % HNO_3 (Aristar Plus). The total dilution factor from the solid sample to the solution run in the ICPMS was ~6,000. All operations were performed in a laminar flow bench providing a dust-free environment. A calibration curve was measured using concentrations of 0, 0.2, 0,4, 1.1, and 10 mg Fe/L (Inorganic Ventures). Also, In was used as an internal standard with a final concentration of 20 mg/L in the diluted solution. Internal standard normalized intensities were fitted against the concentration for the calibration curve ($r^2 = 0.9999$), and the internal standard normalized intensities for the samples were blank corrected and interpolated using the linear fit, with an uncertainty of ca. 5%.

CHAPTER 5

ISOTHERMAL HYDROGENATION KINETICS OF MAGNESIUM HYDRIDE WITH TITANTIUM HYDRIDE ADDITIVE

5.1 Introduction

Magnesium hydride (MgH_2) is regarded as a promising material for not only hydrogen storage, but also thermal devices such as cooling and heating machines, heat pumps, and solar thermal storage systems. Magnesium hydride is low cost, and has a very high theoretical hydrogen storage capacity (7.6 wt.%) and high desorption enthalpy (74.5 kJ/mol H_2), and thus, high energy density [26, 92]. Practical applications of MgH_2 have been impeded, however, due to both the intrinsic thermodynamic stability of MgH_2 and the sluggish kinetic rates of dehydrogenation and hydrogenation of magnesium.

The kinetic behavior of MgH_2 can be improved by using mechanical ball milling to produce nano-scale particles, or by adding a transition metal alloy [110] or intermetallic compounds [25, 40] as catalytic additives. For example, Ti-based additives such as TiH_2 and $TiMn_2$ have been demonstrated as effective catalysts to allow MgH_2 to absorb hydrogen, even at room temperature [26]. In particular, Zhou et al. showed that the nano-sized MgH_2 with 5 at.% $TiMn_2$ additive can absorb 3 wt.% hydrogen at room temperature within 250 minutes under 1.0 bar H_2 pressure [25].These are extraordinary rates of hydrogenation. However, detailed studies of the kinetic behavior of these materials, i.e.,

MgH_2 with Ti-based additives, are still unavailable.

In general, there is a large body of research literature regarding the hydrogenation kinetics of commercially pure magnesium [28, 48, 111], and temperature is always one of the most important factors affecting the kinetics of hydrogenation and dehydrogenation. However, most of the studies in the past were conducted within temperature ranges from 200 to 400 ºC because the rate of hydrogenation of Mg is too slow to be readily measured at low temperatures, especially difficult at room temperature. For practical engineering applications such as on-board hydrogen storage for fuel cell vehicles, however, the low temperature range for hydrogenation or dehydrogenation would be far more important than the higher temperature ranges. Moreover, it is usually understood that the high-temperature kinetic behavior of MgH_2 may not be applicable to that of room temperature because rate-limiting steps could change as temperature varies [67, 98].

Another important issue in studies of the kinetics of hydrogenation, which has often been neglected in the literature, is the thermal gradient effect or self-heating phenomenon that can easily render a kinetics study inaccurate. Kinetics analysis is usually based on fitting kinetic data to various theoretical or empirical models. Most of these models, such as the Jander diffusion model and the volume contracting model, are based on isothermal assumptions, i.e., reaction should proceed at a constant temperature. It would be questionable to expect reliable mechanistic conclusions when interpreting kinetics data of a nonisothermal process using an isothermal kinetics model.

Unfortunately, an isothermal condition is usually difficult to maintain during hydrogenation due to the thermal gradient effect or self-heating phenomenon [28, 97]. The thermal gradient effect or self-heating phenomenon refers to the rise of temperature during

the initial stage of hydrogenation [28, 97], and is primarily an effect of the large exothermic hydrogenation reaction heat and the poor heat conductivity of the hydrogen storage materials. Due to insufficient heat dissipation from the hydrogen storage material, a large amount of heat released during hydrogenation will accumulate and raise the temperature of the material. This propels a faster reaction, resulting in the release of more heat, leading to considerable temperature rise. This significant self-heating phenomenon has been observed during hydrogenation as a temperature spike during the initial stage of the process. Moretto et al. reported that during hydrogenation of Mg-based materials, the sample temperature could rise by as much as 80 ºC in the initial hydrogenation period [28].

The effects of self-heating on the kinetics of hydrogenation have also been reported for studies of Mg_2Ni and $LaNi_5$ alloys [98-100]. Three methods have been primarily used to minimize the self-heating effect: using a smaller mass of sample [28], changing reaction vessel design, and/or adding thermal ballast [98]. Thermal ballast serves as a heat buffer, which not only accelerates the heat conduction but also absorbs the heat itself, thus minimizing the temperature fluctuation. Thermal ballast materials are required to have high thermal conductivity and high heat capacity, and should be inert to H_2 as well as the reaction materials.

In this work, we investigated the hydrogenation kinetic behavior of MgH_2-0.1TiH_2. The self-heating effect was characterized and minimized by using expandable graphite as the thermal ballast material to ensure isothermal conditions. Experiments were conducted at different temperatures within a low temperature range, from room temperature to 200 ºC. The JMA model was applied to describe the kinetic behavior, and an estimate was made of the activation energy of hydrogen adsorption in this system.

5.2 Experimental Details

The elements Ni, Al, Mn, and Cu have been reported as effective thermal ballasts for Mg_2Ni and $LaNi_5$ alloys [98, 99, 112]. However, these thermal ballasts are not suitable for Mg, since they may react with Mg. Song et al. confirmed that Ni would take part in the dissociation of H_2 during the hydrogenation process and affect the hydrogenation/dehydrogenation kinetics of Mg powder [112, 113]. In our preliminary trial tests, when copper was used as the thermal ballast, it was found that copper reacted with Mg to form a Mg-Cu alloy. Expandable graphite has also been reported as a good candidate for thermal ballast. It has excellent thermal conductivity, and is also inert in relation to Mg, Ti [114], and H_2 [115] under the temperature range from room temperature to 400 ºC. Expandable graphite was therefore chosen for this study. The expandable graphite (> 98%) employed in this study was purchased from Asbury Carbons (Asbury, NJ). Before being used, the graphite was degassed at 300 ºC for 3 h and stored under vacuum to avoid surface contamination before use.

The raw materials for this work, magnesium hydride (MgH_2, 98%) and titanium hydride (TiH_2, 99%), were purchased from Sigma-Aldrich (Milwaukee, WI) and Alfa-Aesar (Ward Hill, MA), respectively, and used without any further purification. It should be noted that the impurity content of the raw material can, in general, be quite significant, resulting in a lower H content in the raw material than the theoretical H content of MgH_2. All the material handling in the present study was carried out in a glovebox filled with purified argon (99.999%), which contained less than 1 ppm water vapor and 1 ppm oxygen, in order to minimize contamination.

Three grams of a mixture of MgH_2 and TiH_2, with a molar ratio of 10:1, were mixed

and milled via a custom-made ultrahigh-energy-high-pressure (UHEHP) ball milling device under a 150 bar hydrogen pressure. The milling was carried out at room temperature for 7 h using a ball-to-powder ratio of 110:1 by weight (approximately 10:1 by volume). After milling, the MgH_2-$0.1TiH_2$ powder was mixed by hand for 30 min, using ten times more expandable graphite by weight (i.e., the ratio of the expandable graphite to the MgH_2-$0.1TiH_2$ powder was 10:1 by weight).

The amount of expandable graphite required to minimize the temperature spike was estimated based on the temperature change and the hydrogen uptake observed in a nonisothermal hydrogenation test of MgH_2-$0.1TiH_2$, without the addition of expandable graphite. As shown in Figure 5, the sample was quickly heated due to the self-heating effect from the initial temperature of 100 ºC to the peak temperature of 111 ºC in as short as 9.3 seconds. Assuming the sample was perfectly insulated thermally without any heat dissipation, the calculated peak temperature rise would be 554 ºC based on the amount of H_2 absorbed within this short period of time (1.91 wt.% H_2), the hydrogenation reaction enthalpy, as well as the heat capacity of MgH_2-$0.1TiH_2$. Detailed calculation of peak temperature is given in Appendix B. Even though this estimation was based on a thermally isolated condition, it provided a reasonable approximation to determine how much graphite should be added. The estimated peak temperature rise decreased with increasing amounts of graphite, following the trend shown in Figure 6. As shown in the figure, the effect of graphite on reducing the undesired temperature rise becomes minute if the graphite is more than 10 times the MgH_2-$0.1TiH_2$. Furthermore, in the case of no addition of graphite, the observed temperature increase (11 ºC) was only about 1/50 of the estimated value (554 ºC), indicating that the major part of released heat was dissipated away via thermal conduction

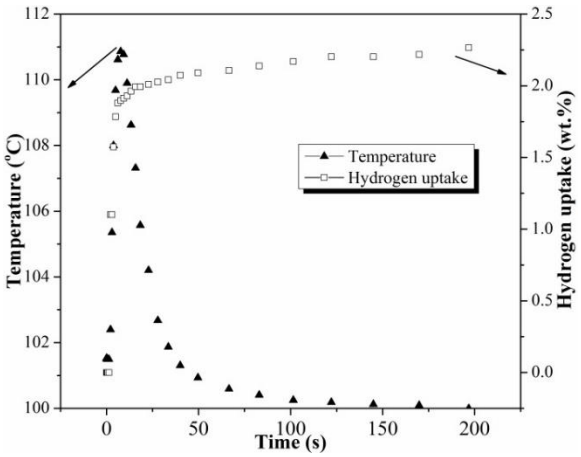

Figure 5. Temperature and H_2 uptake of nonisothermal hydrogenation at 100 ºC and 10 bar.

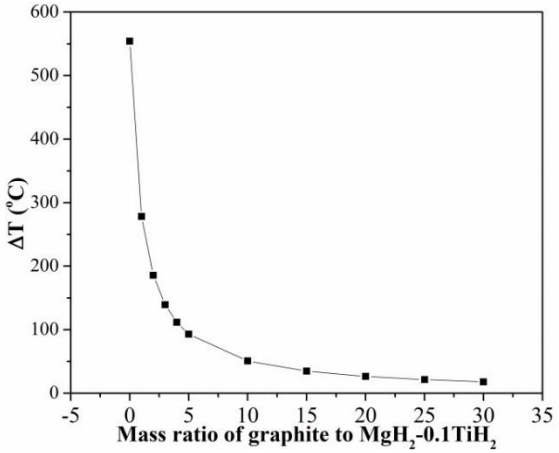

Figure 6. Estimated rise of peak temperature under conditions of thermal isolation.

through the sample holder and the PCT reactor. If a factor of 10 was used for the graphite to MgH_2-0.1TiH_2 ratio, the temperature spike was expected to be only approximately 1 ºC (1/50 of the estimated value of 51 ºC calculated according to Appendix B), suggesting that an amount of graphite addition beyond a factor of 10 would be unnecessary for the purpose of isothermal tests.

Hydrogenation kinetics measurements were performed using a commercial Sieverts type apparatus (PCTPro-2000). The hydrogenation kinetics of the material was evaluated for 5 different temperatures (25 ºC, 60 ºC, 100 ºC, 150 ºC, and 200 ºC). For each test run, the sample was fully dehydrogenated by holding at 300 ºC in vacuum for 1 h, followed by cooling to the required temperature to start the measurement of the hydrogenation kinetics. The pressure was fixed at 10 bar for all hydrogenation tests. As for the driving force of the hydrogenation kinetics, Ron [96] proposed a normalized pressure dependence method (NPDM) for kinetic rate evaluation of metal hydride formation and decomposition, suggesting that the pressure dependence function, i.e., the driving force, has a general form of $F(P)=|P_{eq}-P|/P$, where P and P_{eq} are the system pressure and the equilibrium pressure, respectively.

The equilibrium pressures of MgH_2 under different temperatures were estimated by the Van't Hoff equation:

$$ln\, P_{eq} = -\frac{\Delta H}{RT} + \frac{\Delta S}{R} \qquad \text{Eq. 9}$$

Based on the enthalpy and entropy of the hydrogenation reaction reported by Zhou et al. [25], which is 75.24 kJ/mol H_2 and 135.14 J/K.mol H_2, respectively, the equilibrium pressure and pressure dependence factor $F(P)$ is listed in Table 9. The values of the pressure dependence factor $F(P)$ are 1, 0.999998, 0.99996, 0.9994, and 0.994 at

Table 9. Equilibrium pressure of MgH_2-0.1TiH_2 and corresponding pressure dependence factor *F(P)* at different temperatures.

Temperature (ºC)	25	60	100	150	200
Estimated Equilibrium Pressure P_{eq} (bar)	7.54×10^{-7}	1.83×10^{-5}	3.36×10^{-4}	5.9×10^{-3}	5.6×10^{-2}
Pressure Dependence Factor *F(P)*	1	0.999998	0.99996	0.9994	0.994

temperatures of 25, 60, 100, 150, and 200 ºC, respectively, as shown in Table 9. It can be seen that these values for *F(P)* are all approximately equal to 1, and, for convenience, the pressure dependence factor *F(P)* is treated as equal to 1 in the remainder of this work.

5.3 Results and Discussions

5.3.1 Temperature Spike

The effect of adding expandable graphite to minimize the temperature spike is clearly demonstrated in Figure 7, in which the changes of temperature and hydrogen uptake in the hydrogenation tests at 100 ºC are plotted for the samples with and without expandable graphite. After adding expandable graphite, the temperature spike was dramatically decreased from 11 ºC to 1.2 ºC. For a thermally activated hydrogenation reaction, the dependence of the reaction rate constant, k, on temperature can be expressed by the Arrhenius' equation:

$$k = A\exp(-\frac{E_a}{RT}) \qquad \text{Eq. 10}$$

where k is the reaction rate constant at the temperature T, E_a is activation energy, R is gas constant, and A is pre-exponent factor. The reaction rate k increases with temperature. The error in the hydrogenation rate constant k due to temperature deviation can be estimated in order to demonstrate that adding expandable graphite is effective in maintaining an isothermal condition. The change of reaction rate due to temperature change, ΔT, can be calculated by:

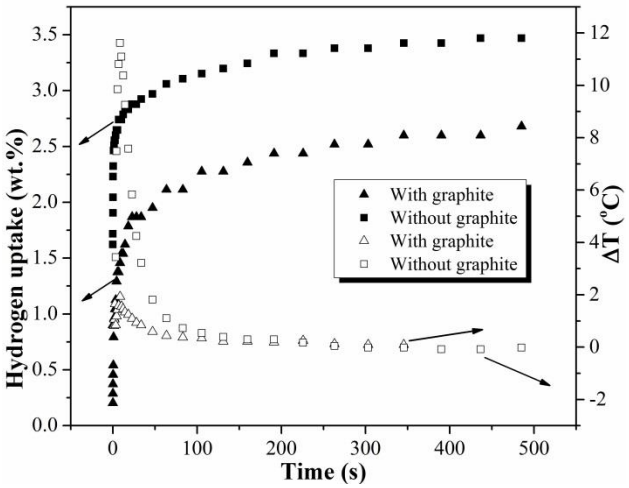

Figure 7. H_2 uptake and temperature profiles of samples with and without expandable graphite hydrogenated at 100 ºC and 10 bar.

$$k_{Error} = \frac{k_{(T+\Delta T)} - k_{(T)}}{k_{(T)}} \times 100\% = (\frac{k_{(T+\Delta T)}}{k_{(T)}} - 1) \times 100\% = \{\exp\left[\frac{E_a}{R}\left(\frac{1}{T} - \frac{1}{T+\Delta T}\right)\right] - 1\} \times 100\% \quad \text{Eq. 11}$$

Based on the activation energy of hydrogenation (17.9 kJ/mol H_2), the error in the reaction rate constant k due to the observed temperature spike at 100 ºC (11 ºC) of the nonisothermal hydrogenation process was calculated to be 16.52 %. After expandable graphite was added, the error in reaction rate was estimated to be merely 2.3 % due to the much smaller temperature spike.

For the samples with expandable graphite, the temperature spikes observed in the hydrogenation tests at other temperatures were also very small with respect to their corresponding test temperature. As shown in Figure 8, temperature spikes of 0.1, 1.0, 1.2, 1.5, and 1.9 ºC were observed for hydrogenation tests at 25, 60, 100, 150, and 200 ºC, respectively. Corresponding to the above, the estimated errors of reaction rate constant k were 0.24 %, 1.93 %, 1.85 %, 1.80 %, and 1.82 %, respectively. These are very small errors and they suggest that the hydrogenation kinetics of MgH_2-0.1TiH_2, at a 1:10 ratio with expandable graphite, can be regarded as isothermal or at least near isothermal.

5.3.2 Hydrogenation Rate

In addition to the observed significant difference in temperature spikes between the isothermal (i.e., with expandable graphite) and the nonisothermal tests (i.e., without expandable graphite), the hydrogenation rate under these two conditions was also found to be quite different from each other. As shown in Figure 7, the amount of hydrogen absorbed by the sample without expandable graphite was considerably larger than that absorbed by

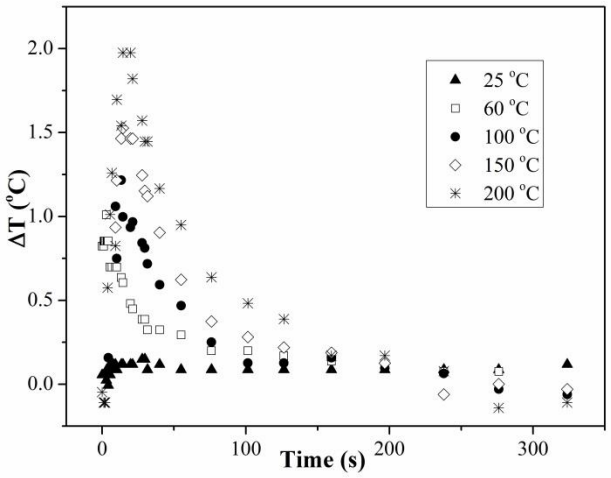

Figure 8. Temperature profiles of samples with expandable graphite hydrogenated at various temperatures.

the sample with expandable graphite after the same period of reaction time. For example, after 500 seconds of hydrogenation, 3.5 wt.% of hydrogen was absorbed in the nonisothermal test, while only 2.6 wt.% was absorbed in the isothermal test. The difference in the amount of absorbed hydrogen between the two cases was found to exist primarily in the first few tens of seconds, indicating that during this period, the hydrogenation rate under a nonisothermal condition was considerably larger than that under an isothermal condition. However, hydrogenation rates after this short initial stage were nearly the same in both cases.

The higher hydrogenation rate in the initial stage under a nonisothermal condition can be attributed to the accelerated reaction, due to the significant self-heating effect. In the nonisothermal tests, the reaction rate varied considerably in the initial stage due to drastic temperature spikes caused by the strong exothermic hydrogenation reaction of magnesium. Therefore, the reaction rate observed in the initial stage of the nonisothermal test is not the true reaction rate at the set point temperature; rather, it should be higher than the true reaction rate. After the initial stage, the relatively slow reaction in comparison to that in the initial stage resulted in a slower rate for the release of heat. As soon as the rate of heat release became smaller than the rate of heat dissipation, the sample temperature would start to drop from the peak value and gradually move back to the set point, and the reaction rate would thus decrease to a lower value corresponding to the set point temperature. For the isothermal test, since the sample temperature was almost the same as the set point temperature, even in the initial stage, the observed reaction rate was considered to be close enough to the true reaction rate for the set point temperature. The true reaction rate would be useful for interpreting reaction kinetics. In the following sections, only the kinetics data

under isothermal conditions (i.e., for samples with expandable graphite) was used for analysis and modeling.

5.3.3 Hydrogenation Rates at Different Temperatures

Hydrogenation curves (i.e., the hydrogen uptake as a function of time) at different temperatures under isothermal conditions are plotted in Figure 9. As shown in Figure 9, after any given period of time, the hydrogen uptake increased with increasing temperature, demonstrating the expected strong dependence of reaction rate on temperature.

The hydrogenation curves at different temperatures indicated a common trend that the reaction rate in the initial hundreds of seconds was much higher than that in the later stage. The difference in the hydrogenation curves at different temperatures primarily resulted from the difference of reaction rate in the short initial period of time. The initial higher reaction rate at higher temperature resulted in a larger hydrogen uptake and the gaps between the hydrogenation curves of different temperatures existed primarily in the initial stage. As the reaction proceeded, the difference between the data of the 200 ºC and 150 ºC samples became very small; Figure 9. Theoretically, hydrogenation under any given temperature would reach the hydrogen capacity of the material, which is the maximum possible amount of hydrogen that a material can absorb, if sufficiently long reaction time is allowed. The higher the temperature is, the faster the hydrogenation rate is. The 200 ºC hydrogenation rate was sufficiently fast and the hydrogen uptake was close to the material's hydrogen capacity at the end of the 1 h run, followed by the 150 ºC hydrogenation, which was slower than the 200 ºC hydrogenation in the initial stage, but reached approximately similar saturation as that at 200 ºC after 1 h. For hydrogenation at lower

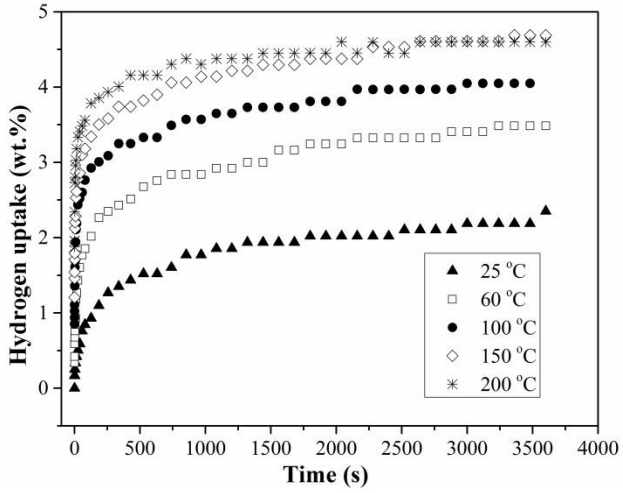

Figure 9. Hydrogenation curves at different temperatures under isothermal conditions.

temperatures (100, 60, and 25 ºC), a much longer time would be needed to reach the hydrogen capacity of the material. However, the hydrogenation experiments were not conducted for times longer than 1 h in this study because the thermal gradient effect is most pronounced within the first 1 h, or even the first few minutes. The main focus of the present study was to understand the effects of the thermal gradient in the initial stage of the reaction. Further studies, however, are necessary to precisely determine the time necessary for hydrogenation to reach the material's hydrogen capacity at low temperatures.

5.3.4 Kinetics Analysis

Various kinetic models have been proposed to interpret the hydrogenation kinetics of different hydrogen storage materials. Based on the assumption of a rate-limiting step of hydrogenation, which could be surface physical sorption, surface penetration, diffusion, chemical absorption, and/or other processes, a kinetic model can be established to describe the fraction of hydrogenation reaction as a function of time [116]. Sabitu et al. studied the hydrogenation kinetics of TiH_2-, Mg_2Ni-, and Nb_2O_5–doped MgH_2 and concluded that the most likely mechanism was a 3-D moving boundary [74]. Montone et al. modeled the hydrogenation kinetics of Fe-doped MgH_2 with the JMA model and considered that the hydrogenation process could be controlled by either a 1-D interface reaction or a 2-D diffusion process [117]. The popular models for hydrogenation of metal hydrides are summarized in Table 10. In the kinetic equations listed, ξ stands for the reaction fraction after a certain period of reaction time t; k the reaction rate constant; and n is the Avrami exponent, related to the system geometry. The left-hand side of each kinetic equation is referred to as the model parameter, e.g., $ln(-ln(1-\xi))$ is the model parameter in the

Table 10. Kinetic models applied for hydrogenation.

Model	Kinetic equation	Reference
Johnson-Mehl-Avrami (JMA)	$ln(-ln(1-\xi))=ln(k)+nln(t)$	[60, 92, 105, 118, 119]
Jander diffusion model (JMD)	$(1-(1-\xi)^{1/3})^2=kt$	[92, 105, 116, 119]
1-D diffusion	$\xi^2=kt$	[105, 119]
2-D diffusion (Bidmensional particle shape)	$(1-\xi)ln(1-\xi)+\xi=kt$	[105, 119]
3-D diffusion (Ginsling-Braunshteinn model)	$(1-2\xi/3)-(1-\xi)^{2/3}=kt$	[105, 119]
2-D contracting area	$1-(1-\xi)^{1/2}=kt$	[105, 119]
3-D contracting volume	$1-(1-\xi)^{1/3}=kt$	[105, 119]

Johnson-Mehl-Avrami (JMA) model.

In order to determine which of the kinetic models could be used effectively to interpret the hydrogenation kinetics of MgH_2-0.1TiH_2, all the models listed in Table 10 were used to fit the kinetics data obtained under isothermal conditions. It was found that only the JMA model fit the hydrogenation kinetics of MgH_2-0.1TiH_2, while the other five models did not.

In order to compare the hydrogenation kinetics, data at 100 °C were fit by the 2- and 3-D contracting models, as well as the 1- and 2-D diffusion models as shown in Figure 10 a), and the Jander diffusion and the 3-D diffusion models as shown in Figure 10 b). In these figures, the model parameter of each model was plotted as a function of time. If a model satisfactorily describes the hydrogenation kinetics, the plot of its model parameter versus time should be linear. None of the five plots could be best fit by a straight line, suggesting that none of the five models could be effectively used to interpret the hydrogenation kinetics of MgH_2-0.1TiH_2.

In Figure 11, the model parameter of the JMA model, $ln(-ln(1-\xi))$, was plotted against the natural logarithm of the reaction time, $ln(t)$, to evaluate the suitability of this model. Clearly, the kinetic data of this work for all the temperatures under isothermal conditions can be best fit by straight lines, suggesting that among the models listed in Table 10, the JMA model was the best numerical model for use in interpreting the hydrogenation kinetics of MgH_2-0.1TiH_2.

The values of the reaction rate constant k at different temperatures from the best-fits of the kinetic data under isothermal conditions are listed in Table 11. The data show that the hydrogenation rate increases with increasing temperature.

As mentioned earlier, hydrogenation under nonisothermal conditions is quite

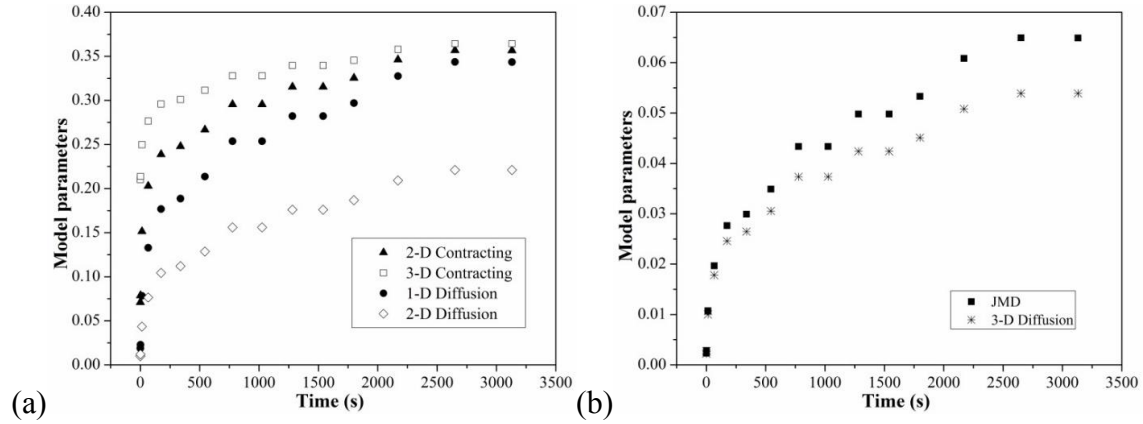

Figure 10. Plots of the model parameters versus time of a) the 2- and 3-D contracting models, and the 1- and 2-D diffusion models; b) the Jander diffusion model and the 3-D diffusion model. Note the y-axis scale is different for a) and b). Data were obtained at 100 ºC under isothermal conditions starting from t=1 s.

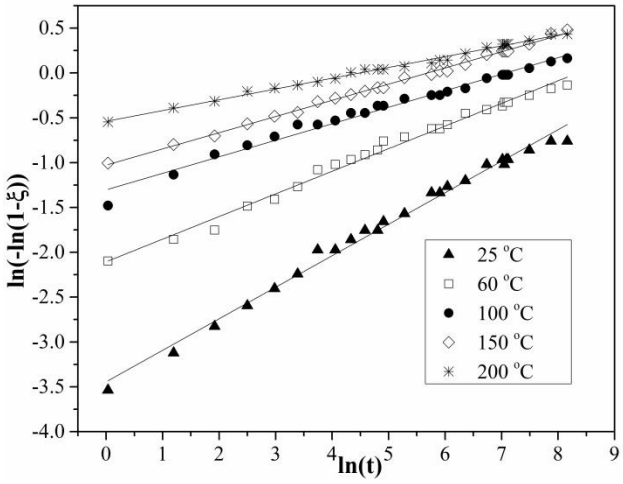

Figure 11. The JMA model parameters plotted against *ln(t)*. Data were those from all tested temperatures under isothermal conditions and started from *ln(t)*=0 (t=1 s).

Table 11. Values of the reaction rate constant k from the best-fit of hydrogenation kinetic data using the JMA model at different temperatures under isothermal conditions.

T, °C	24.20	65.30	104.50	153.47	201.84
ln(k)	-3.377	-2.0789	-1.2843	-1.0589	-0.6534

different from that under isothermal conditions, due to the difference of temperature deviation in the initial stage of hydrogenation, as demonstrated in Figure 7. It is worthwhile, however, to examine whether the kinetic data under nonisothermal conditions can also be described by the JMA model. In Figure 12, plots of the JMA model parameters are drawn for the two groups of kinetics data at different temperatures. Obviously, while the isothermal data can be best fit by the JMA model as straight lines, the nonisothermal data appear to be nonlinear for most temperatures, suggesting that the JMA model is not suitable for interpreting the nonisothermal hydrogenation kinetics of MgH_2-0.1TiH_2. This is easily understood because the JMA model, as most other kinetic models, is established based on the assumption of isothermal conditions. It would therefore be unlikely to use the JMA model to interpret the kinetic data under nonisothermal conditions. It demonstrates again that self-heating during hydrogenation can render kinetic analyses inaccurate and isothermal conditions are necessary for effectively studying hydrogenation kinetics.

In order to evaluate the activation energy of hydrogenation of MgH_2-0.1TiH_2, the reaction rate constant k at different temperatures, obtained from the JMA model best-fit of the isothermal kinetics data, as listed in Table 11, were collected to draw the plot of *ln(k)* versus *1000/T* in Figure 13. According to Eq. 9, the activation energy can be calculated using the slope of the plotted line. In this work, the hydrogenation activation energy of MgH_2-0.1TiH_2 was calculated to be 17.9 kJ/mol H_2 within the temperature range from room temperature to 200 ºC.

The activation energy obtained in the present study may be more reliable than those of alternate methodologies for the MgH_2-0.1TiH_2 system, considering the facts that a) the hydrogenation tests were conducted under nearly isothermal conditions that minimized the

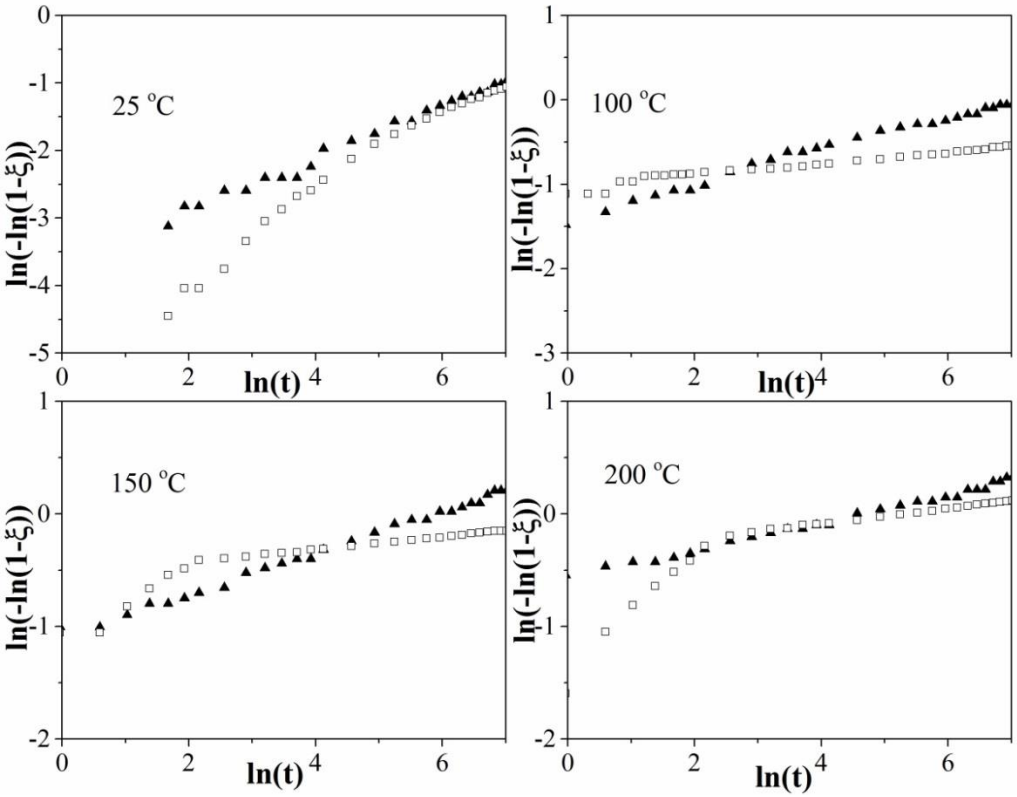

Figure 12. Comparison between two cases, where the JMA model was used to fit the two groups of kinetic data, one for isothermal conditions (solid triangles) and the other for nonisothermal conditions (open squares).

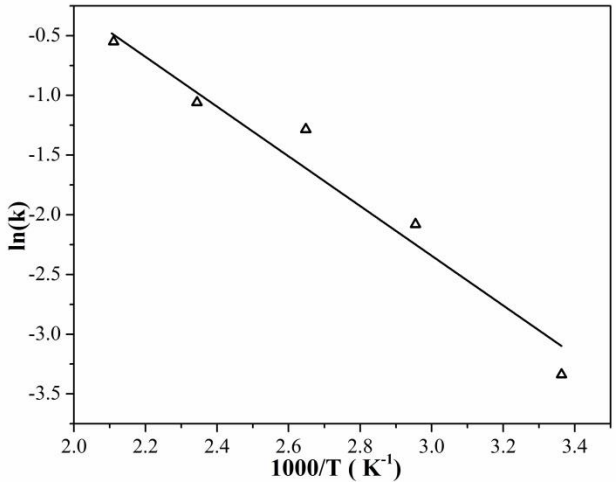

Figure 13. Plot of *ln(k)* versus *1000/T* used to evaluate the activation energy of hydrogenation of MgH_2-0.1TiH_2.

self-heating effect on the kinetics measurement, and b) the kinetics data were obtained over a wider temperature range.

The activation energies for hydrogen diffusion in magnesium and magnesium hydride have been reported to be 40 kJ/mol H_2 and 98-166 kJ/mol H_2, respectively [61]. Both are much larger than the activation energy of hydrogenation of MgH_2-0.1TiH_2 calculated in this work, 17.9 kJ/mol H_2, implying that hydrogen diffusion is not the rate-limiting step in the hydrogenation of MgH_2-0.1TiH_2. Further studies, however, are necessary to achieve a comprehensive understanding of this issue.

5.4 Summary

The hydrogenation kinetics of MgH_2-0.1TiH_2 was studied under isothermal conditions where the self-heating effect was minimized. The key results are summarized as follows:

1. There was a significant temperature spike in the initial stage of hydrogenation of MgH_2-0.1TiH_2 due to the heat released from the exothermic reaction.
2. The addition of a sufficient amount of expandable graphite proved to be effective in minimizing the temperature spike and establishing the isothermal conditions for the kinetics study.
3. The hydrogenation kinetics under isothermal conditions were significantly different from those under nonisothermal conditions.
4. The hydrogenation kinetics of MgH_2-0.1TiH_2 under nearly isothermal conditions can be described numerically by the JMA model.

5. The activation energy of hydrogenation of MgH_2-0.1TiH_2 was calculated to be 17.9 kJ/mol H_2, which is much lower than the activation energy of hydrogen diffusion in magnesium and magnesium hydride.

CHAPTER 6

EFFECT OF MILLING PARAMETERS, CATALYST, TEMPERATURE, AND PRESSURE ON HYDROGENATION KINETICS OF MAGNESIUM HYDRIDE

6.1 Introduction

Hydrogenation is important in the application of magnesium hydrides, such as hydrogen storage, thermal storage, battery, etc. [12, 18]. As we discussed above in Chapter 2, the sluggish hydrogenation kinetics in the past has been a major hurdle to realize practical application [29, 38, 45]. Over the recent decades, however, ball milling and adding additives has been recognized as two major paths to improve the kinetics of magnesium hydrides [25, 46, 61].

As the most widely accepted method to prepare magnesium hydrides, ball milling was proved to be effective in facilitating the hydrogenation kinetics of magnesium hydrides [48, 103], which could possibly alter the mechanism of hydrogenation as a result. According to the literature, the hydrogenation kinetics study of pure magnesium hydrides dated back to 1955, when Ellinger et al. [101] concluded it obeyed the second order rule. Later Kennelley et al. [37] claimed that the hydrogenation of pure magnesium is a first order reaction. In 1976, Stander [102] reported the process was initially controlled by a surface reaction then diffusion. However, after the ball milling technique was introduced in magnesium hydrides

preparation, Huot et al. contended that diffusion was the only control step for hydrogenation of magnesium hydrides [48].

Adding a catalyst could considerably improve the hydrogenation kinetics of magnesium hydride as well [46, 57-59], which in return, might change the hydrogenation mechanism. Lu et al. [26] found the first order rate law can best describe the hydrogenation kinetics of ball-milled magnesium with TiH_2 as catalyst, and the calculated activation energy was 16.4 kJ/mol H_2. Zhou et al. [25] compared the effect of Ti-base intermetallic compounds on the hydrogenation kinetics of ball-milled magnesium hydrides; the calculated activation energy varied from 20.6-25.5 kJ/mol H_2 using the Johnson-Mehl-Avrami (JMA) model. Tan et al. [60] prepared thin film magnesium hydride with Nb-V alloys as catalyst, and suggested to interpret the hydrogenation kinetics as a two-stage procedure using the JMA rate law. Barkhordarian et al. [103] concluded that the hydrogenation of Nb_2O_5 catalyst magnesium hydrides was controlled by diffusion, after fitting the kinetics data with different kinetics models.

Moreover, few kinetic studies of magnesium hydrides were based on isothermal condition. Due to the self-heating phenomenon, it was very difficult to maintain an isothermal condition during hydrogenation of magnesium hydrides [28, 97]. Caused by the inherent high enthalpy and low thermal conductivity of magnesium hydrides, self-heating occurs as a sample is heated up by the released reaction heat during an exothermic reaction. Temperature would increase considerably during hydrogenation, especially for materials that have excellent kinetics and those scaled-up magnesium hydrides tanks [28]. To some extent, self-heating is favored in practical application, because it can start and accelerate the reaction. In kinetics studies, however, a substantial temperature deviation would lead

to unreliable kinetics analysis [98, 99, 112]. Recently, Li et al. [120] used expandable graphite as thermal ballast to absorb excessive reaction heat and facilitate heat transfer, which was effective in minimizing the self-heating phenomenon and thus allows for more accurate kinetics analysis.

In this chapter, various milling parameters and different catalysts were used to prepare ball-milled magnesium hydrides, of which hydrogenation kinetics has been examined, as well as other properties such as grain size, surface area, phase composition, and morphology. Different models were further employed to understand the mechanism of hydrogenation, as well as how hydrogenation was affected by grain size and hydrogenation condition. In the following section, all of the kinetics studies were conducted under isothermal conditions as described in Chapter 5.

6.2 Experimental Details

MgH_2 and TiH_2 were used as received, while $TiMn_2$ and 75V-5Ti-20Cr were activated before using. The thermal ballast, graphite, had gone through a degassing procedure before being mixed with ball-milled magnesium hydrides. See Table 8 and section 0 for more detailed information of materials used in this chapter. The mixture of magnesium hydrides with/without catalyst was milled via a custom-made ultrahigh-energy-high-pressure (UHEHP) ball milling device under a 150 bar hydrogen pressure. Samples milled with different milling parameters and catalysts were prepared and listed below; see Table 12. After milling, magnesium hydrides with/without catalyst were mixed by hand for 30 min, using ten times more expandable graphite by weight (i.e., the ratio of the expandable graphite to the MgH_2-0.1TiH_2 powder was 10:1 by weight). All the materials handling was

Table 12. Sample preparation parameters.

Sample No.	Catalyst	Milling Time (h)	Milling Load (g)
1	None	0.5	3
2		2	
3		4	
4		6	
5	10 mol.% TiH_2	0.5	
6		2	
7		4	
8		6	
9			10
10			15
11	5 mol.% $TiMn_2$	2	3
12		4	
13		6	
14	5 mol.% 75VTiCr	2	
15		4	
16		6	

conducted inside or sealed before taken out from the glovebox, which is filled with argon (99.999 %) and contains less than 1 ppm oxygen and moisture inside, in order to minimize contamination.

The hydrogenation kinetics measurement was performed on a commercial Sieverts type apparatus (PCTPro-2000). See Figure 4 for the detailed sample cell configuration. It should be noted that sample had gone through three hydrogenation/dehydrogenation cycles to eliminate the residual stress caused by the milling process. The influence of driving force during hydrogenation, especially at higher hydrogenation temperature, has been corrected using a normalized pressure dependence method (NPDM) put forward by Ron in 1999 [96]. Phase analysis was carried out using high-energy X-ray diffraction (XRD) in Advanced Photon Source (APS), Argonne National Laboratory. Grain size and strain analysis based on the X-ray diffraction was performed using the Williamson-Hall equation. Specific surface area was measured using a TriStar 3020 surface area analyzer with nitrogen gas and was analyzed using BET theory. Iron content was detected using an Agilent 7500ce Inductively Coupled Plasma Mass Spectroscopy. Particle microscopy was examined using a JEOL 2010 LaB6 Transmission Electron Microscope (TEM) and grain size was calculated via dark field images.

6.3 Results

6.3.1 Grain Size

Ball milling is the major sample preparation process in this work. Thus the parameter of balling milling could have a significant effect on the material properties, such as grain size, specific surface area, phase, and morphology. There are various milling parameters,

including milling time, milling load, ball to sample ratio, rotating speed, etc. In this session, we will mainly focus on the effect of milling load and milling time on hydrogenation kinetics.

Grain size could be calculated based on the peak broadening of the X-ray diffraction patterns using Williamson-Hall equation, Eq. 8, which is described earlier in section 4.2.2. See Figure 14 as an example for the grain size calculation, where $FW(\theta)*Cos(\theta)$ was plotted against $Sin(\theta)$. The grain size could be calculated via the intercept of the Williamson-Hall plot, according to the Williamson-Hall equation, Eq. 8. More data regarding peak fitting and $FW(\theta)$ used in calculation are attached in Appendix C. See Figure 15 and Table 13 for the calculated grain size of each sample.

By comparing the calculated grain size of pure MgH_2 (open triangle), MgH_2-TiH_2 (solid square), MgH_2-$TiMn_2$ (open circle), and MgH_2-VTiCr (solid triangle), an obvious trend shows that sample milled for a longer amount of time has smaller grain size. Moreover, the grain size of MgH_2-TiH_2, MgH_2-$TiMn_2$, and MgH_2-VTiCr are smaller than that of pure MgH_2 milled for the same amount of time, except for one data point, MgH_2-VTiCr milled for 6 h, of which the grain size is slightly bigger than that of pure MgH_2. This comparison indicates that additives (TiH_2, $TiMn_2$, and VTiCr in this work) might serve as a milling aid and assist in reducing grain size of MgH_2.

Grain size was also analyzed via the TEM dark field image; Figure 16. Most of the Mg and TiH_2 (and MgO) diffraction rings are in very close proximity, or even overlap, and cannot be isolated using an objective aperture to form dark-field images. The primary rings of each, for example, cannot be used. Mg (102) is the strongest Mg diffraction ring that does not overlap and is used for the grain size analysis. See Table 14 for the calculated

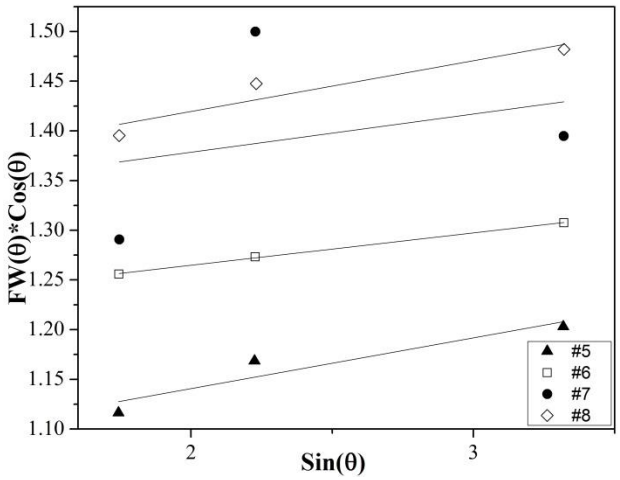

Figure 14. Williamson-Hall plot of samples #5-8, MgH_2-TiH_2 milled by different milling time.

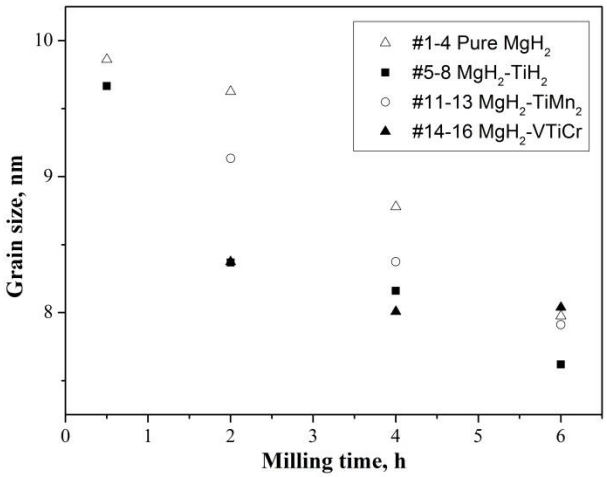

Figure 15. Grain size of pure MgH_2, MgH_2-TiH_2, MgH_2-$TiMn_2$, and MgH_2-VTiCr.

Table 13 Calculated grain size of each sample #1-16.

Sample No.	Grain Size (nm)	Catalyst	Milling Time (h)	Milling Load (g)
1	9.86	None	0.5	3
2	9.63		2	
3	8.78		4	
4	7.98		6	
5	9.67	10 mol.% TiH_2	0.5	
6	8.37		2	
7	8.16		4	
8	7.62		6	
9	10.95			10
10	12.51			15
11	9.14	5 mol.% $TiMn_2$	2	3
12	8.37		4	
13	7.91		6	
14	8.37	5 mol.% 75VTiCr	2	
15	8.01		4	
16	8.04		6	

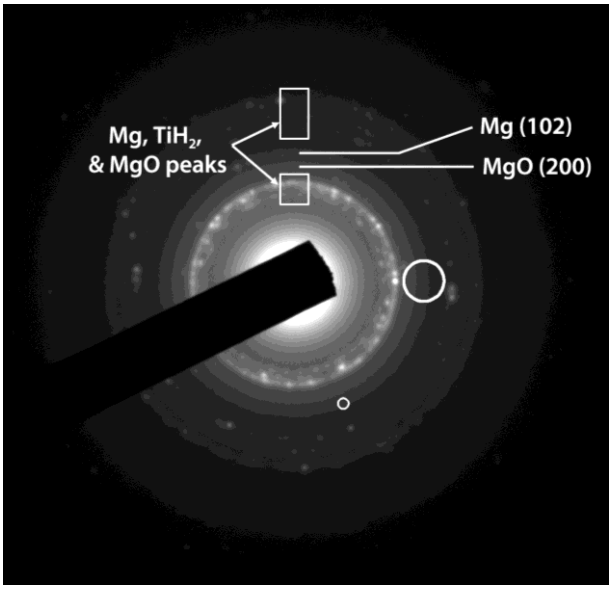

Figure 16. The dark field image of sample #8, MgH_2-TiH_2.

Table 14. Grain size of MgH_2-TiH_2 samples #8-10 calculated by XRD and TEM method.

Grain size (nm)	#10	#9	#8	#10:#9:#8
XRD	12.5	11.9	7.8	1.6:1.5:1
TEM	21.5	19.5	13.5	1.6:1.4:1

grain size of samples milled with different milling load, sample #8-10. The grain sizes of sample #8-10 obtained via XRD and TEM do not match in value, which is 12.5, 11.9, and 7.8 nm from XRD and 21.5, 19.5, and 13.5 nm from TEM, respectively. However, these two sets of grain size are consistent in portion, which is 1.6:1.5:1 via XRD and 1.6:1.4:1 via TEM. It is understandable that the deviation in actual value of the grain size could possibly stem from the machine configuration, analysis standard error, and data processing. However, with the same experimental and analysis method (XRD or TEM), the relative portion of grain size for different samples should be consistent. Therefore, the author tends to believe the distribution of grain size for these three samples, sample #8-10, is reliable.

6.3.2 Specific Surface Area

The specific surface area of sample #1-10, 12, and 15 is shown in Figure 17. Compared to a 0.5 m^2/g specific surface area of as-received powders, half-hour milling created a much higher specific surface area of 8.8 m^2/g. As milling time increases, the specific surface area of the milled powder will continue to increase and reach a maximum value (9.8 m^2/g for pure MgH_2 milled for 4 h and 10.1 m^2/g for MgH_2-TiH_2 milled for 2 h) and then gradually decrease. A speculation is that milling will, on one hand, break the large particles into smaller ones of the as-received materials; thus, it has an effect of increasing the specific surface area. On the other hand, it will press particles together and causes agglomeration; thus, it has an effect of reducing the specific surface area. When there is a bigger portion of large particles, the breaking effect dominates and the specific surface area will increase as milling time increases. Until a certain point that the breaking effect is equivalent to the pressing effect, sample will have the maximum value for specific surface

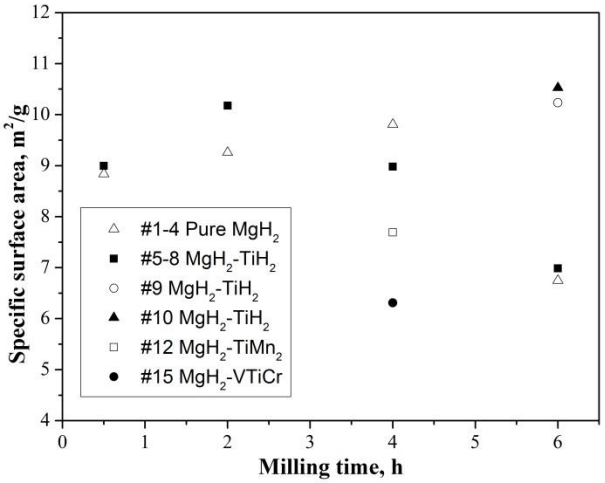

Figure 17. Specific surface area of magnesium hydrides with different processing variables and catalysts.

area. After that, the pressing effect dominates and larger particles of agglomeration will form, reflected as a decreasing specific surface area as milling time increases. From the comparison of specific surface area shown in Figure 17, adding TiH_2 caused sample to reach maximum specific surface area in 2 h, compared to 4 h for pure magnesium hydrides. In addition, adding catalyst did not show a certain effect on the specific surface area, as we compare the specific surface area of pure MgH_2, MgH_2-TiH_2, MgH_2-$TiMn_2$, and MgH_2-VTiCr milled for the same amount of time.

6.3.3 Phase Composition Analysis

The X-ray diffraction pattern was obtained for the pure MgH_2 and MgH_2-TiH_2 milled with different length of time as well; see Figure 18 and Figure 19. Besides the most stable phase of magnesium hydrides, β MgH_2, there is a certain amount of γ MgH_2 in the as-milled powder, even for the sample milled for only half an hour. For both pure MgH_2 and MgH_2-TiH_2, as milling time increases, the relative peak intensity of γ MgH_2 increases in comparison with β MgH_2, indicating the longer milling time could lead to a higher γ MgH_2 content in the as-milled powder. Moreover, the peak broadening increases as milling time is extended, implying that the longer the milling time, the more amorphous the as-milled powder. In addition, a small peak of iron is identified in the X-ray diffraction pattern, suggesting that a certain amount of iron might exist in the as-milled sample, which is consistent with the ICP test and will be discussed latter in section 6.4.3.

See Figure 20 for the X-ray diffraction pattern of sample #8-10 milled with different milling load. Regarding the relative intensity, the X-ray pattern of these three samples is very similar, showing the appearance of β MgH_2, γ MgH_2, TiH_2, and certain iron content.

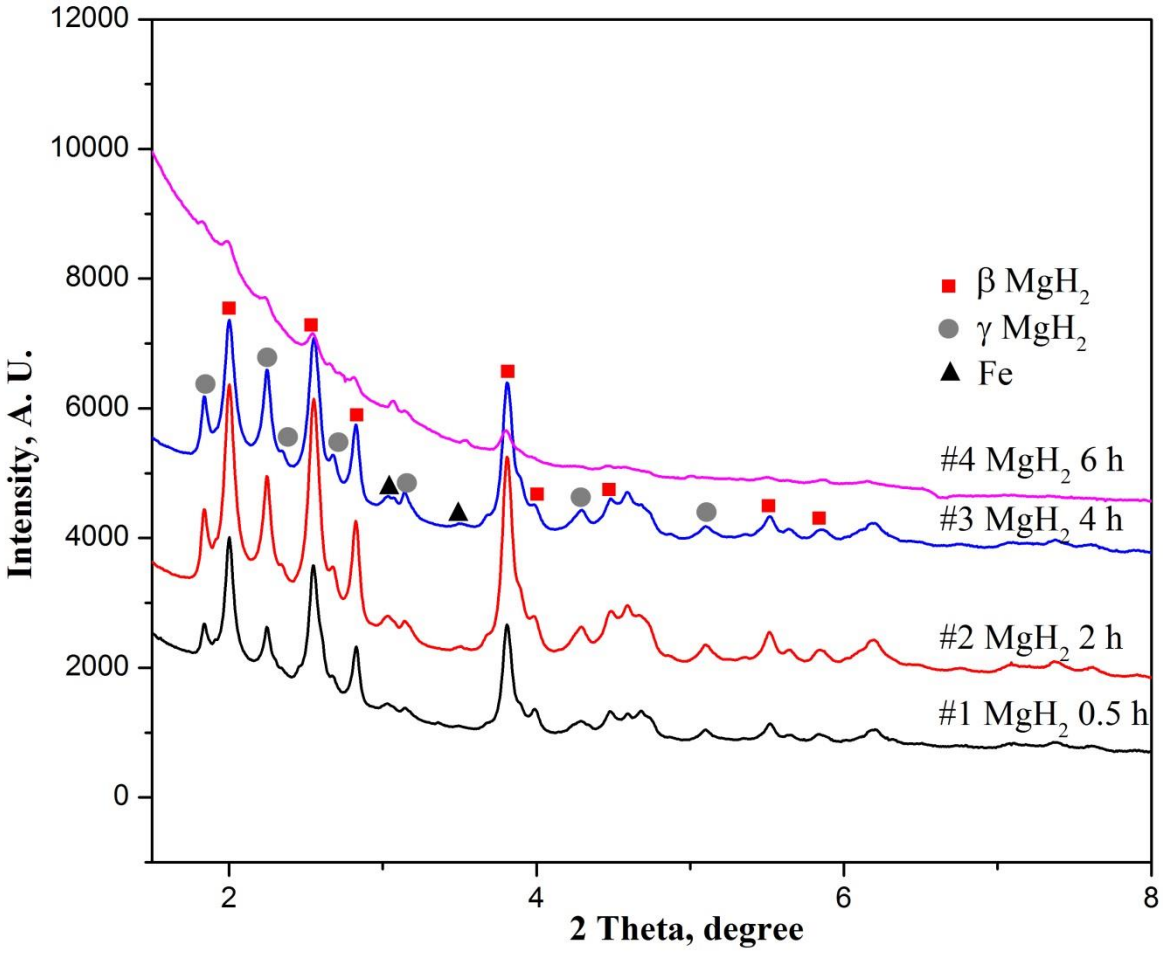

Figure 18. X-ray diffraction pattern of pure MgH_2 with different grain size, sample #1-4.

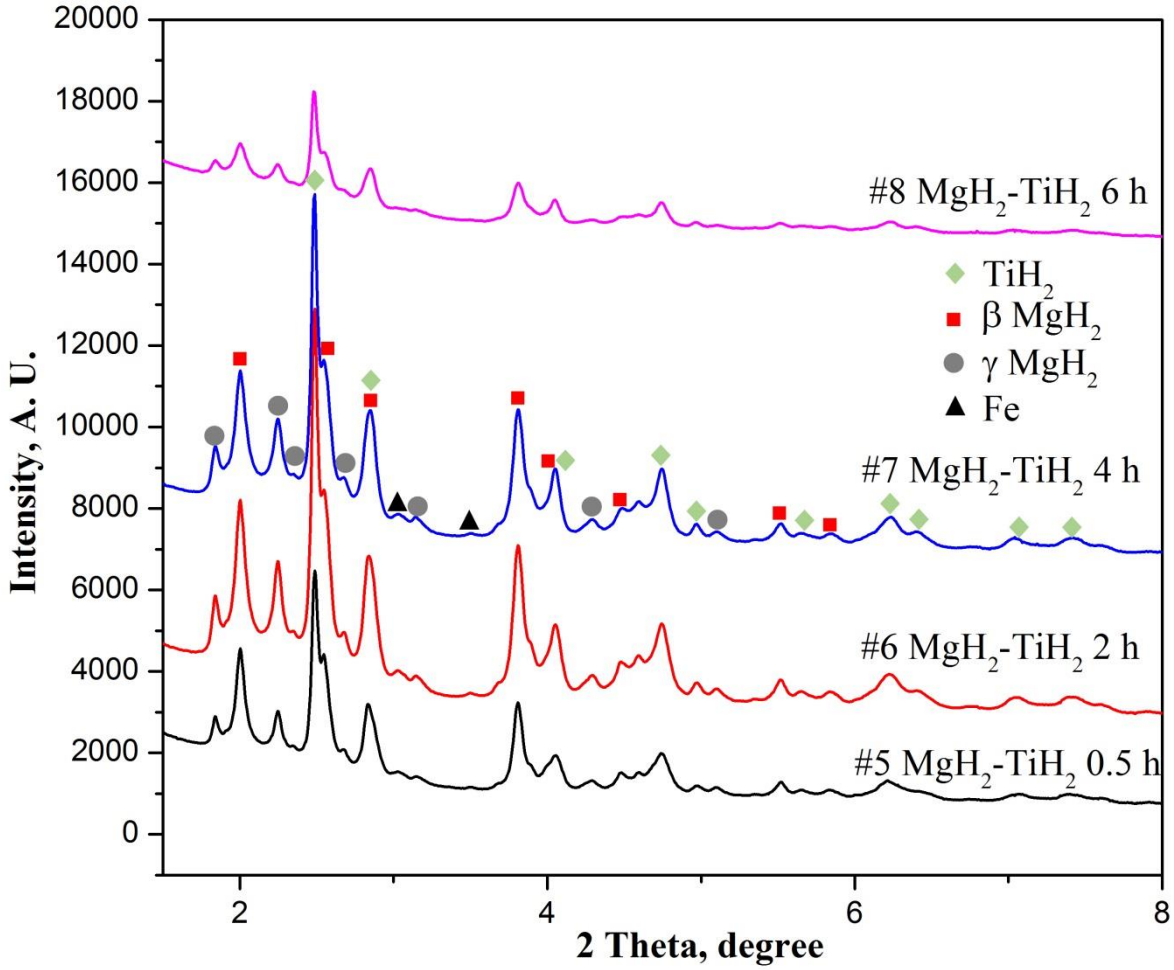

Figure 19. X-ray diffraction pattern of MgH_2-TiH_2 with different grain size, sample #5-8.

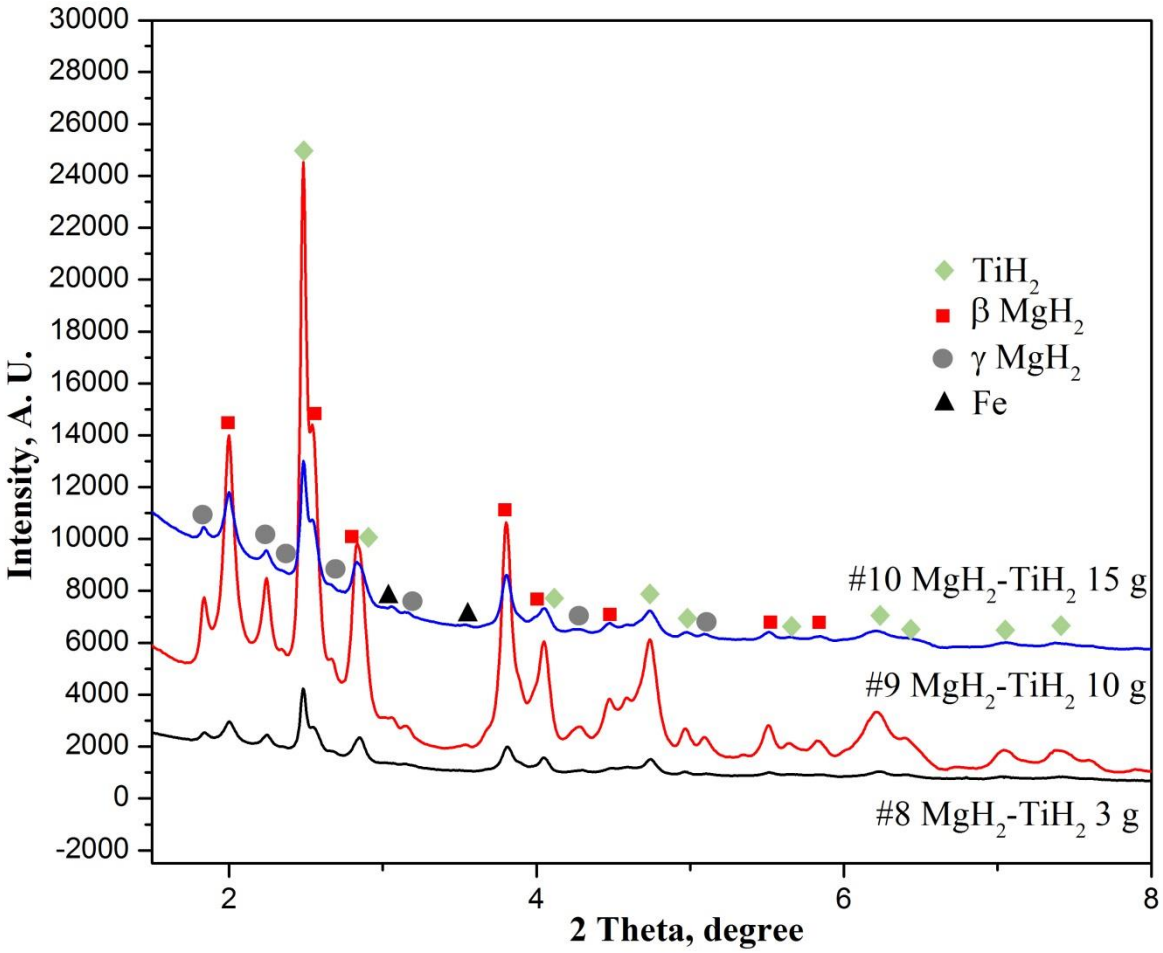

Figure 20. X-ray pattern of MgH_2-TiH_2 with different grain size, sample #8-10.

This indicates that changing the milling load will not have an obvious effect on the phase composition.

The X-ray diffraction pattern of magnesium hydrides with/without different catalysts was compared; see Figure 21. There is not much difference for the X-ray diffraction pattern after adding $TiMn_2$ and VTiCr catalyst. It could be: a) only 5 mol.% $TiMn_2$ and VTiCr were added and b) the three strongest diffraction peaks are not prominent compared to other diffraction peaks for $TiMn_2$ and VTiCr. However, in the X-ray diffraction pattern of MgH_2-TiH_2, there is a significant TiH_2 peak at 2.4 ºand 4.2 ºcompared to that of pure MgH_2.

6.3.4 Morphology

The microstructure of these three different samples, sample #8-10, has been examined via transmission electron microscopy (TEM); see Figure 22. The darker part in the images is TiH_2 additive while the brighter area is MgH_2. For sample #8, the TiH_2 additive was reduced to a size of ca. 2-3 nm and dispersed uniformly in magnesium hydride particle; Figure 22 (a). However, for sample #9, the size for the TiH_2 additive is much larger, ca. 60-100 nm and agglomerated together in the magnesium hydride particle; Figure 22 (b). Such agglomeration is even more serious for sample #10, with the 15 g milling load; Figure 22 (c). As shown in section 6.3.5.1, sample #8 has the best room temperature hydrogenation kinetics as well as the best cycle ability after 5 hydrogenation and dehydrogenation cycles, followed by sample #9, and then sample #10. This implies that the particle size as well as particle distribution of catalyst could possibly have an effect on the hydrogenation kinetics of magnesium hydrides. In addition, sample #8 has the smallest grain size, compared to sample #9 and #10, as discussed in section 6.3.1.

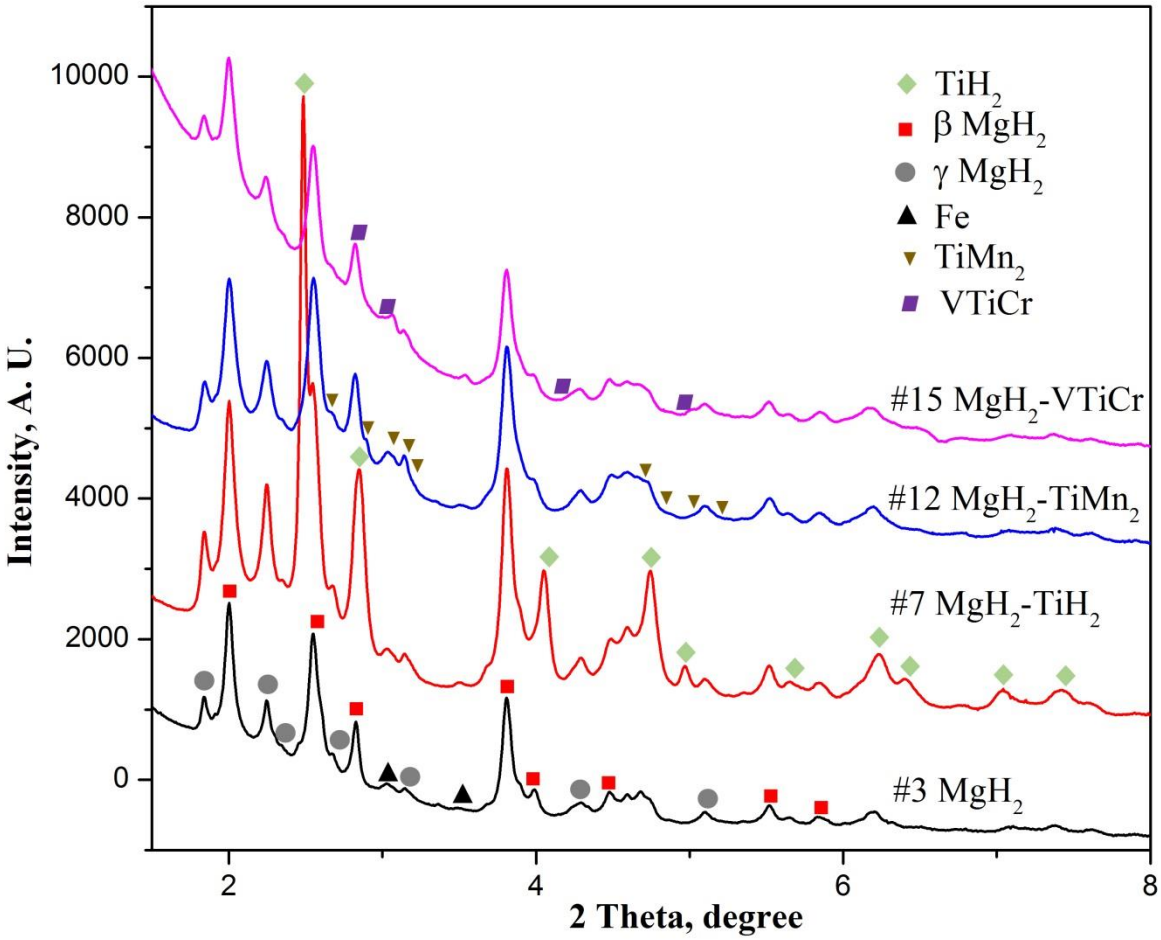

Figure 21. X-ray diffraction pattern of pure MgH_2, MgH_2-TiH_2, MgH_2-$TiMn_2$, and MgH_2-VTiCr.

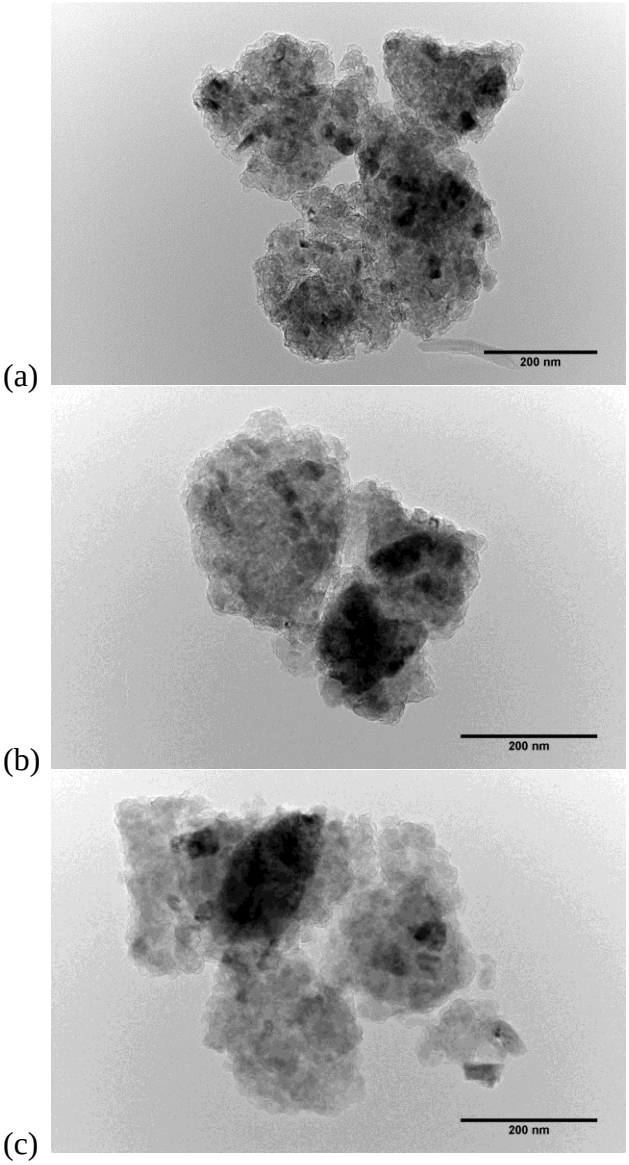

Figure 22. TEM images of MgH_2-TiH_2 with different grain size, a) sample #8; b) sample #9; and c) sample #10.

6.3.5 Hydrogenation Kinetics

6.3.5.1 Effect of grain size

Pure MgH_2 was milled for different lengths of time, 0.5, 2, 4, and 6 h, as sample #1-4, and the same for MgH_2-0.1TiH_2 as sample #5-8. Temperature deviations were within 1.5 ºC for each sample during hydrogenation at different temperatures, indicating the hydrogenation was maintained isothermal or at least quasi-isothermal.

See Figure 23 for the hydrogenation of pure magnesium hydrides, sample #1-4. When hydrogenated at either 150 or 200 ºC, sample #1 was slowest in absorbing hydrogen. As discussed in section 6.3.1, the grain size of these three samples are #1>#2>#3>#4. Moreover, sample #1-3 cannot uptake hydrogen in a test temperature lower than 150 ºC. In comparison, sample #4, which has the smallest grain size among samples #1-4, can absorb hydrogen as low as 60 ºC. This implies that magnesium hydrides with smaller grain size tend to have superior hydrogenation rate.

For MgH_2-TiH_2, sample #5-8, of which grain size follows an order of #5>#6>#7>#8, the relationship of grain size and hydrogenation rate was slightly different; see Figure 24. At room temperature, sample #8 had the best hydrogenation rate, followed by sample #7, then sample #6, while sample #5 cannot even uptake hydrogen at room temperature. As hydrogenation temperature increased (60 ºC or above), during the initial hydrogenation stage, the hydrogenation rate follows a sequence of #8>#7>#6>#5, the same as in room temperature hydrogenation. However, after the initial hydrogenation stage, sample #6 absorbed more hydrogen than sample #7 when hydrogenated at 60 ºC. Moreover, sample #5 absorbed more hydrogen than the other three samples (sample # 6, 7, and 8) at 150 ºC. To conclude, for MgH_2-TiH_2, sample with smaller grain size will have faster hydrogenation

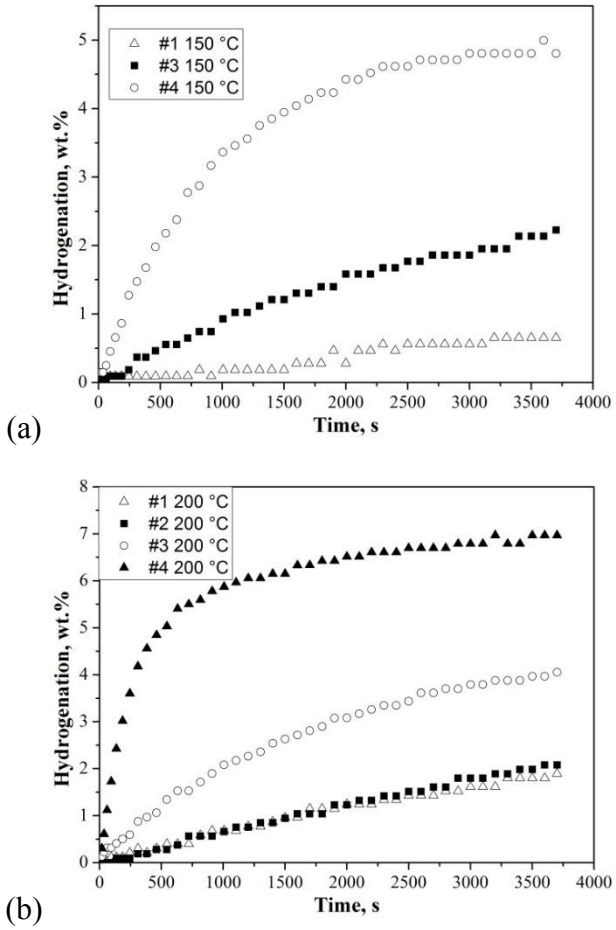

Figure 23. Hydrogenation of pure MgH_2 with different grain size, sample #1-4, at a) 150 ºC and b) 200 ºC.

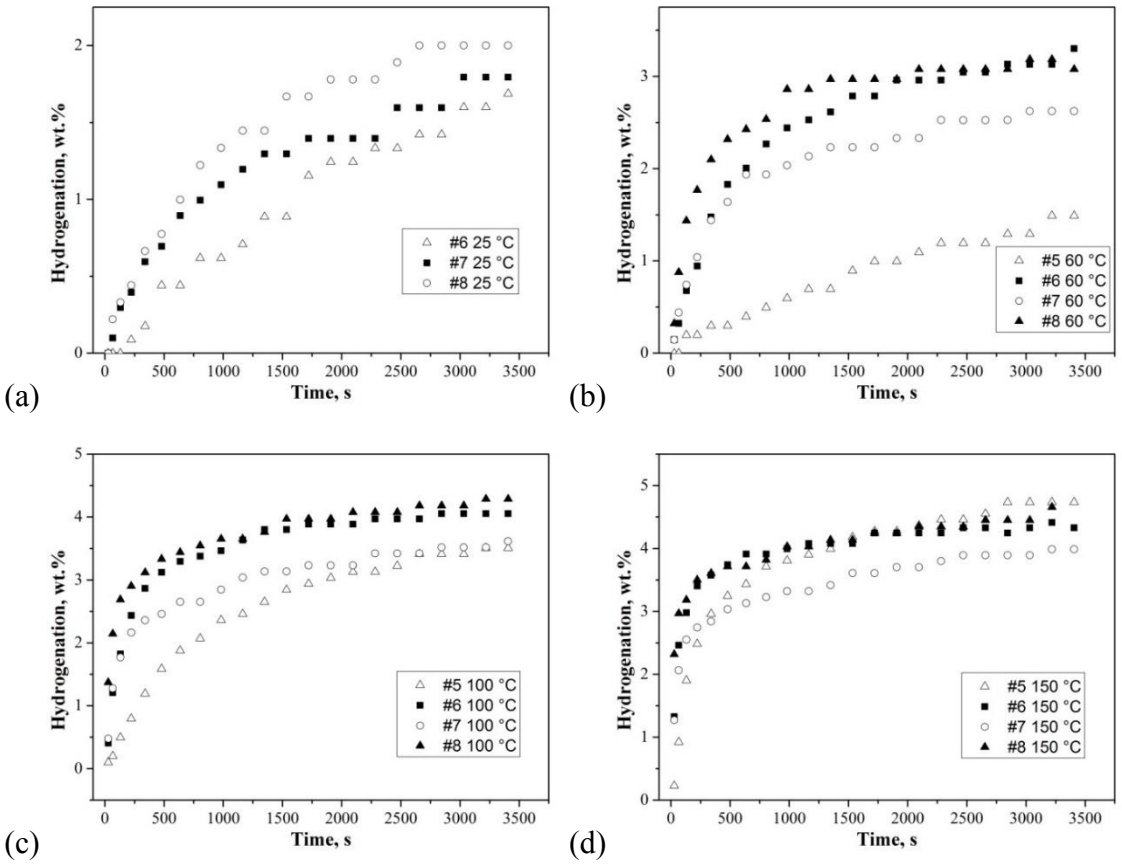

Figure 24. Hydrogenation of MgH_2-TiH_2 with different grain size, sample #5-8, at a) room temperature; b) 60 ºC; c) 100 ºC; and d) 150 ºC.

rate in low-temperature hydrogenation or in the initial stage of high-temperature hydrogenation, while in the later stage of high-temperature hydrogenation, it falls behind sample with larger grain size.

See Figure 25 for the comparison of hydrogenation kinetics at different temperatures of sample #8-10. The hydrogenation tests were conducted under various temperatures following a sequence of: room temperature, 60 ºC, 100 ºC, 150 ºC, 200 ºC, and then room temperature hydrogenation again. In addition, hydrogenation was maintained under isothermal or at least quasi-isothermal condition during all the hydrogenation tests.

For hydrogenation at lower temperature (room temperature and 60 ºC), sample #8 showed the best absorption rate, followed by sample #9, and then sample #10. As hydrogenation temperature increased (100, 150, and 200 ºC), sample #8 still held the fastest hydrogenation rate in the initial hydrogenation stage, as shown in Figure 25 (c)-(e). However, at the end of the 1 h hydrogenation, sample #8 cannot absorb as much hydrogen as sample #9 and #10.

The repeatability of good room temperature kinetics is also one of the main concerns in hydrogenation kinetics as low temperature absorption, especially room temperature absorption, allows for easier operation and less energy consumption. See Figure 25 (a) for the comparison of the 1^{st} and 6^{th} room temperature hydrogenation kinetics. After 5 hydrogenation/dehydrogenation cycles, sample #8 gained improved kinetic rate, and sample #9 maintained almost the same kinetic rate, while sample #10 suffered from an approximately 1/3 (0.5 wt.%) reduction in absorbed hydrogen at the end of the 1 h hydrogenation. In regard to the degradation of room temperature hydrogenation, sample with the smallest grain size works best in maintaining a good room temperature kinetic

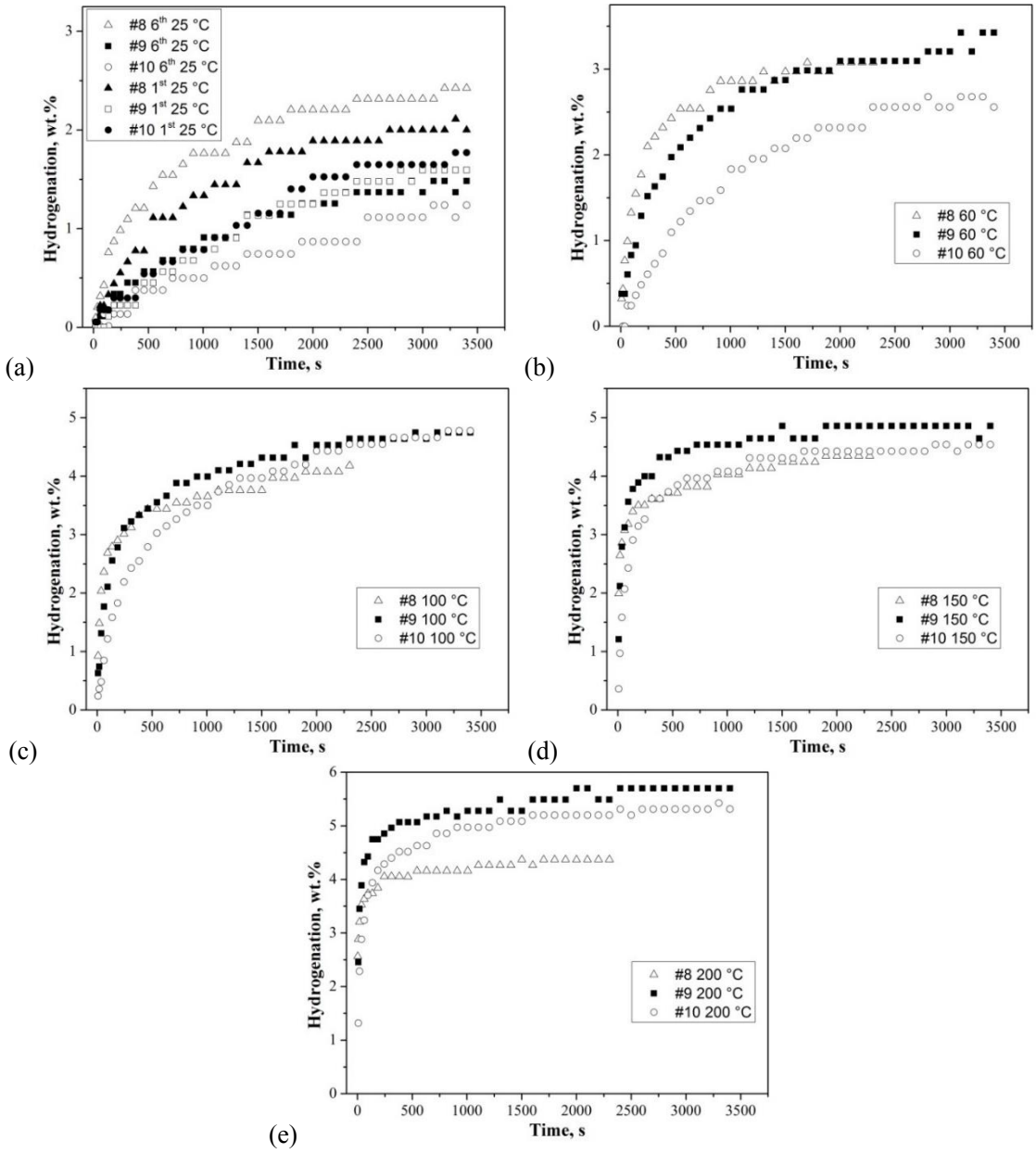

Figure 25. Hydrogenation of MgH_2-TiH_2 samples #8-10 at a) room temperature; b) 60 ºC; c) 100 ºC; d) 150 ºC; and e) 200 ºC.

rate. However, future characterization of cycle ability based on more cycles is necessary to further verify this result.

6.3.5.2 Effect of Catalyst

In this section, three different catalysts, 10 mol.% TiH_2, 5 mol.% $TiMn_2$, and 5 mol.% VTiCr, have been added to magnesium hydrides and milled for the same amount of time, 4 h, as sample #7, 12, and 15, respectively. Note that hydrogenation was maintained isothermal or at least quasi-isothermal.

Adding catalyst considerably improved the hydrogenation kinetics; see Figure 26. Before adding catalyst, pure MgH_2 milled for 4 h, sample #3, cannot uptake hydrogen unless temperature was raised to 150 ºC; Figure 26 (c). However, room temperature hydrogenation of magnesium hydrides was made possible via adding TiH_2, $TiMn_2$, or VTiCr as catalyst; Figure 26 (a). Even though the hydrogenation rate of pure MgH_2, sample #3, was largely improved via raising temperature from 150 to 200 ºC, MgH_2-TiH_2, sample #7, still absorbed ca. 1 wt.% more hydrogen than pure MgH_2, sample #3; Figure 26 (d).

In regard to the effect of these three catalysts, TiH_2, $TiMn_2$, and VTiCr, all of them were effective in improving the hydrogenation kinetics of MgH_2. At room temperature, the hydrogenation rate was almost the same for MgH_2 with different catalysts: in the end of the 1 h hydrogenation, MgH_2-$TiMn_2$ absorbed 1.86 wt.% hydrogen, MgH_2-TiH_2 1.80 wt.%, and MgH_2-VTiCr 1.6 wt.%. When hydrogenation occurred in 100 ºC, the hydrogenation rate for the three samples is still very close, and all of them are fast in the initial hydrogenation stage, but slightly varies in a sequence of $TiMn_2$>VTiCr>TiH_2. As temperature rose to 150 ºC, the hydrogenation rate still followed the trend of

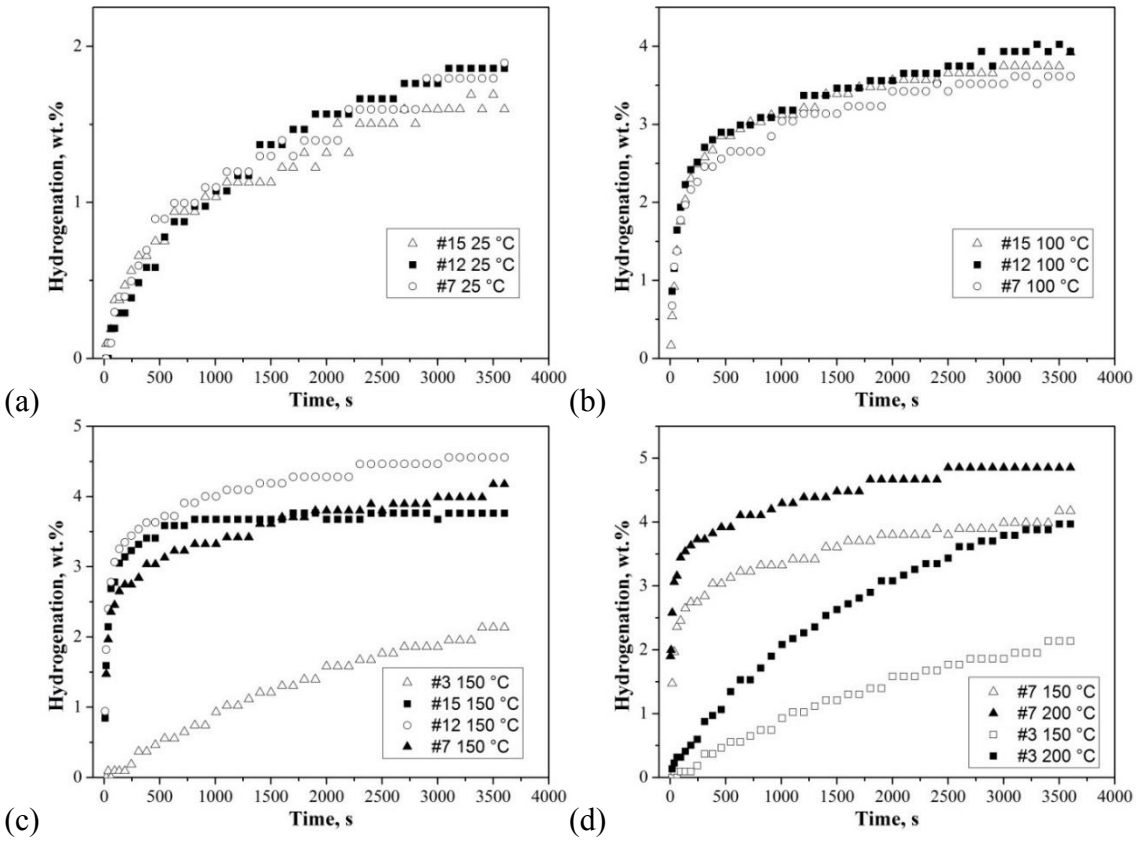

Figure 26. Comparison of hydrogenation kinetics of magnesium hydrides with three different catalysts at a) room temperature; b) 100 ºC; and c) 150 ºC as well as d) pure MgH_2 and MgH_2-TiH_2 at two different temperatures, 150 and 200 ºC.

$TiMn_2$>VTiCr>TiH_2 during the initial hydrogenation stage. However, in the later hydrogenation stage, the hydrogenation curve of MgH_2-VTiCr, sample #15, leveled off, while MgH_2-TiH_2, sample #7, as well as MgH_2-$TiMn_2$, sample #12, kept absorbing hydrogen with a relatively slow rate.

6.3.5.3 Effect of Temperature

Temperature is certainly an important factor in hydrogenation, as discussed in section 5.3.3. See Figure 27 for the temperature effects of pure MgH_2 (sample #3) and MgH_2-TiH_2 (sample #7). Note that both samples were milled for 4 h and all the hydrogenation tests were maintained isothermal or at least quasi-isothermal.

The pure magnesium cannot absorb hydrogen until temperature was raised to 150 ºC, at which sample picked up 2.1 wt.% hydrogen; see Figure 27 (a). As temperature further increased, sample absorbed 1.8 wt.% more hydrogen at 200 ºC, and even 4.8 wt.% more at 250 ºC. Represented by the slope of the curve, the rate of hydrogenation for pure MgH_2 appeared as a gradually decreasing variable, showing that the hydrogenation rate was gradually decreasing as hydrogenation proceeded. Moreover, if allowed for a longer time, sample will slowly absorb to the maximum value of hydrogen, i.e., the hydrogen capacity of the material.

However, for magnesium with TiH_2, the rate of hydrogenation was fast in the initial stage and then sharply turned to a much smaller value, especially for the high-temperature hydrogenation; see Figure 27 (b). By adding TiH_2, magnesium hydride can absorb hydrogen at room temperature, much lower than the 150 ºC of pure MgH_2. In the end of the 1 h hydrogenation, sample #7 absorbed 1.8, 2.6, 3.6, 4.0, and 4.8 wt.% hydrogen at 25,

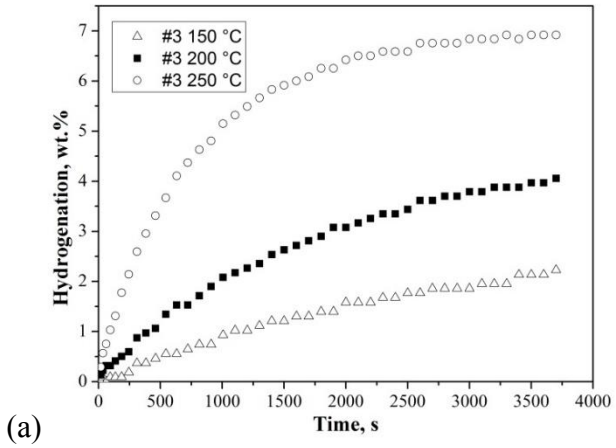

(a)

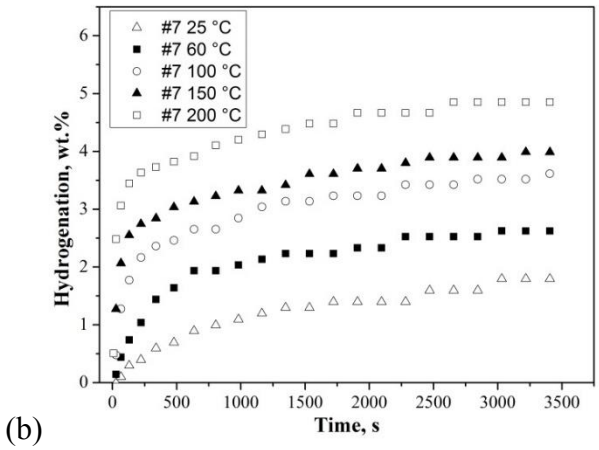

(b)

Figure 27. Comparison of hydrogenation kinetics at different temperatures of a) pure MgH_2 milled for 4 h, sample #3; b) MgH_2-TiH_2 additive milled for 4 h, sample #7.

60, 100, 150, and 200 ºC, respectively.

6.3.5.4 Effect of Pressure

In this section, sample #7, MgH_2-0.1TiH_2 milled for 4 h, was selected and tested under different hydrogen pressures, 0.5, 1, and 10 bar, in a temperature range from room temperature to 150 ºC; see Figure 28. At lower temperature (room temperature and 60 ºC), higher hydrogen pressure facilitated the hydrogenation process, while at higher temperature, especially 150 ºC, hydrogenation under 10 bar H_2 pressure still had the best hydrogenation rate in the initial hydrogenation stage. However, in the later hydrogenation stage, the 10-bar hydrogenation became very slow afterward and could not absorb as much hydrogen as in the other two lower-pressure hydrogenation tests; Figure 28 (d).

6.4 Discussion

6.4.1 Modeling

In order to find the most appropriate kinetic model to describe the hydrogenation kinetics of materials studied in this work, different models have been applied to interpret the hydrogenation kinetic data, including P1 power law, E1 exponential law, Johnson-Mehl-Avrami (JMA), B1 Prout-Tompkins, Jander diffusion model (JMD), 1-D diffusion model, 2-D diffusion model (Bidmensional particle shape), 3-D diffusion model (Ginsling-Braunshteinn model), 2-D contracting area model, 3-D contracting volume model, F1 first order, F2 second order, and F3 third order. See Table 5 for more details of each model. It should be noted that temperature during the hydrogenation process was kept near isothermal by adding graphite. And the pressure has been adjusted based on the normalized

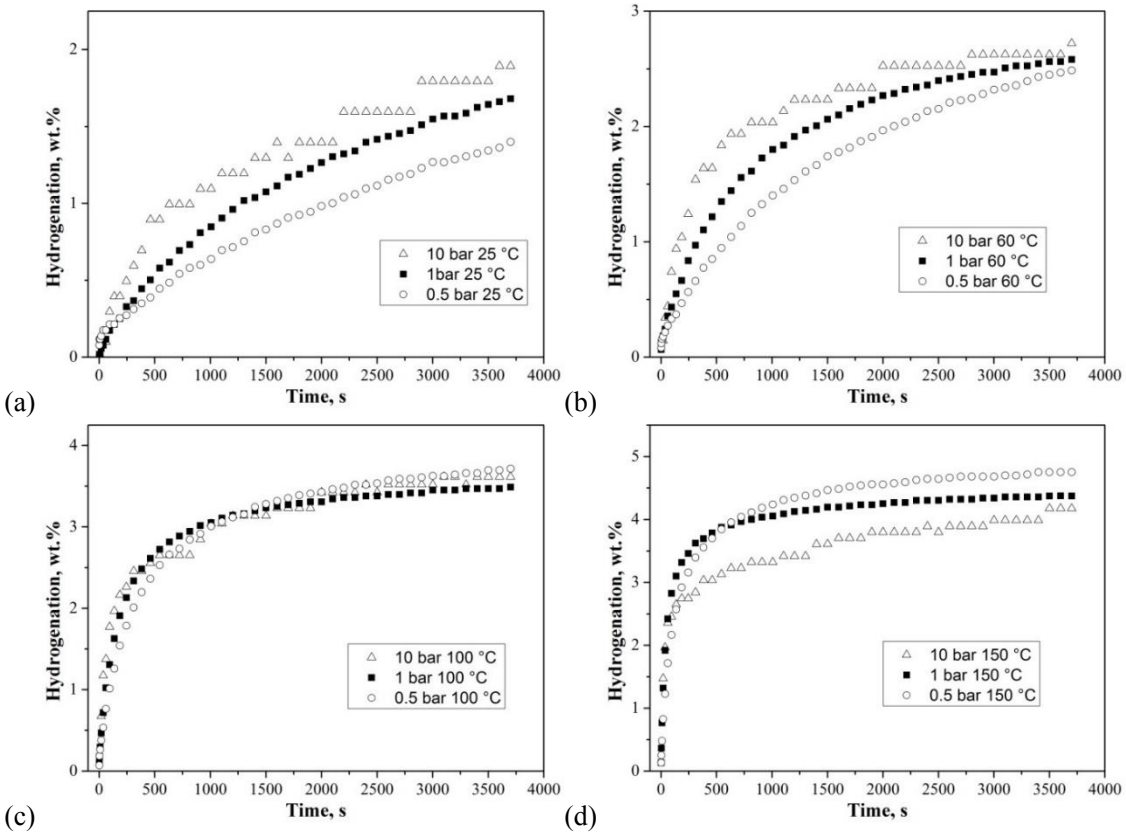

Figure 28. Hydrogenation kinetics of MgH_2-0.1TiH_2 4 h under different pressures at a) room temperature; b) 60 ºC; c) 100 ºC; and d) 150 ºC.

pressure dependence method (NPDM) put forward by Ron in 1999 [96], a method that introduced pressure dependence factor F(P)=|Peq-P|/P, which combines with the rate equation in a way as $f(\xi)=ktF(P)$, to offset the effect of pressure variation. See Table 15 for the modified equation after applying the NPDM method, where $f(\xi)$ stands for the left side of the rate equation, the right side of which is the product of rate constant k and reaction time t.

Among various models, the Johnson-Mehl-Avrami (JMA) model works best to describe the hydrogenation behavior at different temperatures. See Figure 29 (a) and (c) for the JMA model fitting of hydrogenation kinetics of pure MgH_2 and MgH_2-0.1TiH_2 milled for 4 h (sample #3 and 7), respectively. For both samples, the JMA plot appears as satisfactory linear lines for hydrogenation at each temperature. It should be noted that the P1 power law was found in good consistency with the hydrogenation kinetics. An example of the P1 power law fitting is presented in Appendix D. However, this model is merely a numerical one without any indication of inherent physical mechanism. Therefore, no further discussion will be presented in this work regarding the P1 power law.

Except for the JMA model, another model, the JMD model, could partially describe the hydrogenation kinetics of pure MgH_2 as well; see Figure 29 (b). For hydrogenation at 150 and 200 ºC, the JMD model can linearly fit the kinetics data, indicating that diffusion could be the possible mechanism during hydrogenation for this certain sample at hydrogenation temperature not higher than 200 ºC. However, when hydrogenation temperature was raised to 250 ºC, the JMD model fitting deviates from a linear line, implying that as temperature increases, diffusion might become less of a rate-limiting

Table 15. Summary of the rate equation after appling the NPDM method.

Rate laws	Original equation	Equation Applied NPDM
P1 power	$\xi^{1/n}=kt$	$F(P)^{-1}\xi^{1/n}=kt$
E1 exponential	$ln(\xi)=kt$	$F(P)^{-1}ln(\xi)=kt$
Johnson-Mehl-Avrami (JMA)	$ln(-ln(1-\xi))=ln(k)+nln(t)$	$ln(-ln(1-\xi))=ln(k)+nln(t/F(P))$
B1 Prout-Tompkins	$ln(\xi/(1-\xi))=kt$	$F(P)^{-1}ln(\xi/(1-\xi))=kt$
Jander diffusion model (JMD)	$(1-(1-\xi)^{1/3})^2=kt$	$F(P)^{-1}(1-(1-\xi)^{1/3})^2=kt$
1-D diffusion	$\xi^2=kt$	$F(P)^{-1}\xi^2=kt$
2-D diffusion (Bidmensional particle shape)	$(1-\xi)ln(1-\xi)+\xi=kt$	$F(P)^{-1}((1-\xi)ln(1-\xi)+\xi)=kt$
3-D diffusion (Ginsling-Braunshteinn model)	$(1-2\xi/3)-(1-\xi)^{2/3}=kt$	$F(P)^{-1}((1-2\xi/3)-(1-\xi)^{2/3})=kt$
2-D contracting area	$1-(1-\xi)^{1/2}=kt$	$F(P)^{-1}(1-(1-\xi)^{1/2})=kt$
3-D contracting volume	$1-(1-\xi)^{1/3}=kt$	$F(P)^{-1}(1-(1-\xi)^{1/3})=kt$
F1 first order	$-ln(1-\xi)=kt$	$-F(P)^{-1}ln(1-\xi)=kt$
F2 second order	$1/(1-\xi)=kt$	$F(P)^{-1}1/((1-\xi)=kt$
F3 third order	$(1/(1-\xi))^2=kt$	$F(P)^{-1}(1/(1-\xi))^2=kt$

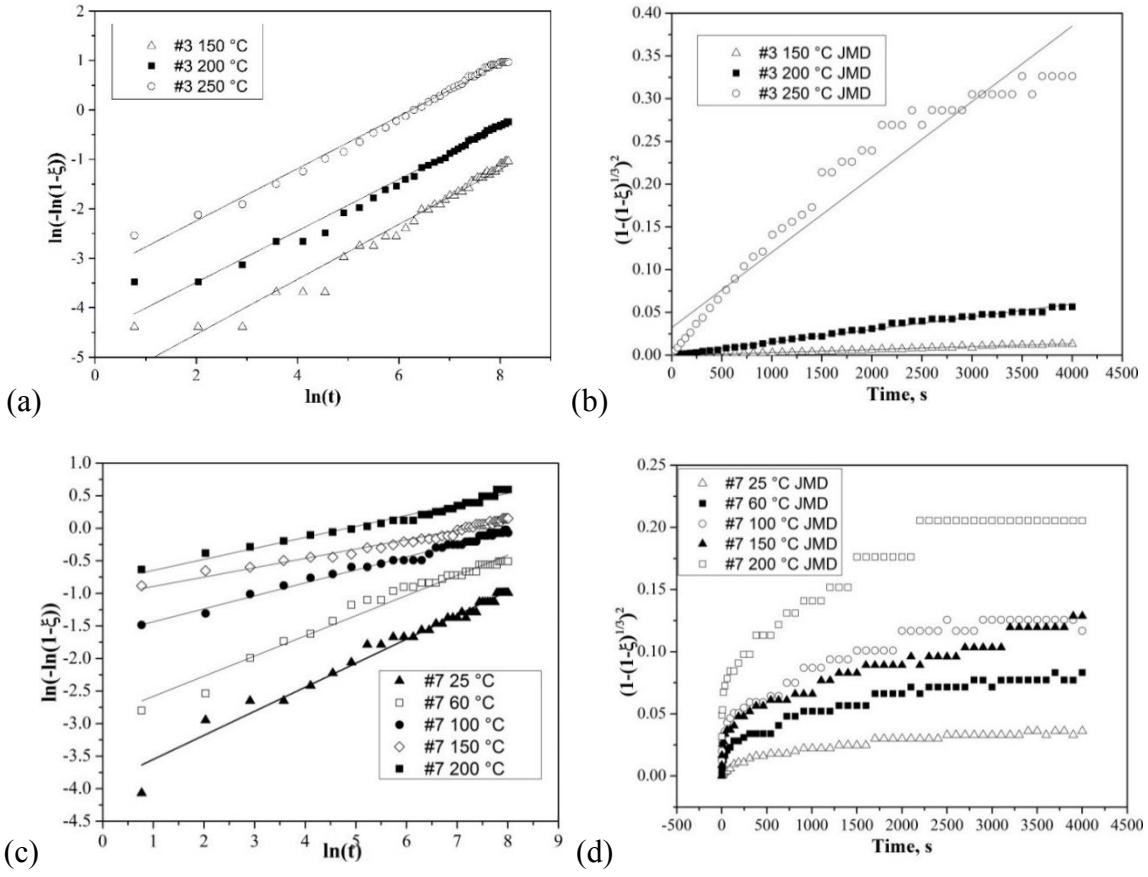

Figure 29. The hydrogenation of pure MgH_2 milled for 4 h fit by a) JMA model and b) JMD model, as well as the hydrogenation kinetics of MgH_2-0.1TiH_2 milled for 4 h fit by c) JMA model and d) JMD model.

factor during the hydrogenation process. See Figure 30 for JMD kinetics modeling of other pure MgH_2 samples milled for 0.5, 2, and 6 h, sample #1, 2, and 4. For sample #1, pure MgH_2 milled for 0.5 h, the JMD model has high consistency with the kinetic data of hydrogenation in a temperature range of 150-250 ºC. However, for sample #2, pure MgH_2 milled for 2 h, the JMD model works well in describing the hydrogenation kinetics at 200 and 250 ºC, but is not suitable for the hydrogenation at the higher temperature, 300 ºC. For sample #4, pure MgH_2 milled for 6 h, the same tendency appears where the JMD model could fit the kinetic data of hydrogenation at lower temperatures, 60 and 100 ºC, but failed for the hydrogenation at higher temperatures, 150 and 200 ºC. The consistency of the JMD model with the kinetic data of low-temperature hydrogenation of pure MgH_2 implies that at lower temperatures, hydrogenation of MgH_2 could possibly be controlled by diffusion, which will be discussed later in section 6.4.2 as well.

In comparison with pure MgH_2, MgH_2-TiH_2 cannot be fit by the JMD model anyway. See Figure 29 (d) for the JMD model fitting of the hydrogenation kinetics of MgH_2-0.1TiH_2 milled for 4 h, sample #7, where the model fitting is a concave curve for hydrogenation under different temperatures from room temperature to 200 ºC. In addition, none of the JMD model fitting for other MgH_2-TiH_2 samples, sample #5, 6, and 8, is linear, as shown in Appendix D. This implies that the JMD model is not suitable in describing the hydrogenation kinetics of such material.

Other modeling details are given in Appendix D.

Activation energy of hydrogenation was calculated using the Arrhenius Equation; see Eq. 6. By plotting *ln(k)*, obtained based on the JMA model, against the reverse of temperature, *1/T*, activation energy could be calculated by the slope of the fitted data.

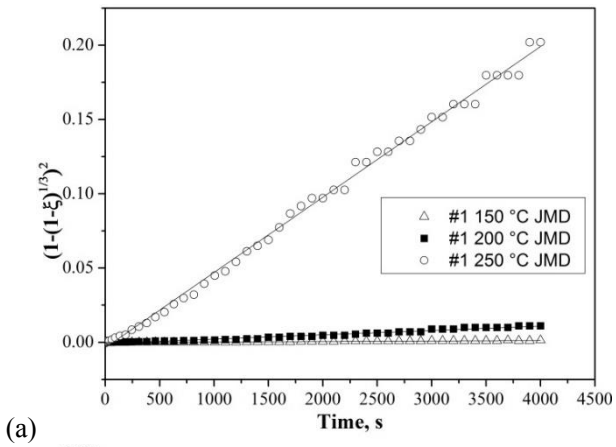

(a)

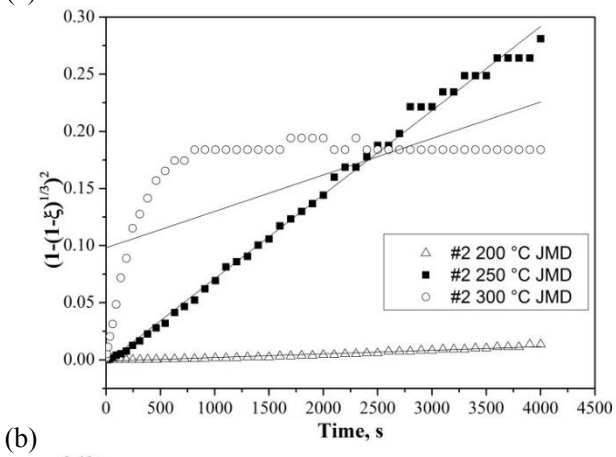

(b)

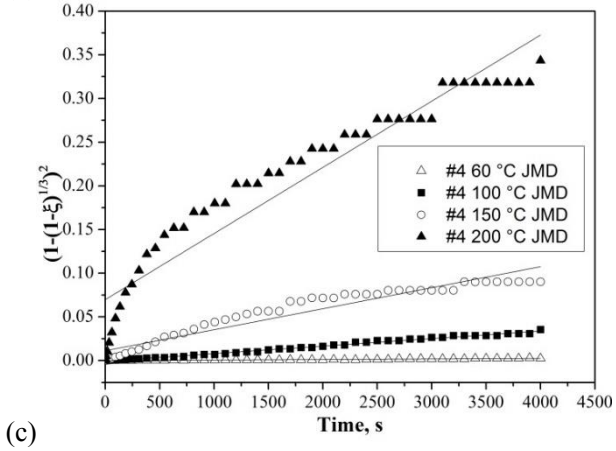

(c)

Figure 30. JMD model fitting of pure MgH_2 milled for a) 0.5 h; b) 2 h; and c) 6 h.

See Figure 31 for the Arrhenius plots of various samples, sample #1-10, 12, and 15. Exact values of the calculated activation energies are shown in Table 16-18.

See Figure 31 (b) and Figure 31 (c) for the Arrhenius plot of pure MgH_2 and MgH_2-TiH_2, respectively. For pure MgH_2 samples, sample #1-4, sample #1 has the sharpest slope in the Arrhenius plot, followed by sample #2, #3, and #4. Thus, sample #1 has the biggest activation energy, followed by sample #2, #3, and #4. As discussed in section 6.3.1, the grain size of sample #1-4 follows a trend of #1>#2>#3>#4. This implies that pure MgH_2 with a larger grain size has bigger activation energy of hydrogenation. For MgH_2-TiH_2, sample #5-8, the same trend shows that MgH_2-TiH_2 sample with a smaller grain size has smaller activation energy for hydrogenation. See Table 16 for the calculated activation energy of hydrogenation for pure MgH_2 and MgH_2-TiH_2.

See Figure 31 (a) for the Arrhenius plot of sample #8-10. The activation energy of hydrogenation for sample #10 is 33.3 kJ/mol H_2, which is 5.8 and 9.2 kJ/mol H_2 higher than those of samples #8 and 7, respectively. See Table 17 for the calculated activation energy of hydrogenation for sample #8-10. As discussed in section 6.3.1, grain size of these three samples are #8<#9<#10. This result again supports the conclusion that sample with smaller grain size will have smaller activation energy of hydrogenation.

In terms of the effect of catalyst on the activation energy, the activation energy of hydrogenation for MgH_2-TiH_2 (sample #7), MgH_2-$TiMn_2$ (sample #12) and MgH_2-VTiCr (sample #15) turns out to be very close, which is 24.2 (MgH_2-TiH_2), 22.6 (MgH_2-$TiMn_2$), and 24.7 (MgH_2-VTiCr) kJ/mol H_2; see Figure 31 (d) and Table 16. In addition, the activation energies of MgH_2 with catalyst are much smaller compared to that for the pure MgH_2 milled for the same amount of time (sample #3, pure MgH_2 milled for 4 h), indicating

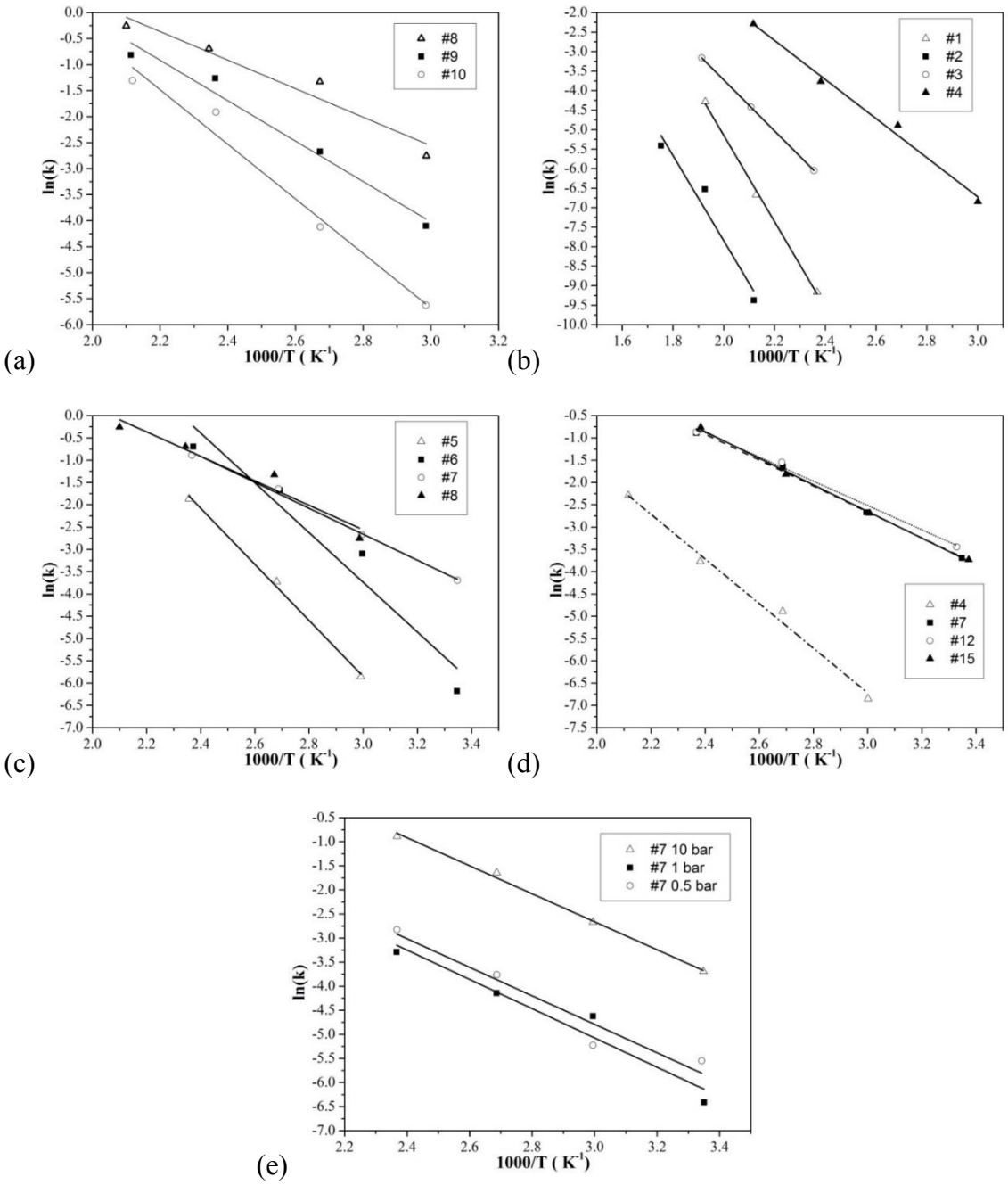

Figure 31. The calculation of activation energy of hydrogenation of MgH_2 prepared with different a) milling load (with TiH_2); b) milling time; c) milling time (with TiH_2); d) catalyst (TiH_2, VTiCr and $TiMn_2$); and e) different hydrogenation pressure (with TiH_2).

Table 16. Calculated activation energy of magnesium hydrides with different processing variables and catalysts.

Milling time	Activation energy (kJ/mol H_2)			
	Pure MgH_2	MgH_2-0.1TiH_2	VTiCr	$TiMn_2$
0.5	92.0	52.3		
2	90.8	46.4		
4	54.3	24.2	24.7	22.6
6	41.6	22.8		

Table 17. Calculated activation energy of samples milled with different milling load.

Sample No.	Milling load (g)	Activation energy (kJ/mol H_2)
8	3	24.2
9	10	27.6
10	15	33.3

Table 18. Calculated activation energy under three different pressures, magnesium hydride with TiH_2 additive milled for 4 h.

Sample No.	Pressure (bar)	Activation energy (kJ/mol H_2)
	10	24.2
7	1	25.3
	0.5	24.6

that adding catalyst helps to reduce the activation energy of hydrogenation for magnesium hydride.

Activation energy of hydrogenation was also calculated based on hydrogenation tests under three different pressures (10, 1, and 0.5 bar). As discussed above in section 6.3.5.4, pressure will have an effect on the hydrogenation rate of MgH_2-0.1TiH_2. However, the activation energy of hydrogenation stays the same based on the kinetics data obtained under three different hydrogenation pressures; see Figure 31 (e) and Table 18. This implies that hydrogenation pressure, at least in the range of 0.5-10 bar, will not change the activation energy of magnesium hydride.

6.4.2 The Possible Mechanism

The activation energies for hydrogen diffusion in magnesium and magnesium hydride have been reported to be 40 kJ/mol H_2 and 98-166 kJ/mol H_2, respectively [61, 121]. As listed in Table 16, all the values of the calculated activation energy of hydrogenation are above 40 kJ/mol H_2 for sample #1-4 (pure MgH_2 milled for 0.5, 2, 4, and 6 h), which is 92.0, 90.8, 54.3, and 41.6 kJ/mol H_2, respectively. This indicates that diffusion could possibly be the rate-limiting step during hydrogenation for sample #1-4. Additionally, as discussed in section 6.4.1, the low-temperature hydrogenation kinetic data of sample #1-4 is in high consistency with the JMD model, Figure 30, which indicates that the hydrogenation of pure MgH_2 at lower temperature could possibly be controlled by diffusion.

However, different from that for pure MgH_2, the hydrogenation is not limited by diffusion for sample #5 and #6 (MgH_2-0.1TiH_2 milled for 0.5 and 2 h). Even though the activation energies for sample #5 and #6 are above the reported activation energy for

diffusion, the hydrogenation kinetic data of these two samples cannot be fit by any model based on the diffusion mechanism, such as the JMD, 1-, 2-, and 3-D diffusion models. Moreover, sample #1 and #5 as well as sample #2 and #6 were compared, of which two samples were milled for the same amount of time. It is found that for pure MgH_2, the mechanism of hydrogenation could be diffusion as discussed above, while after adding 10 mol.% TiH_2 as catalyst, diffusion is no longer the rate-limiting step. In other words, TiH_2 catalyst might assist in the diffusion process during hydrogenation. Similar conclusion could be obtained for two other catalysts, $TiMn_2$ and VTiCr. As Corey et al. have reported, adding additive Nb_2O_5, another good catalyst for MgH_2, allows for a higher H diffusion rate for MgH_2 [121].

In addition, when combining the calculated results of activation energy and grain size, Figure 32, a relationship could be found that the bigger the grain size is, the bigger the activation energy is. Yao et al. investigated the grain size effect on hydrogenation kinetics of MgH_2, based on the assumption that hydrogenation of MgH_2 was controlled by diffusion [104]. Yao contended that smaller grain size allows for a faster hydrogen diffusion rate, and MgH_2 of smaller grain size can uptake more hydrogen at lower temperature than that of larger grain size at higher temperature. In this work, if diffusion is the control step in the initial hydrogenation, the results of calculated grain size and modeling could be connected in a reasonable way.

First, assume diffusion is the control step for the initial stage of hydrogenation. For pure MgH_2, (sample #1-4), as milling time increases, the grain size of MgH_2 reduces gradually, allowing for better rate of hydrogen diffusion, thus, better hydrogenation kinetics and smaller activation energy. For one certain sample, as temperature increases, the rate of

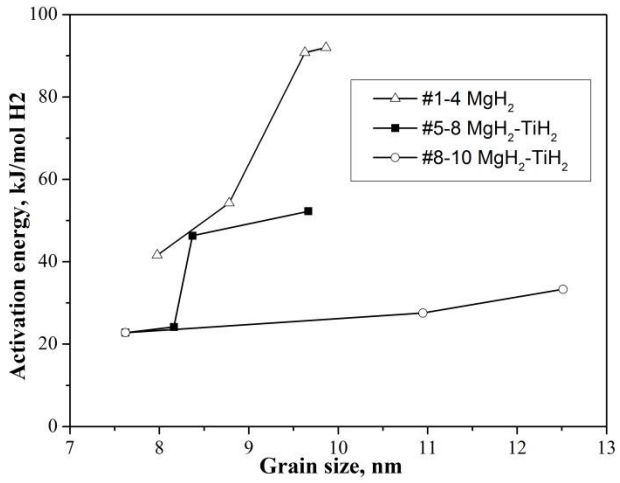

Figure 32. Relationship of grain size and calculated activation energy of hydrogenation.

diffusion will increase exponentially [121]. For MgH_2 of certain grain size, when temperature reaches a certain value, diffusion is rapid enough and becomes less of or no longer the control step, which could explain the discrepancy of JMD model fitting of low-temperature and high-temperature hydrogenation of pure MgH_2.

For MgH_2-TiH_2, on one hand, adding TiH_2 helps to reduce the grain size of MgH_2, allowing for fast hydrogenation kinetics. On the other hand, TiH_2 assists in the diffusion process as well, despite its effect on grain size. With two ways of improving the diffusion process, TiH_2 facilitates the diffusion rate of H_2 considerably and diffusion becomes less of or no longer the control step of hydrogenation, reducing the activation energy of MgH_2 hydrogenation considerably. $TiMn_2$ and VTiCr also have similar effect on the hydrogenation kinetics of MgH_2.

Admittedly, there could be other possible factors affecting the hydrogenation of MgH_2. Even though it follows certain trends regarding milling parameters and catalyst, the discrepancies of grain size of each sample are at most a couple of nanometers; see Table 13. The results of specific surface area, Figure 17, are not in consistency with the hydrogenation behavior, as discussed in section 6.3.5. Defects could be another possible factor that helps with the diffusion during hydrogenation, that the increasing milling time will raise the density of defects, creating a different path for diffusion other than grain boundaries. However, when the residual strain was examined, there is no obvious trend regarding milling parameters or adding catalyst, of which more details are given in the Appendix C. So far, grain size is the only factor that correlates with the hydrogenation behavior, while other factors such as defects, however, cannot be ruled out definitely.

6.4.3 The Influence of Fe Contamination

According to the literature [47, 71, 75, 122], iron and related compounds have been studied previously as catalyst. Even though not as good as other catalyst, such as V, Ti, 8 at.% Fe is able to improve the dehydrogenation considerably, reported by Liang et al. [71] According to Bassetti et al., as low as 2 wt.% Fe could lead to ca. 5 wt.% more hydrogen release during dehydrogenation at 300 ºC [47]. As detected in X-ray diffraction patterns Figure 18 – Figure 21, there is certain amount of iron in the as-milled powder. It is understandable because the milling canister and milling balls were made from 316 Stainless Steel. It is highly possible that the collision and friction during milling would scrape down some stainless steel scratches, introducing certain iron content. Huot et al. detected 0.13 wt.% iron in their ball-milled magnesium hydride, but they believed such a small amount of contamination would not affect the kinetics of magnesium hydrides [48].

The validation of the results and discuss above should be questioned if iron had a significant effect on the hydrogenation kinetics in this work. In order to clarify this issue, first, iron content level in selected samples was measured; then, the hydrogenation kinetics were compared to determine how important a role, if any, did iron serve in this case.

Inductively Coupled Plasma Mass Spectrometer (ICP-MS) was employed to examine the iron content in the ball-milled powders. The processing variables that could possibly affect the level of iron content were milling load, milling time, and catalyst. To verify the effect of iron content on the hydrogenation kinetics in this work, six samples with different milling load, milling time, and catalyst were chosen, of which the iron content was listed in Table 19.

Table 19. Iron content of selected samples.

Sample No.	Sample condition	Iron content (ppm)
2	Pure MgH_2 2 h	5622
4	Pure MgH_2 6 h	22260
6	MgH_2-0.1 TiH_2 2 h	5028
8	MgH_2-0.1 TiH_2 6 h	19403
9	MgH_2-0.1TiH_2 6 h 10 g	2367
10	MgH_2-0.1TiH_2 6 h 15 g	1440

Smaller milling load leads to bigger iron content. When milling load was increased from 3 g to 15 g (#8-10), the iron content was reduced by a factor of 13. Moreover, longer milling time would introduce more iron content as well. After comparing sample #2&4 and sample #6&8, it is obvious that an increase of milling time from 2 h to 6 h will lead to a ca. 4-times augment in iron content. However, adding TiH_2 did not have an apparent influence on the iron content, concluded by comparing sample #2&6 and #4&8.

Combining the conclusion above and the discussion in section 6.3, it is clear that a smaller milling load and longer milling time are responsible for the higher iron content, two factors which could cause smaller grain size, thus faster hydrogenation rate as well, as we discussed in section 6.3.5. In order to clarify the question of whether iron is assisting the hydrogenation process, the hydrogenation kinetics of sample #6&9 was further compared; see Figure 33. Sample #6 and #9 have the same chemical composition, and the iron content of sample #9 is half of that of sample #6. If iron content was playing a significant role in hydrogenation, then sample #6 should have better hydrogenation kinetics. However, the results showed the opposite. As in Figure 33, sample #9 could pick up hydrogen faster, especially at higher temperatures. This indicates that iron content is not a primary factor affecting the hydrogenation kinetics of MgH_2 in this work.

6.5 Summary

The hydrogenation kinetics of magnesium hydrides was studied under isothermal conditions where the self-heating effect was minimized. The key results are summarized as follows:

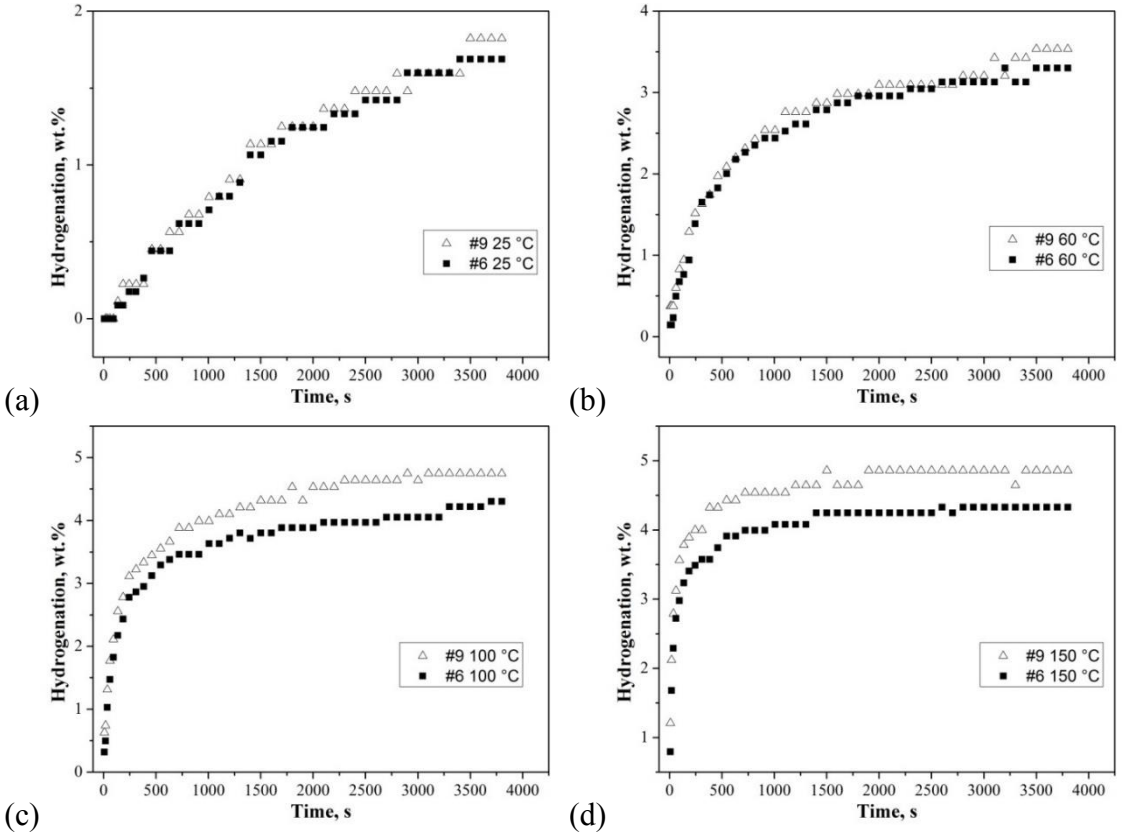

Figure 33. Comparison of hydrogenation kinetics of sample #6 and #9 at a) room temperature; b) 60 ºC; c) 100 ºC; and d) 150 ºC.

1. Longer milling time, smaller milling load, and adding appropriate catalyst helps reduce the grain size of magnesium hydride, thus facilitating hydrogenation of magnesium hydrides, and reducing the activation energy of hydrogenation as well;
2. Higher hydrogenation pressure favors faster hydrogenation, but will not affect the activation energy of hydrogenation;
3. The hydrogenation kinetics of MgH_2 with/without catalyst can be numerically described by the JMA model;
4. The JMD model has high consistency with kinetic data of low-temperature hydrogenation of pure magnesium hydrides;
5. Diffusion could be the control step for low-temperature hydrogenation of magnesium hydride with relatively large grain size. However, as temperature increases or adding appropriate catalysts, diffusion could be overcome and no longer the control step for hydrogenation of magnesium hydrides.

APPENDIX A

ENERGY DENSITY CALCULATION

The energy density of common thermal storage materials was calculated in this work, as shown in Figure 2. For metal hydrides, the gravimetric energy density was calculated as shown in Eq. 12, where D_m is the gravimetric energy density, n_{H_2} is the mole number of hydrogen, m and ΔH are the mass and formation enthalpy of metal hydrides, respectively. n_{H_2} could be expressed via the participation of hydrogenation capacity, w_{H_2}, as shown in Eq. 13, where M_{H_2} is the molar mass. Then the gravimetric energy density could be described as Eq. 14. Likewise, the volumetric energy density D_v is defined as in Eq. 15, where V is the volume of metal hydrides. The volume of the single metal hydride system consists of the volume of metal hydride and hydrogen gas, Eq. 16, where the volume of metal hydrides is negligible when compared to the volume of hydrogen gas, V_{H_2}, which could be calculated via Eq. 17 [123].

The energy density calculation of paired metal hydrides, which consist of one high-temperature (HT) hydride and one low-temperature (LT) hydride, is slightly different. Assume the m_1 and m_2 is the mass of HT hydride and LT hydride, $w_{H_2,1}$ and $w_{H_2,2}$ are the hydrogen capacity of HT hydride and LT hydride, respectively. The amount of hydrogen absorbed/desorbed by HT hydride and LT hydride should be the same, Eq. 18. As a result,

m_2 could be expressed by Eq. 19 and the mole number of hydrogen gas can be described as in Eq. 20. As for a closed system, the hydrogen circulating between HT hydride and LT hydride is restricted in the system, which is small compared to the volume of metal hydrides. Therefore, here the authors treat the volume of the system as the sum of both hydrides. See Eq. 21 and Eq. 22 for the gravimetric and volumetric energy density of the paired metal hydrides system. For the calculation of volumetric energy density, the volume expressed in the form of mass and density is shown in Eq. 23.

See Table 20 for details in the calculation. Note that for metal hydrides, the density, formation enthalpy, and H capacity was obtained from literature [12, 124]; for other thermal storage materials, such as phase change materials and latent heat storage materials, the gravimetric energy density was directly taken from the literature [125, 126] and the volumetric energy density was further converted using Eq. 24 (no gas component involved).

$$D_m = \frac{n_{H_2} \cdot \Delta H}{m} \quad \text{Eq. 12}$$

$$n_{H_2} = \frac{m \cdot w_{H_2}}{M_{H_2}} \quad \text{Eq. 13}$$

$$D_m = \frac{w_{H_2} \cdot \Delta H}{M_{H_2}} \quad \text{Eq. 14}$$

$$D_V = \frac{n_{H_2} \cdot \Delta H}{V} \quad \text{Eq. 15}$$

$$V = V_{H_2} + V_{MH} \approx V_{H_2} \quad \text{Eq. 16}$$

$$V_{H_2} = n_{H_2} V_m \quad \text{Eq. 17}$$

$$m_1 w_{H_2,1} = m_2 w_{H_2,2} \quad \text{Eq. 18}$$

$$m_2 = \frac{m_1 w_{H_2,1}}{w_{H_2,2}} \quad \text{Eq. 19}$$

$$n_{H_2} = \frac{m_1 w_{H_2,1}}{M_{H_2}} \quad \text{Eq. 20}$$

$$D_m = \frac{\frac{m_1 w_{H_2,1}}{M_{H_2}} (\Delta H_1 - \Delta H_2)}{m_1 + m_2} \quad \text{Eq. 21}$$

$$D_V = \frac{\frac{m_1 w_{H_2,1}}{M_{H_2}} (\Delta H_1 - \Delta H_2)}{V_1 + V_2} \quad \text{Eq. 22}$$

$$D_V = \frac{\frac{m_1 w_{H_2,1}}{M_{H_2}} (\Delta H_1 - \Delta H_2)}{\frac{m_1}{\rho_1} + \frac{m_2}{\rho_2}} \quad \text{Eq. 23}$$

$$D_V = D_m \cdot \rho \quad \text{Eq. 24}$$

Table 20 Energy density calculation.

Metal Hydrides	H_2 Capacity	Enthalpy	Density	Gravimetric Energy Density		Volumetric Energy Density	
	wt.%	kJ/mol H_2	g/cm^3	MJ/kg	kWh/kg	MJ/m^3	kWh/m^3
Metal Hyrides							
TiNi	1.4	59	6.6	0.413	0.115	2.634	0.732
Mg_2Ni	3.2	61	2.981	0.976	0.271	2.723	0.756
Mg_2Co	4.2	108	2.981	2.268	0.630	4.821	1.339
$Mg_2Ni_{.75}Fe_{.25}$	3.3	65.2	2.981	1.076	0.299	2.911	0.809
MgH_2	7.7	75.2	1.45	2.895	0.804	3.357	0.933
TiH_2	4	131	3.75	2.620	0.728	5.848	1.625
$LaNi_5$	1.5	30.8	8.3	0.231	0.064	1.375	0.382
$LaNi_2Cu_3$	0.9	32	8.3	0.144	0.040	1.429	0.397
$CaNi_5$	0.3	62	6.6	0.093	0.026	2.768	0.769
$MmNi_5$	1.4	23.5	8.6	0.165	0.046	1.049	0.291
$TiMn_{1.5}$	1.9	28.7	6.4	0.273	0.076	1.281	0.356
$TiCr_{1.8}$	2.43	20.2	6	0.245	0.068	0.902	0.250
$ZrFe_{1.5}Cr_{.5}$	1.4	24.3	7.6	0.170	0.047	1.085	0.301
$ZrMn_2$	1.7	37.4	7.4	0.318	0.088	1.670	0.464
TiFe	1.9	28.1	6.5	0.267	0.074	1.254	0.348
LiH_2	25.1	22.78	0.78	2.859	0.794	1.017	0.282
$NaBH_4$	10.7	90	1.074	4.815	1.338	4.018	1.116
$LiBH_4$	18.5	69	0.666	6.383	1.773	3.080	0.856

Table 20 Continued.

Metal Hydrides	H_2 Capacity	Enthalpy	Density	Gravimetric Energy Density		Volumetric Energy Density	
	wt.%	kJ/mol H_2	g/cm^3	MJ/kg	kWh/kg	MJ/m^3	kWh/m^3
Metal Hyrides							
$NaAlH_4$	7.5	37.6	1.24	1.410	0.392	1.679	0.466
$LiAlH_4$	10.6	18.9	0.917	1.002	0.278	0.844	0.234
$Li_3Be_2H_5$	8.1	40	0.71	1.620	0.450	1.786	0.496
Paired Metal Hydrides							
MgH_2+$TiMn_{1.5}$	See above			0.354	0.098	1353.3	375.9
TiH_2+$TiMn_{1.5}$				0.659	0.183	3435.1	954.2
TiH_2+$TiCr_{1.8}$				0.837	0.233	4096.0	1137.8
MgH_2+$LaNi_5$				0.279	0.077	1306.8	363.0
Mg_2Ni+$LaNi_5$				0.154	0.043	815.5	226.5
TiH_2+$LaNi_5$				0.547	0.152	3408.4	946.8
MgH_2+$TiCr_{1.8}$				0.508	0.141	1738.8	483.0
Mg_2Ni+$TiMn_{1.5}$				0.193	0.053	863.3	239.8

Table 20 Continued.

Metal Hydrides	H_2 Capacity	Enthalpy	Density	Gravimetric Energy Density		Volumetric Energy Density	
	wt.%	kJ/mol H_2	g/cm^3	MJ/kg	kWh/kg	MJ/m^3	kWh/m^3
Phase Change Material							
$NaNO_3$	2.257	N/A	N/A	0.199	0.055	450.0	125.0
KNO_3	2.11	N/A	N/A	0.266	0.074	561.6	156.0
KOH	2.044	N/A	N/A	0.150	0.042	306.0	85.0
Salt-ceramics($NaCO_3$ -$BaCo_3$/MgO)	2.6	N/A	N/A	0.415	0.115	1080.0	300.0
Na_2CO_3	2.533	N/A	N/A	0.276	0.077	698.4	194.0
Solid Latent Heat Storage Materials							
Sand-rock-mineral-oil	1.7	N/A	N/A	0.127	0.035	216.0	60.0
Reinforced concrete	2.2	N/A	N/A	0.164	0.045	360.0	100.0
Cast Iron	7.2	N/A	N/A	0.080	0.022	576.0	160.0
Silica fire bricks	1.82	N/A	N/A	0.297	0.082	540.0	150.0
Magnesia fire bricks	3	N/A	N/A	0.360	0.100	1080.0	300.0

Table 20 Continued.

Metal Hydrides	H_2 Capacity	Enthalpy	Density	Gravimetric Energy Density		Volumetric Energy Density	
	wt.%	kJ/mol H_2	g/cm^3	MJ/kg	kWh/kg	MJ/m^3	kWh/m^3
Liquid Latent Heat Storage Materials							
Mineral oil	0.77	N/A	N/A	0.257	0.071	198.0	55.0
Synthetic oil	0.9	N/A	N/A	0.228	0.063	205.2	57.0
Silicone oil	0.9	N/A	N/A	0.208	0.058	187.2	52.0
Nitrate salts	1.87	N/A	N/A	0.481	0.134	900.0	250.0
Carbonate Salts	2.1	N/A	N/A	0.737	0.205	1548.0	430.0
Liquid sodium	0.85	N/A	N/A	0.339	0.094	288.0	80.0

APPENDIX B

ESTIMATION OF PEAK TEMPERATURE RISE

The following calculation is based on the temperature change and hydrogen uptake observed in the nonisothermal hydrogenation test of MgH_2-0.1TiH_2, i.e., the test without expandable graphite.

Heat produced during hydrogenation, *Q*, is given by:

$$Q = \frac{m_{MgH_2} X_{H_2}}{M_{H_2}} \Delta H \qquad \text{Eq. 25}$$

where m_{MgH_2} stands for the mass of MgH_2 loaded in the sample vial, X_{H_2} for the weight percent of hydrogen, M_{H_2} for the mole mass of hydrogen, ΔH for the reaction enthalpy.

Assuming the sample is well insulated, and all the heat will thus be used to heat the sample,

$$Q = mC_p \Delta T \qquad \text{Eq. 26}$$

where *m* stands for sample mass, C_p for heat capacity, ΔT for temperature change.

Before hydrogenation, the sample was in the form of Mg, then gradually transformed from Mg to MgH_2. Due to the short reaction time (9.3 s), the mass and heat capacity were treated as constant and equal to those of the initial status (m_0 and C_{p_0}). Then Eq. 26 becomes:

$$Q = m_0 C_{p_0} \Delta T \quad \text{Eq. 27}$$

Combine Eq. 25 and Eq. 27,

$$\Delta T = \frac{X_{H_2} \Delta H}{M_{H_2}} \frac{m_{MgH_2}}{m_0} \frac{1}{C_{P_0}} \quad \text{Eq. 28}$$

where,

$$m_0 = m_{Mg} + m_{Graphite} \quad \text{Eq. 29}$$

$$m_{Mg} = \frac{M_{MgH_2}}{M_{Mg}} m_{MgH_2} \quad \text{Eq. 30}$$

$$C_{P_0} = \frac{m_{Mg} C_{P_{Mg}} + m_{Graphite} C_{P_{Graphite}}}{m_{Mg} + m_{Graphite}} \quad \text{Eq. 31}$$

Therefore, ΔT could be calculated based on different amounts of graphite. Detailed values are listed below; see Table 21.

Table 21 Variables and values used in the calculations.

Variables	Value	Unit
X_{H_2}	1.91	%
ΔH	74.5	kJ/mol H_2
$M_{Mg\,H_2}$	26.320	g/mol
M_{Mg}	24.305	g/mol
M_{H_2}	2.0158	g/mol
$C_{P_{Mg}}$	1022.83	J/kg.K
$C_{P_{Graphite}}$	1157.27	J/kg.K

APPENDIX C

GRAIN SIZE CALCULATION

Grain size was calculated based on the Williamson-Hall equation, Eq. 8. See Table 22 for the detailed results of X-ray pattern fitting. The full width half maximum of the peak (FWHM) was extracted from the fitted X-ray pattern, which was obtained via MDI Jade 5.0.

Table 22. Grain size calculation chart.

Sample No.	Sample detail	2θ	FW(θ) $*10^2$	Sin(θ) $*10^2$	FW(θ)*Cos(θ) $*10^3$	Grain size (nm)	Strain $*10^3$
		2.002	6.70	1.75	1.17		
1	Pure MgH_2 0.5h	2.550	7.90	2.22	1.38	9.86	3.04
		3.804	8.00	3.32	1.39		
		2.000	6.70	1.74	1.17		
2	Pure MgH_2 2h	2.553	8.10	2.23	1.41	9.63	2.91
		3.807	8.00	3.32	1.39		
		2.003	6.60	1.75	1.15		
3	Pure MgH_2 4h	2.550	8.20	2.22	1.43	8.78	1.57
		3.805	7.50	3.32	1.31		
		1.998	8.20	1.74	1.43		
4	Pure MgH_2 6h	2.550	8.50	2.22	1.48	7.98	2.48
		3.795	9.10	3.31	1.59		
		1.999	6.40	1.74	1.12		
5	MgH_2-TiH_2 0.5h	2.551	6.70	2.22	1.17	9.67	1.28
		3.805	6.90	3.32	1.20		
		2.001	7.20	1.75	1.26		
6	MgH_2-TiH_2 2h	2.554	7.30	2.23	1.27	8.37	0.82
		3.808	7.50	3.32	1.31		
		2.001	7.50	1.75	1.31		
7	MgH_2-TiH_2 4h	2.555	7.80	2.23	1.36	8.16	1.28
		3.807	8.00	3.32	1.39		
		2.002	8.00	1.75	1.40		
8	MgH_2-TiH_2 6h	2.558	8.30	2.23	1.45	7.62	1.28
		3.808	8.50	3.32	1.48		
	MgH_2-TiH_2 6h	1.997	7.40	1.74	1.29		
9	(10 g milling	2.549	7.20	2.22	1.26	10.95	4.63
	load)	3.793	8.90	3.31	1.55		
	MgH_2-TiH_2 6h	2.003	6.80	1.75	1.19		
10	(15 g milling	2.546	5.60	2.22	0.98	12.51	3.83
	load)	3.802	7.80	3.32	1.36		
		2.003	7.10	1.75	1.24		
11	MgH_2-$TiMn_2$ 2h	2.555	8.20	2.23	1.43	9.14	2.48
		3.810	8.30	3.32	1.45		
		2.006	8.10	1.75	1.41		
12	MgH_2-$TiMn_2$ 4h	2.556	8.60	2.23	1.50	8.37	2.48
		3.812	9.30	3.32	1.62		
		2.004	8.40	1.75	1.47		
13	MgH_2-$TiMn_2$ 6h	2.559	8.70	2.23	1.52	7.91	2.48
		3.814	9.40	3.33	1.64		

Table 22. Continued.

Sample No.	Sample detail	2θ	FW(θ) *10^2	Sin(θ) *10^2	FW(θ)*Cos(θ) *10^3	Grain size (nm)	Strain *10^3
		2.004	7.40	1.75	1.29		
14	MgH_2-VTiCr 2h	2.557	8.00	2.23	1.40	8.37	2.48
		3.810	8.10	3.32	1.41		
		2.001	8.60	1.75	1.50		
15	MgH_2-VTiCr 4h	2.551	8.30	2.22	1.45	8.01	2.88
		3.804	9.50	3.32	1.66		
		2.006	8.10	1.75	1.41		
16	MgH_2-VTiCr 6h	2.556	8.10	2.23	1.41	8.04	2.48
		3.813	8.80	3.33	1.53		

APPENDIX D

HYDROGENATION KINETIC MODELING

Johnson-Mehl-Avrami (JMA) has been found to be the best model to describe the hydrogenation kinetics of all the samples. In this section, the data fits by the JMA model for each sample are presented; see Figure 34-36. In addition, sample #3, pure MgH_2 milled for 4 h, was taken as an example to showcase the hydrogenation kinetic data modeling with various models mentioned in Table 5; see Figure 37.

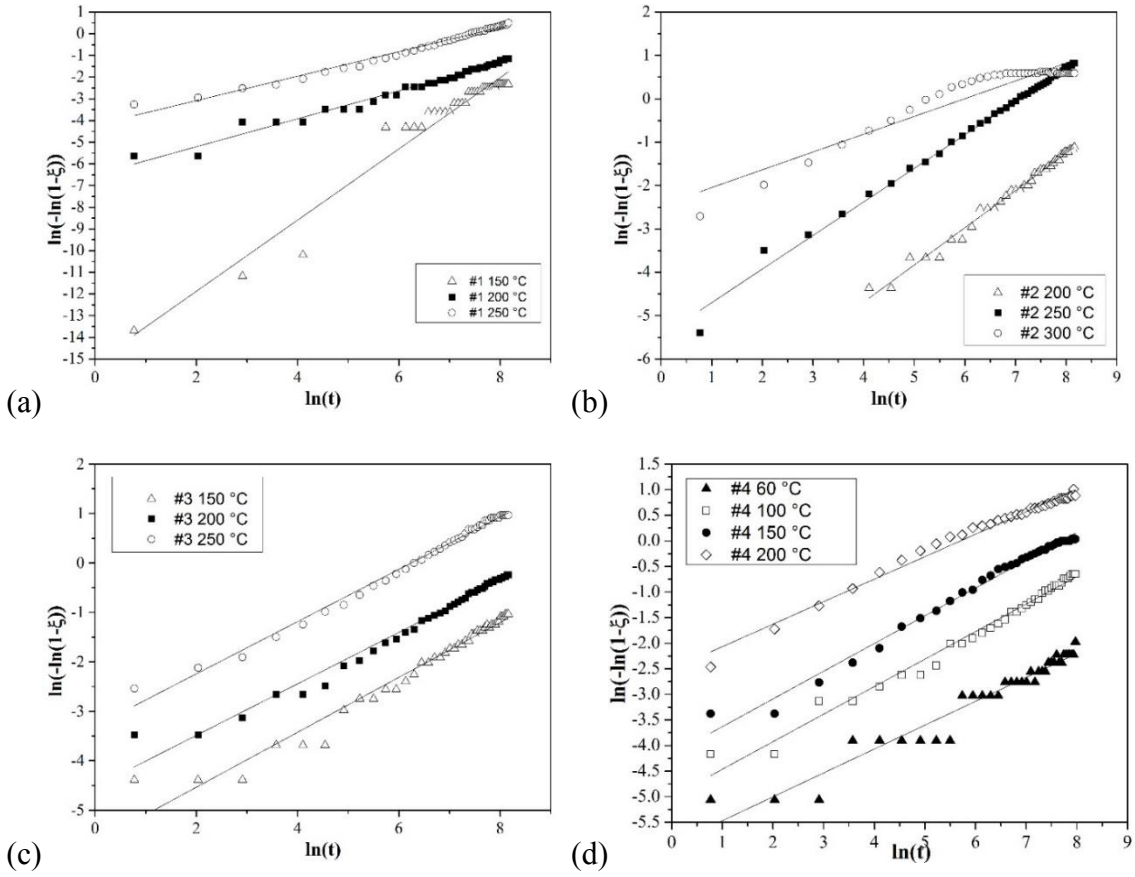

Figure 34. JMA model fitting of pure MgH_2 milled for a) 0.5 h, sample #1; b) 2 h, sample #2; c) 4 h, sample #3; and d) 6 h, sample #4.

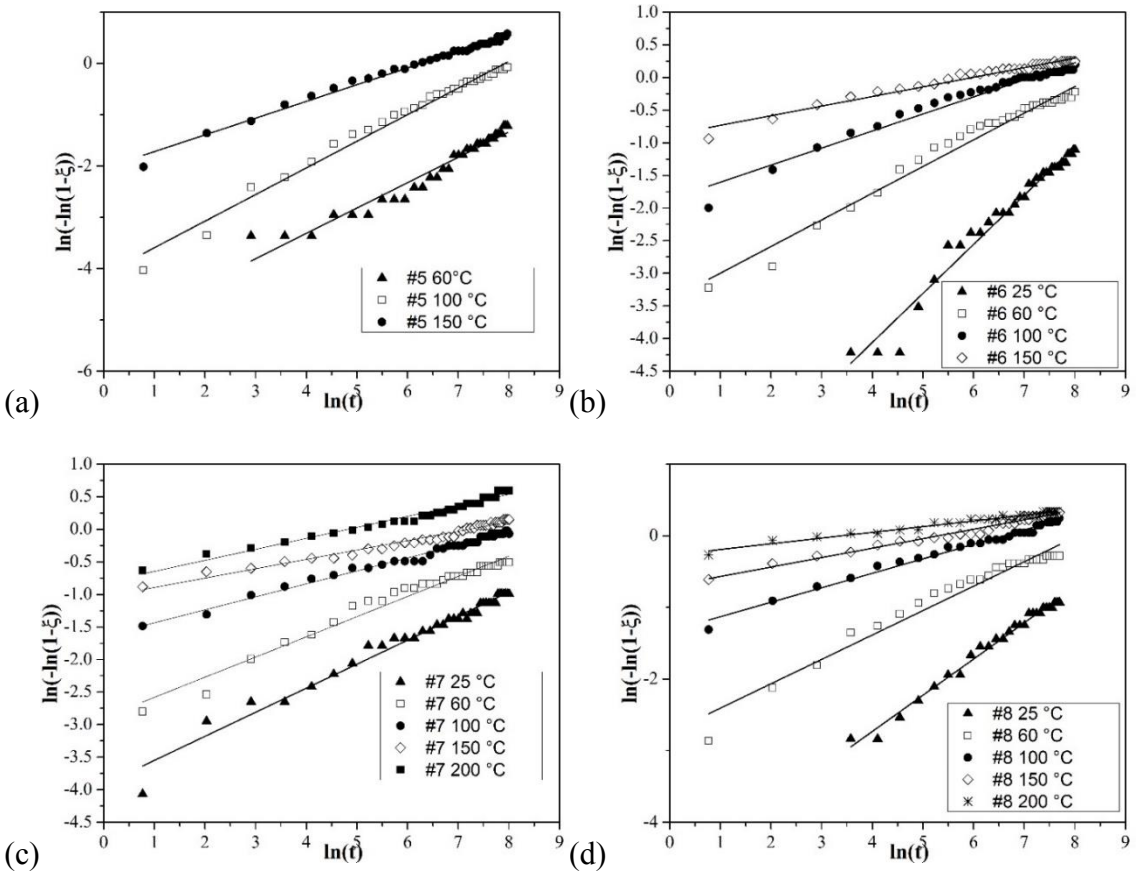

Figure 35. JMA model fitting of MgH_2-TiH_2 milled for a) 0.5 h, sample #5; b) 2 h, sample #6; c) 4 h, sample #7; and d) 6 h, sample #8.

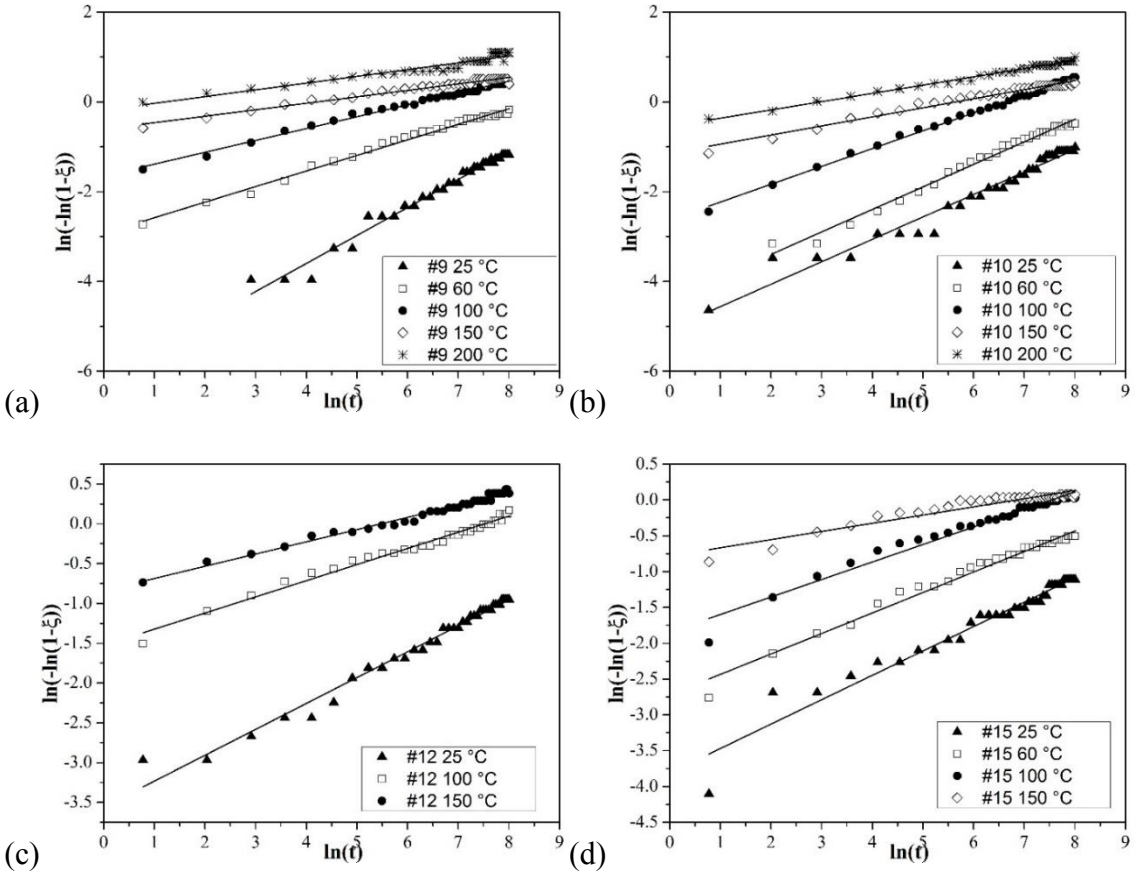

Figure 36. JMA model fitting of MgH_2-TiH_2 milled with a) 10 g milling load, sample #9 and b) 15 g milling load, sample #10, as well as c) MgH_2-$TiMn_2$ milled for 4 h, sample #12 and d) MgH_2-VTiCr milled for 4 h, sample #15.

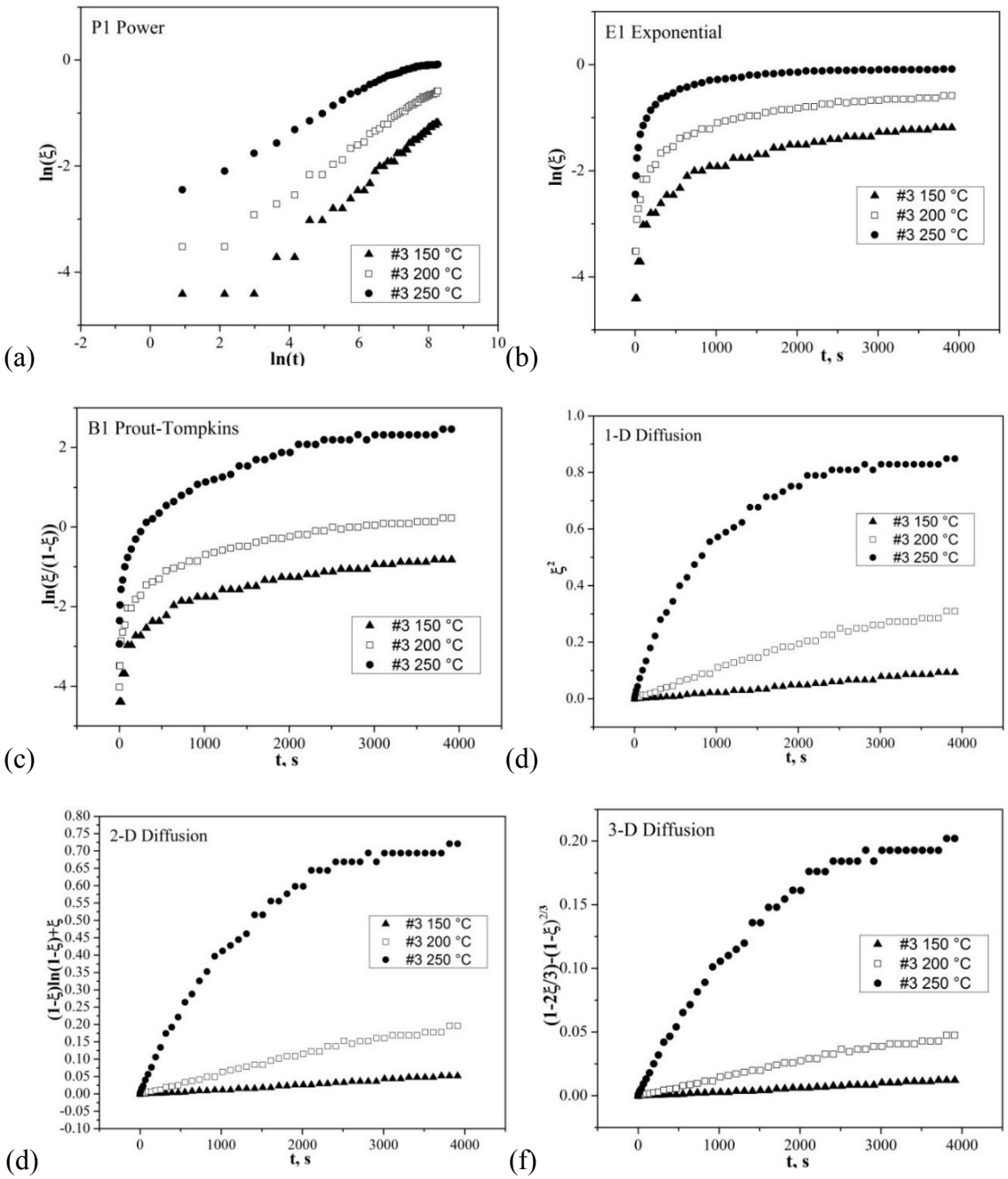

Figure 37. The kinetic modeling of pure MgH_2 milled for 4 h (sample #3) by a) P1 power; b) E1 Exponential; c) B1 Prout-Tompkins; d) 1-D Diffusion; e) 2-D Diffusion; f) 3-D Diffusion; g) 2-D Contracting; h) 3-D Contracting; i) F1 First Order; j) F2 Second Order; and k) F3 Third Order.

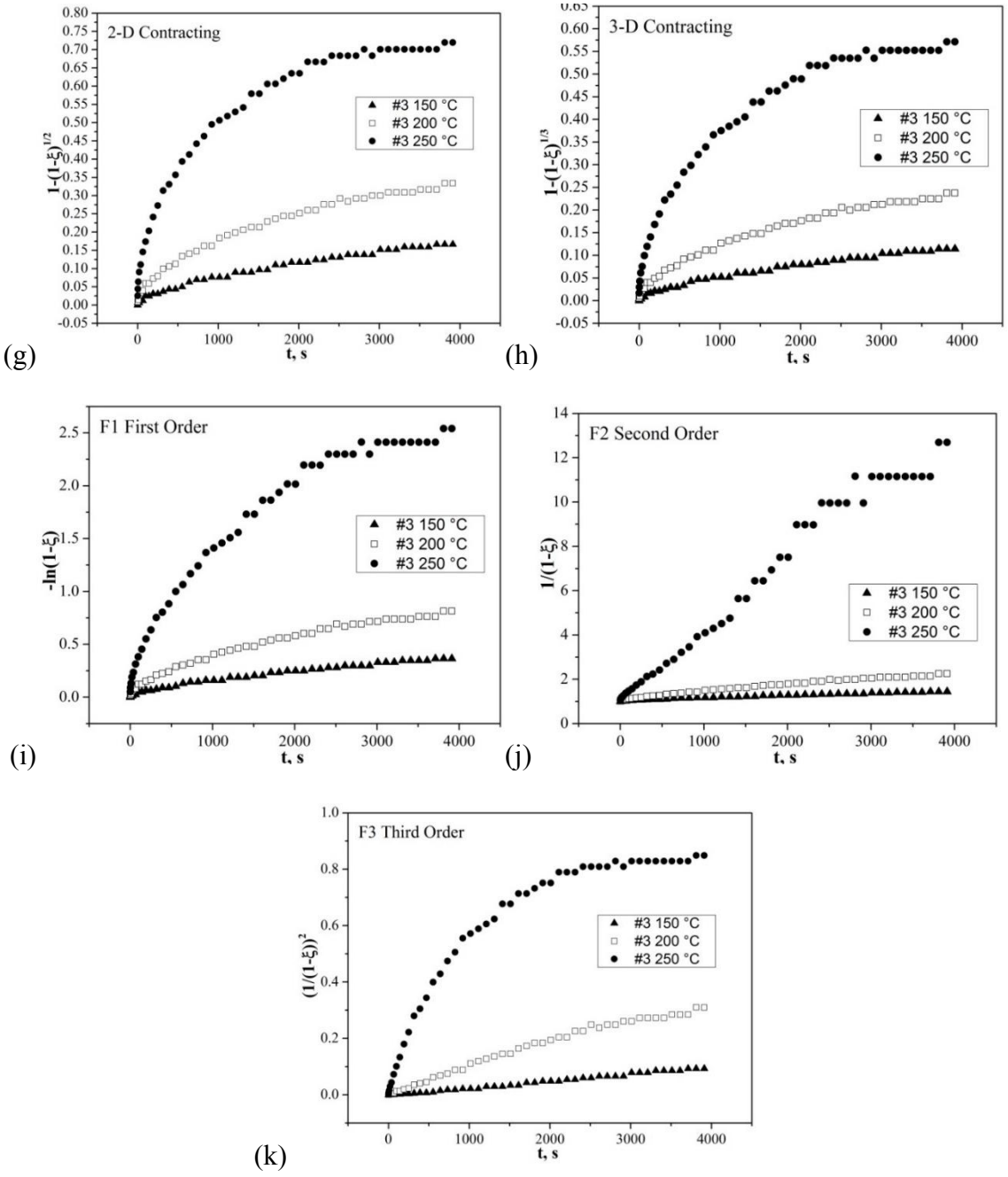

Figure 37. Continued.

REFERENCES

[1] Provincial Groninger Courant 1834.

[2] Tie SF, Tan CW. A Review of Energy Sources and Energy Management System in Electric Vehicles. Renewable and Sustainable Energy Reviews. 2013;20:82-102.

[3] Pollet BG, Staffell I, Shang JL. Current Status of Hybrid, Battery and Fuel Cell Electric Vehicles: From Electrochemistry to Market Prospects. Electrochim Acta. 2012;84:235-49.

[4] Khayyam H. Adaptive Intelligent Control of Vehicle Air Conditioning System. Appl Therm Eng. 2013;51:1154-61.

[5] Lambert MA, Jones BJ. Automotive Adsorption Air Conditioner Powered by Exhaust Heat. Part 1: Conceptual and Embodiment Design. Proceedings of the Institution of Mechanical Engineers, Part D: Journal of Automobile Engineering. 2006;220:959-72.

[6] AlQdah KS. Performance and Evaluation of Aqua Ammonia Auto Air Conditioner System Using Exhaust Waste Energy. Energy Procedia. 2011;6:467-76.

[7] Fang Z, A New Generation High Density Thermal Battery Based on Advanced Metal Hydrides. 0471-1522,

[8] Chan CC. The State of the Art of Electric, Hybrid, and Fuel Cell Vehicles. Proceedings of the IEEE. 2007;95:704-18.

[9] Kumar L, Jain S. Electric Propulsion System for Electric Vehicular Technology: A Review. Renewable and Sustainable Energy Reviews. 2014;29:924-40.

[10] Buschow KHJ. Electronic and Magnetic Properties of Metals and Ceramics, Part II. In: Buschow KHJ, editor. Materials Science and Technology-A Comprehensive Treatment. Weinheim VCH; 1994.

[11] Seayad AM, Antonelli DM. Recent Advances in Hydrogen Storage in Metal-Containing Inorganic Nanostructures and Related Materials. Adv Mater. 2004;16:765-77.

[12] Sandrock G. A Panoramic Overview of Hydrogen Storage Alloys from a Gas Reaction Point of View. J Alloys Compd. 1999;293-295:877-88.

[13] Bowman RC, Fultz B. Metallic Hydrides I: Hydrogen Storage and Other Gas-Phase Applications. MRS Bull. 2011;27:688-93.

[14] Varin RA, Czujko T, Wronski ZS. Nanomaterials for Solid State Hydrogen Storage. 2009.

[15] Bogdanović B, Ritter A, Spliethoff B. Active MgH_2-Mg Systems for Reversible Chemical Energy Storage. Angewandte Chemie International Edition in English. 1990;29:223-34.

[16] CHAPTER 9 - Solar Energy Storage by Metal Hydride. In: Ohta T, editor. Solar-Hydrogen Energy Systems: Pergamon; 1979. p. 193-224.

[17] Jain I, Vijay Y, Malhotra L, Uppadhyay K. Hydrogen Storage in Thin Film Metal Hydride—A Review. Int J Hydrogen Energy. 1988;13:15-23.

[18] Dantzer P. Metal-Hydride Technology: A Critical Review. In: Wipf H, editor. Hydrogen in Metals III: Springer Berlin Heidelberg; 1997. p. 279-340.

[19] Schlapbach L. Hydrogen as a Fuel and Its Storage for Mobility and Transport. MRS Bull. 2011;27:675-9.

[20] Huot J. Nanocrystalline Materials for Hydrogen Sotrage. In: Nalwa HS, editor. Nanoclusters and Nanocrystals: American Scientific Publishers; 2003. p. 53-85.

[21] Sakai T, Hazama T, Miyamura H, Kuriyama N, Kato A, Ishikawa H. Rare-earth-based Alloy Electrodes for a Nickel-metal Hydride Battery. J Less Common Met. 1991;172–174, Part 3:1175-84.

[22] Eichenauer W. F. A. Lewis: The Palladium Hydrogen System. Academic Press, London and New York 1967. 178 Seiten, 87 Abbildungen. Preis: 45 s. Berichte der Bunsengesellschaft für physikalische Chemie. 1967;71:1160-1.

[23] Joubert JM, Latroche M, Percheron-Guégan A. Metallic Hydrides II: Materials for Electrochemical Storage. MRS Bull. 2011;27:694-8.

[24] Chen XY, Wei LX, Deng L, Yang FS, Zhang ZX. A Review on the Metal Hydride Based Hydrogen Purification and Separation Technology. Applied Mechanics and Materials. 2013;448-453:3027-36.

[25] Zhou C, Fang ZZ, Ren C, Li J, Lu J. Effect of Ti Intermetallic Catalysts on Hydrogen Storage Properties of Magnesium Hydride. J Phys Chem C. 2013;117:12973-80.

[26] Lu J, Choi YJ, Fang ZZ, Sohn HY, Ronnebro E. Hydrogenation of Nanocrystalline Mg at Room Temperature in the Presence of TiH_2. J Am Chem Soc. 2010;132:6616-7.

[27] Tan X, Wang L, Holt CM, Zahiri B, Eikerling MH, Mitlin D. Body Centered Cubic Magnesium Niobium Hydride with Facile Room Temperature Absorption and Four Weight Percent Reversible Capacity. Phys Chem Chem Phys. 2012;14:10904-9.

[28] Moretto P, Zlotea C, Dolci F, Amieiro A, Bobet JL, Borgschulte A, et al. A Round

Robin Test Exercise on Hydrogen Absorption/Desorption Properties of a Magnesium Hydride Based Material. Int J Hydrogen Energy. 2013;38:6704-17.

[29] Solid-state Hydrogen Storage Materials and Chemistry: Woodhead Publishing and Maney Publishing; 2008.

[30] Bastide J-P, Bonnetot B, Létoffé J-M, Claudy P. Polymorphisme De L'hydrure De Magnesium Sous Haute Pression. Mater Res Bull. 1980;15:1779-87.

[31] Noritake T, Towata S, Aoki M, Seno Y, Hirose Y, Nishibori E, et al. Charge Density Measurement in MgH_2 by Synchrotron X-ray Diffraction. J Alloys Compd. 2003;356-357:84-6.

[32] Noritake T, Aoki M, Towata S, Seno Y, Hirose Y, Nishibori E, et al. Chemical Bonding of Hydrogen in MgH_2. Appl Phys Lett. 2002;81:2008-10.

[33] Stampfer; JF, Holley; CE, Suttle; JF. The Magnesium-Hydrogen System. J Amer Chem Soc. 1960;82:3504-8.

[34] Lu J, Choi YJ, Fang ZZ, Sohn HY, Ronnebro E. Hydrogen Storage Properties of Nanosized MgH_2-0.1TiH_2 Prepared by Ultrahigh-energy-high-pressure Milling. J Am Chem Soc. 2009;131:15843-52.

[35] Bogdanović B, Bohmhammel K, Christ B, Reiser A, Schlichte K, Vehlen R, et al. Thermodynamic Investigation of the Magnesium–hydrogen System. J Alloys Compd. 1999;282:84-92.

[36] Vigeholm B, Kjøller J, Larsen B, Pedersen AS. Formation and Decomposition of Magnesium Hydride. J Less Common Met. 1983;89:135-44.

[37] Kennelley JA, Varwig JW, Myers HW. Magnesium—Hydrogen Relationships. The Journal of Physical Chemistry. 1960;64:703-4.

[38] Aguey-Zinsou K-F, Ares-Fernández J-R. Hydrogen in Magnesium: Nnew Perspectives toward Functional Stores. Energy & Environmental Science. 2010;3:526.

[39] Er Sl, de Wijs GA, Brocks G. Tuning the Hydrogen Storage in Magnesium Alloys. The Journal of Physical Chemistry Letters. 2010;1:1982-6.

[40] Zhou C, Fang ZZ, Lu J, Zhang X. Thermodynamic and Kinetic Destabilization of Magnesium Hydride Using Mg-In Solid Solution Alloys. J Am Chem Soc. 2013.

[41] Orimo S, Fujii H. Materials Science of Mg-Ni-based New Hydrides. Applied Physics A Materials Science & Processing. 2001;72:167-86.

[42] Reiser A. The Application of Mg-based Metal-hydrides as Heat Energy Storage Systems. Int J Hydrogen Energy. 2000;25:425-30.

[43] Selvam P, Viswanathan B, Swamy CS, Srinivasan V. Magnesium and Magnesium Alloy Hydrides. Int J Hydrogen Energy. 1986;11:169-92.

[44] Vegge T, Hedegaard-Jensen LS, Bonde J, Munter TR, Nørskov JK. Trends in Hydride Formation Energies for Magnesium-3d Transition Metal Alloys. J Alloys Compd. 2005;386:1-7.

[45] Bogdanović B, Spliethoff B, Ritter A. The Magnesium Hydride System for Heat Storage and Cooling. Z Phys Chem. 1989;164:1497-508.

[46] Gasan H, Celik ON, Aydinbeyli N, Yaman YM. Effect of V, Nb, Ti and Graphite Additions on the Hydrogen Desorption Temperature of Magnesium Hydride. Int J Hydrogen Energy. 2012;37:1912-8.

[47] Bassetti A, Bonetti E, Pasquini L, Montone A, Grbovic J, Vittori Antisari M. Hydrogen Desorption from Ball milled MgH_2 Catalyzed with Fe. The European Physical Journal B. 2005;43:19-27.

[48] Huot J, Liang G, Boily S, Van Neste A, Schulz R. Structural Study and Hydrogen Sorption Kinetics of Ball-milled Magnesium Hydride. J Alloys Compd. 1999;293-295:495-500.

[49] Bao S, Tajima K, Yamada Y, Okada M, Yoshimura K. Color-neutral Switchable Mirrors Based on Magnesium-titanium Thin Films. Appl Phys A. 2007;87:621-4.

[50] Kalisvaart WP, Luber EJ, Poirier E, Harrower CT, Teichert A, Wallacher D, et al. Probing the Room Temperature Deuterium Absorption Kinetics in Nanoscale Magnesium Based Hydrogen Storage Multilayers Using Neutron Reflectometry, X-ray Diffraction, and Atomic Force Microscopy. The Journal of Physical Chemistry C. 2012;116:5868-80.

[51] Domènech-Ferrer R, Gurusamy Sridharan M, Garcia G, Pi F, Rodríguez-Viejo J. Hydrogenation Properties of Pure Magnesium and Magnesium–aluminium Thin Films. J Power Sources. 2007;169:117-22.

[52] Kim J-H, Kim B-G, Kang Y-M. Synthesis and Enhanced Hydrogen Desorption Kinetics of Magnesium Hydride using Hydriding Chemical Vapor Synthesis. J Alloys Compd. 2012;529:102-7.

[53] Bellemare J, Huot J. Hydrogen Storage Properties of Cold Rolled Magnesium Hydrides with Oxides Catalysts. J Alloys Compd. 2012;512:33-8.

[54] Vincent SD, Lang J, Huot J. Addition of Catalysts to Magnesium Hydride by Means of Cold Rolling. J Alloys Compd. 2012;512:290-5.

[55] Li L, Saita I, Saito K, Akiyama T. Effect of Synthesis Temperature on the Hydriding Behaviors of Mg–Ni–Cu Ternary Hydrogen Storage Alloys synthesized by hydriding combustion synthesis. J Alloys Compd. 2004;372:218-23.

[56] Li L, Akiyama T, Yagi J-i. Hydrogen Storage Alloy of Mg_2NiH_4 Hydride Produced by Hydriding Combustion Synthesis from Powder of Mixture Metal. J Alloys Compd. 2000;308:98-103.

[57] Bazzanella N, Checchetto R, Miotello A. Atoms and Nanoparticles of Transition Metals as Catalysts for Hydrogen Desorption from Magnesium Hydride. Journal of Nanomaterials. 2011;2011:1-11.

[58] Anik M, Karanfil F, Küçükdeveci N. Development of the High Performance Magnesium Based Hydrogen Storage Alloy. Int J Hydrogen Energy. 2012;37:299-308.

[59] Shelyapina MG, Fruchart D, Wolfers P. Electronic Structure and Stability of New FCC Magnesium Hydrides Mg_7MH_{16} and Mg_6MH_{16} (M = Ti, V, Nb): An AB Initio Study. Int J Hydrogen Energy. 2010;35:2025-32.

[60] Tan X, Zahiri B, Holt CMB, Kubis A, Mitlin D. A TEM Based Study of the Microstructure During Room Temperature and Low Temperature Hydrogen Storage Cycling in MgH_2 Promoted by Nb–V. Acta Mater. 2012;60:5646-61.

[61] Zahiri B, Danaie M, Tan X, Amirkhiz BS, Botton GA, Mitlin D. Stable Hydrogen Storage Cycling in Magnesium Hydride, in the Range of Room Temperature to 300 °C, Achieved Using a New Bimetallic Cr-V Nanoscale Catalyst. J Phys Chem C. 2012;116:3188-99.

[62] Di Vece M, Grandjean D, Van Bael M, Romero C, Wang X, Decoster S, et al. Hydrogen-Induced Ostwald Ripening at Room Temperature in a Pd Nanocluster Film. Phys Rev Lett. 2008;100.

[63] Dobrovolsky VD, Ershova OG, Solonin YM, Khyzhun OY, Paul-Boncour V. Influence of TiB_2 Addition upon Thermal Stability and Decomposition Temperature of the MgH_2 Hydride of a Mg-based Mechanical Alloy. J Alloys Compd. 2008;465:177-82.

[64] Ma L-P, Wang P, Cheng H-M. Hydrogen Sorption Kinetics of MgH_2 Catalyzed with Titanium Compounds. Int J Hydrogen Energy. 2010;35:3046-50.

[65] Xie L, Liu Y, Wang YT, Zheng J, Li XG. Superior Hydrogen Storage Kinetics of MgH_2 Nanoparticles Doped with TiF_3. Acta Mater. 2007;55:4585-91.

[66] Dehouche Z, Djaozandry R, Huot J, Boily S, Goyette J, Bose TK, et al. Influence of Cycling on the Thermodynamic and Structure Properties of Nanocrystalline Magnesium Based Hydride. J Alloys Compd. 2000;305:264-71.

[67] Liang G, Huot J, Boily S, Schulz R. Hydrogen Desorption Kinetics of a Mechanically Milled MgH_2+5at.%V Nanocomposite. J Alloys Compd. 2000;305:239-45.

[68] Pelletier J, Huot J, Sutton M, Schulz R, Sandy A, Lurio L, et al. Hydrogen Desorption Mechanism in MgH_2-Nb Nanocomposites. Physical Review B. 2001;63.

[69] Malka IE, Bystrzycki J, Płociński T, Czujko T. Microstructure and Hydrogen Storage Capacity of Magnesium Hydride with Zirconium and Niobium Fluoride Additives after Cyclic Loading. J Alloys Compd. 2011;509:S616-S20.

[70] Jin S, Shim J, Ahn J, Cho Y, Yi K. Improvement in Hydrogen Sorption Kinetics of MgH_2 with Nb Hydride Catalyst. Acta Mater. 2007;55:5073-9.

[71] Liang G, Huot J, Boily S, Van Neste A, Schulz R. Catalytic Effect of Transition Metals on Hydrogen Sorption in Nanocrystalline Ball Milled MgH_2–Tm (Tm=Ti, V, Mn, Fe and Ni) Systems. J Alloys Compd. 1999;292:247-52.

[72] Pighin SA, Capurso G, Lo Russo S, Peretti HA. Hydrogen Sorption Kinetics of Magnesium Hydride Enhanced by the Addition of Zr_8Ni_{21} Alloy. J Alloys Compd. 2012;530:111-5.

[73] Polanski M, Bystrzycki J, Plocinski T. The Effect of Milling Conditions on Microstructure and Hydrogen Absorption/Desorption Properties of Magnesium Hydride (MgH_2) without and with Cr_2O_3 Nanoparticles. Int J Hydrogen Energy. 2008;33:1859-67.

[74] Sabitu ST, Fagbami O, Goudy AJ. Kinetics and Modeling Study of Magnesium Hydride with Various Additives at Constant Pressure Thermodynamic Driving Forces. J Alloys Compd. 2011;509:S588-S91.

[75] Shang C. Mechanical Alloying and Electronic Simulations of (MgH_2+M) Systems (M=Al, Ti, Fe, Ni, Cu and Nb) for Hydrogen Storage. Int J Hydrogen Energy. 2004;29:73-80.

[76] Sabitu ST, Gallo G, Goudy AJ. Effect of TiH_2 and Mg_2Ni Additives on the Hydrogen Storage Properties of Magnesium Hydride. J Alloys Compd. 2010;499:35-8.

[77] Yu XB, Guo YH, Yang H, Wu Z, Grant DM, Walker GS. Improved Hydrogen Storage in Magnesium Hydride Catalyzed by Nanosized $Ti_{0.4}Cr_{0.15}Mn_{0.15}V_{0.3}$ Alloy. The Journal of Physical Chemistry C. 2009;113:5324-8.

[78] Yonkeu AL, Swainson IP, Dufour J, Huot J. Kinetic Investigation of the Catalytic Effect of a Body Centered Cubic-Alloy $TiV_{1.1}Mn_{0.9}$ (BCC) on Hydriding/Hehydriding Properties of Magnesium. J Alloys Compd. 2008;460:559-64.

[79] Amirkhiz BS, Danaie M, Barnes M, Simard B, Mitlin D. Hydrogen Sorption Cycling Kinetic Stability and Microstructure of Single-Walled Carbon Nanotube (SWCNT) Magnesium Hydride (MgH_2) Nanocomposites. The Journal of Physical Chemistry C. 2010;114:3265-75.

[80] Konarova M, Tanksale A, Beltramini JN, Lu GQ. Porous MgH_2/C Composite with Fast Hydrogen Storage Kinetics. Int J Hydrogen Energy. 2012;37:8370-8.

[81] Durojaiye T, Goudy A. Desorption Kinetics of Lithium Amide/Magnesium Hydride Systems at Constant Pressure Thermodynamic Driving Forces. Int J Hydrogen Energy.

2012;37:3298-304.

[82] Saldan I, Campesi R, Zavorotynska O, Spoto G, Baricco M, Arendarska A, et al. Enhanced Hydrogen Uptake/Release in 2LiH–MgB_2 Composite with Titanium Additives. Int J Hydrogen Energy. 2012;37:1604-12.

[83] Mao J, Guo Z, Yu X, Ismail M, Liu H. Enhanced Hydrogen Storage Performance of $LiAlH_4$–MgH_2–TiF_3 Composite. Int J Hydrogen Energy. 2011;36:5369-74.

[84] Laidler KJ. Chemical Kinetics1965.

[85] House JE. Principles of Chemical Kinetics: Wm. C. Brown Publishers; 1997.

[86] Hood JJ. XXXVI.On The Influence of Heat on The Rate of Chemical Change. Philosophical Magazine Series 5. 1885;20:323-8.

[87] Hood JJ. XLIX.On The Laws of Chemical Change.—Part I. Philosophical Magazine Series 5. 1878;6:371-83.

[88] van't Hoff MJH. Etudes De Dynamique Chimique. Recl Trav Chim Pays-Bas. 1884;3:333-6.

[89] Arrhenius S. Ober Die Reacktionsgeschwindigkeit Bei Der Inversion Von Rohrzucker Durch Sauren. Z Physik Chem. 1889;4:226-48.

[90] Kissinger HE. Reaction Kinetics in Differential Thermal Analysis. Anal Chem. 1957;29:1702-6.

[91] Martin M, Gommel C, Borkhart C, Fromm E. Absorption and Desorption Kinetics of Hydrogen Storage Alloys. J Alloys Compd. 1996;238:193-201.

[92] Muthukumar P, Satheesh A, Linder M, Mertz R, Groll M. Studies on Hydriding Kinetics of Some La-based Metal Hydride Alloys. Int J Hydrogen Energy. 2009;34:7253-62.

[93] Chou K-C, Xu K. A New Model for Hydriding and Dehydriding Reactions in Intermetallics. Intermetallics. 2007;15:767-77.

[94] Rudman PS. Hydrogen Diffusion Rate Limited Hydriding and Dehydriding Kinetics. J Appl Phys. 1979;50:7195.

[95] Peterson DT, Westlake D. The Rate of Reaction of Hydrogen with Thorium. Journal of Physical Chemistry. 1959;63:1514-6.

[96] Ron M. The Normalized Pressure Dependence Method for the Evaluation of Kinetic Rates of Metal Hydride Formation/Decomposition. J Alloys Compd. 1999;283:178-91.

[97] Broom D. The Accuracy of Hydrogen Sorption Measurements on Potential Storage Materials. Int J Hydrogen Energy. 2007;32:4871-88.

[98] Han J, Lee J. A Study of the Hydriding Kinetics of Mg_2Ni at the Near Isothermal Condition. Int J Hydrogen Energy. 1987;12:417-24.

[99] Akiyama T, Tazaki TA, Takahashi R, Yagi J. Kinetics of Hydrogen Absorption and Desorption of Magnesium Nickel Alloy. Intermetallics. 1996;4:659-62.

[100] Wang XL, Suda S. Reaction Kinetics of Metal Hydrides under Quasi-isothermal Conditions. J Less Common Met. 1991;172-174:969-82.

[101] Ellinger FH, Holley CE, McInteer BB, Pavone D, Potter RM, Staritzky E, et al. The Preparation and Some Properties of Magnesium Hydride. J Am Chem Soc. 1955;77:2647-8.

[102] Stander CM. Kinetics of Formation of Magnesium Hydride from Magnesium and Hydrogen. Electron Microscopy Society of Southern Africa 15th Annual Conference. 1976.

[103] Barkhordarian G, Klassen T, Bormann R. Kinetic Investigation of the Effect of Milling Time on the Hydrogen Sorption Reaction of Magnesium Catalyzed with Different Nb_2O_5 Contents. J Alloys Compd. 2006;407:249-55.

[104] Yao X, Zhu ZH, Cheng HM, Lu GQ. Hydrogen Diffusion and Effect of Grain Size on Hydrogenation Kinetics in Magnesium Hydrides. J Mater Res. 2008;23:336-40.

[105] Pan YB, Wu YF, Li Q. Modeling and Analyzing the Hydriding Kinetics of Mg–$LaNi_5$ Composites by Chou Model. Int J Hydrogen Energy. 2011;36:12892-901.

[106] Haberman Z, Bloch J, Mintz MH, Jacob I. Kinetics of Hydride Formation in Massive $LaAl_{0.25}Ni_{4.75}$ Samples. J Alloys Compd. 1997;253-254:556-9.

[107] Oh JW, Kim CY, Nahm KS, Sim KS. The Hydriding Kinetics of $LaNi_{4.5}Al_{0.5}$ with Hydrogen. J Alloys Compd. 1998;278:270-6.

[108] Mote VD, Purushotham Y, Dole BN. Williamson-Hall Analysis in Estimation of Lattice Strain in Nanometer-sized ZnO Particles. Journal of Theoretical and Applied Physics. 2012;6:6.

[109] Surface Area And Pore Structure by Gas Adsorption.

[110] Jain IP, Lal C, Jain A. Hydrogen Storage in Mg: A Most Promising Material. Int J Hydrogen Energy. 2010;35:5133-44.

[111] Leardini F, Ares JR, Fernández JF, Bodega J, Sánchez C. An Investigation on the Thermodynamics and Kinetics of Magnesium Hydride Decomposition Based on Isotope Effects. Int J Hydrogen Energy. 2011;36:8351-7.

[112] Wang XL, Suda S. Consistent Determination of the Intrinsic Kinetic Properties between Hydrogen and Hydriding Alloys. J Alloys Compd. 1995;231:660-5.

[113] Song MY, Ivanov E, Darriet B, Pezat M, Hagenmuller P. Hydriding and Dehydriding Characteristics of Mechanically Alloyed Mixtures Mg-xwt.%Ni (x = 5, 10, 25 and 55). J Less Common Met. 1987;131:71-9.

[114] Kessler; HD, Rostoker; W, Thyne RJV, Titanium Phase Diagrams. Wright Air Development Center, 1953.

[115] Gulbransen EA, Andrew KF, Brassart FA. The Reaction of Hydrogen with Graphite at 1200° to 1650°C. J Electrochem Soc. 1965;112:49-52.

[116] Luo Q, An XH, Pan YB, Zhang X, Zhang JY, Li Q. The Hydriding Kinetics of Mg–Ni Based Hydrogen Storage Alloys: A Comparative Study on Chou Model and Jander Model. Int J Hydrogen Energy. 2010;35:7842-9.

[117] Montone A, Aurora A, Mirabile Gattia D, Vittori Antisari M. Effect of Hydrogen Pressure and Temperature on the Reaction Kinetics between Fe-doped Mg and Gydrogen Gas. J Alloys Compd. 2011;509:S580-S3.

[118] Avrami M. Kinetics of Phase Change. I General Theory. J Chem Phys. 1939;7:1103-12.

[119] Sharp JH, Brindley GW, Achar BNN. Numerical Data for Some Commonly Used Solid State Reaction Equations. J Am Ceram Soc. 1966;49:379-82.

[120] Li J, Fan P, Fang ZZ, Zhou C. Kinetics of Isothermal Hydrogenation of Magnesium with TiH_2 Additive. Int J Hydrogen Energy. 2014;39:7373-81.

[121] Corey RL, Ivancic TM, Shane DT, Carl EA, Bowman RC, Bellosta von Colbe JM, et al. Hydrogen Motion in Magnesium Hydride by NMR. The Journal of Physical Chemistry C. 2008;112:19784-90.

[122] Peng S-k, Xiao X-z, Xu R-j, Li L, Wu F, Li S-q, et al. Hydrogen Storage Behaviors and Microstructure of MF_3 (M=Ti, Fe)-doped Magnesium Hydride. Transactions of Nonferrous Metals Society of China. 2010;20:1879-84.

[123] Gur I, Sawyer K, Prasher R. Searching for a better thermal battery. Science. 2012;335:1454-5.

[124] Yang J, Sudik A, Wolverton C, Siegel DJ. High capacity hydrogen storage materials: attributes for automotive applications and techniques for materials discovery. Chem Soc Rev. 2010;39:656-75.

[125] Herrmann U, Geyer M, Kearney D, Overview on Thermal Storage Systems. Golden, FLABEG Solar International GmbH, 2003.

[126] Zalba B, Marín JM, Cabeza LF, Mehling H. Review on thermal energy storage with phase change: materials, heat transfer analysis and applications. Appl Therm Eng. 2003;23:251-83.